AFCRL-65-138

AD614235

SATURATION PHENOMENA IN Zn_2Y FERRITE AT FREQUENCIES BELOW RESONANCE

By

R. E. Tokheim

M. L. Report No. 1290

February 1965

Microwave Laboratory

W. W. HANSEN LABORATORIES OF PHYSICS

STANFORD UNIVERSITY . STANFORD, CALIFORNIA

182 p

COPY 2 OF 3 vc

HARD COPY $. 5.00

MICROFICHE $. 1.25

Scientific Report No. 4
for
Contract AF 19(628)-342
Project No. 4600
Task 460003

DDC
RECEIVED
APR 29 1965
DDC-IRA E

Prepared for
Air Force Cambridge Research Laboratories
Office of Aerospace Research
United States Air Force
Bedford, Massachusetts

ARCHIVE COPY

AFCRL-65-138

Microwave Laboratory
W. W. Hansen Laboratories of Physics
Stanford University
Stanford, California

SATURATION PHENOMENA IN Zn_2Y FERRITE AT FREQUENCIES BELOW RESONANCE

By

R. E. Tokheim

M. L. Report No. 1290
February 1965

Scientific Report No. 4
for
Contract AF 19(628)-342
Project No. 4600
Task 460003

Prepared
for
Air Force Cambridge Research Laboratories
Office of Aerospace Research
United States Air Force
Bedford, Massachusetts

NOTICES

Requests for additional copies by agencies of the Department of Defense, their contractors, or other government agencies should be directed to:

DEFENSE DOCUMENTATION CENTER (DDC)
CAMERON STATION
ALEXANDRIA, VIRGINIA 22314

Department of Defense contractors must be established for DDC services or have their "need-to-know" certified by the cognizant military agency of their project or contract.

All other persons and organizations should apply to the:

Clearinghouse for Federal Scientific
and Technical Information (CFSTI)
Sills Building
5285 Port Royal Road
Springfield, Virginia 22151

ABSTRACT

An experimental and theoretical investigation was made of transverse pumping saturation effects in Zn_2Y ferrite at frequencies far below ferromagnetic resonance. Chief interest was in saturation effects at frequencies below the bottom of the spin wave manifold, where the lowest order phonon instabilities were expected to compete favorably with the higher order spin wave instabilities.

Measurements of saturation effects in single crystal Zn_2Y, with the easy plane lying in the plane of the disk, were made at 1.32 kMc. The dc and rf magnetic fields were applied orthogonally in the plane of the disk. The large rf magnetic fields required were obtained by employing a strontium titanate dielectric resonator. In these experiments the order of the first resonant spin wave instability permitted was varied from the first to the fifth by adjusting the position of the spin wave manifold relative to the pump frequency. The nature of the saturation was investigated by observing the waveform of the reflected pump pulse.

Theoretical on-resonance spin wave thresholds up to fourth order and off-resonance spin wave thresholds up to second order were derived. The first order theoretical spin wave threshold was the lowest threshold in the range of low dc magnetic fields. At higher dc fields the second order theoretical on- and off-resonance spin wave thresholds dominated the higher order thresholds. Taking the magnetoelastic effect as the dominant mechanism, first order phonon thresholds were derived for transverse and longitudinal elastic waves propagating in the easy plane and along the c-axis. The lowest theoretical phonon threshold was for transverse elastic waves propagating and polarized in the easy plane, and at frequencies below the bottom of the spin wave manifold, this threshold dominated the theoretical second order off resonance spin wave threshold. Theory was developed for the growth of phonon instabilities from thermal level in order to relate pulse saturation effects to the phonon absorption.

Transverse pumping thresholds observed experimentally were comparable with the above theoretical predictions and strongly indicate that first order phonon instabilities dominate the higher order spin wave instabilities at frequencies below the bottom of the spin wave manifold. These results together with the phonon growth theory made it possible to obtain rough estimates for the phonon Q, one magnetoelastic constant, and the exchange field of Zn_2Y in the easy plane. The observed pulse saturation effects and the results of two experiments for two different phonon absorption levels indicated the presence of nonlinear elastic wave damping.

ERRATA SHEET

FOR

SATURATION PHENOMENA IN Zn$_2$Y FERRITE AT FREQUENCIES BELOW RESONANCE

by

R. E. Tokheim

M. L. Report No. 1290

Page	
iii.	Fourth line from bottom, insert hyphen between off and resonance.
40.	Second paragraph, second line, change "thresholds exist of x" to read "thresholds exist for x" .
45.	Equation (3.5), third term, change α_j to "α_ℓ" .
46.	Equation (3.7), first term, change $c_{ijl\ell}$ to "$c_{ijk\ell}$" .
46.	Equation (3.8), first term, change c_{ijklmn} to "$c_{ijk\ell mn}$" .
58.	Equation (3.26a), remove the parenthesis from the LHS .
70.	Second line below Eq. (3.55), change $C_{11} - C_{12}$ to "$c_{11} - c_{12}$" .
82.	First line below Eq. (4.14), insert "G" before the bracketed term.
119.	Equation (5.7), delete the minus sign on the LHS .
143.	The definition for H_D in the upper part of the figure should read "H_D = Demagnetizing field in the plane of the ferrite desk" .
160.	Left hand column, third and fourth items from the bottom, change ($1/{}^\circ C^{-1}$) to read "(${}^\circ C^{-1}$)" .

ACKNOWLEDGEMENT

I am deeply grateful to Dr. Bert A. Auld, my research advisor, for his guidance and encouragement. I truly appreciate the many helpful discussions with Dr. Donald K. Winslow regarding the experiments. Also, I have benefitted greatly by several discussions with Dr. H. John Shaw. My thanks to Dr. Robert L. White for his reading and comments.

All of the supporting personnel and facilities of the Microwave Laboratory were indispensable during the course of this work, and I sincerely appreciate their services. For the final preparation of this report I would like to thank the Reports and Drafting Office staffs for typing the manuscript and drawing the figures, and Al S. Braun for his coordinative efforts.

My wife Diane deserves special thanks for aiding with the typing and for her loving support and encouragement. Little Shirley came too soon to help.

TABLE OF CONTENTS

Appendices

LIST OF FIGURES

CHAPTER I

INTRODUCTION

The term saturation is used in two ways in discussing the properties of ferrites. The most common use applies to all varieties of ferromagnetic materials. It refers to the static state of the average magnetization vector when the atomic magnetic moments are aligned in one direction due to the application of a sufficiently large dc magnetic field. Thus a material is said to be saturated when its magnetization approaches a constant value with increasing dc magnetic field intensity.

The type of saturation of special concern here is the saturation of the uniform precessional motion of the magnetization. The simplest motion of the magnetization obtains when the magnetization itself is statically saturated by the application of a sufficiently large dc magnetic field. A uniform precessional motion of the magnetization may be established by the application of a transverse rf magnetic field. Saturation of the uniform precessional motion is usually defined in terms of a critical rf magnetic field corresponding to the point at which greatly increased losses obtain if the rf magnetic field is further increased. These losses are due to instabilities arising from nonlinearities in the equation of motion for the magnetization.

The saturation of the uniform motion of the magnetization at ferromagnetic resonance, observed by Damon,[1] and Bloembergen and Wang,[2] was first explained by H. Suhl.[3] He showed that such saturation could be explained on the basis of excitation of unstable spin waves at the pump frequency, and further showed that a subsidiary absorption having a lower saturation threshold would occur when half of the pump frequency was within the spin wave manifold. This is due to unstable spin waves at half the pump frequency.

This early work was concerned with spin wave instabilities excited by a pump frequency which coincided with ferromagnetic resonance and hence was above the bottom of the spin wave manifold. Recently, it has been shown theoretically that higher order spin wave instabilities may also cause saturation of the uniform motion when the pump frequency is below the bottom of the spin wave manifold--where the first and second order instabilities are far off resonance.[4,5] Even under these conditions there still exist resonant acoustic waves at the pump frequency and at one-half the pump frequency,[6] and there exist several mechanisms by which phonon instabilities at these frequencies may be excited.[7] It is unlikely that such phonon instabilities could compete favorably with spin wave instabilities when the pump frequency is within the spin wave manifold because weaker coupling mechanisms are involved. Operation with the pump below the manifold, however, allows only higher order spin wave instabilities to exist at resonance; and the lowest order phonon instabilities might be expected to compete favorably with higher-order spin wave instabilities, since the thresholds generally increase with the order of the instability.

The purpose of this study is to report a theoretical and experimental investigation of the transverse pumping saturation effects in Zn_2Y ferrite ($Zn_2 Ba_2 Fe_{12} O_{22}$) at dc magnetic fields corresponding to frequencies below the bottom of the spin wave manifold. The object was to investigate the instability mechanisms and to determine whether saturation is caused by spin waves or phonons. Experimentally, the pump frequency was fixed at 1.32 kMc, and the dc magnetic field was varied to adjust the position of the spin wave manifold with respect to the pump frequency.

The hexagonal material Zn_2Y was chosen because it has a magnetic "easy" plane. The large magnetic anisotropy of Zn_2Y makes it possible to operate below ferromagnetic resonance with relatively low applied dc magnetic fields. In the easy plane, then, the stiffness of the magnetization is low and it is possible to achieve large uniform precession angles with a much lower rf magnetic field than would otherwise be required.

The theory of instabilities pumped at frequencies below the spin wave manifold is developed in Chapters II and III. The derivation of thresholds for spin wave instabilities up to fourth order is presented in Chapter II. The optimum spin wave thresholds were obtained for each order. Chapter III contains a derivation of the first order thresholds for phonon instabilities. Various possible instability mechanisms are discussed. By taking the magnetoelastic effect as the dominant mechanism, thresholds were determined for transverse and longitudinal acoustic waves propagating in the easy plane and along the c-axis. A comparison was made between the lowest theoretical phonon thresholds and the spin wave thresholds of various orders for both the resonant and nonresonant cases.

Chapter IV is concerned with the growth of phonon instabilities from thermal level. The phonon power absorption was examined for both an ideal pulse and the actual power pulse used in the experiments. The threshold field, at which the effect of the instabilities can be observed by saturation of the reflected pump pulse, is expressed in terms of measurable microwave parameters.

The microwave apparatus and techniques which were employed in measuring the pumping thresholds are described in Chapter V. Large rf magnetic fields were obtained by using a strontium titanate dielectric resonator. The basic resonator theory as well as resonator and ferrite heating effects are analyzed. The methods used to measure the unloaded Q_0 are discussed.

Chapter VI is devoted to results of actual instability threshold measurements. Transverse thresholds were measured in a single crystal Zn_2Y disk with the easy plane lying in the plane of the disk. The dc and rf magnetic fields were applied in the plane of the disk. Results from two experiments are correlated with the phonon and spin wave threshold theory developed in Chapters II and III and with the phonon growth theory of Chapter IV. In correlating theory with experimental results, values were obtained for one magnetoelastic constant, the phonon Q , and the exchange field of Zn_2Y .

At the end of each chapter a summary is given which describes the important features and conclusions for that chapter.

CHAPTER II

SPIN WAVE INSTABILITY THRESHOLDS

This chapter is concerned with the calculation of transverse pump thresholds of spin wave instabilities up to fourth order for operation far below ferromagnetic resonance. The order of an instability n is defined as

$$n = \frac{2\omega}{\omega_p} \quad , \tag{2.1}$$

where ω is the frequency of the spin wave whose instability is being considered, and ω_p is the pump frequency of the rf magnetic field. In the experiment described in Chapter VI, the position of the bottom of the spin wave manifold (Fig. 2.2a) is varied with respect to the pump frequency by changing the strength of the applied dc magnetic field in the ferrite sample. From (2.1) and Fig. 2.2a instabilities of <u>resonant</u> spin waves are permitted only for orders n such that $n\omega_p/2$ lies above the bottom of the manifold. Thus the order of the first allowable spin wave instability varies with the dc magnetic field, and proper interpretation of the experiments requires the study of several orders of spin wave instabilities.

A. GENERAL EQUATION OF MOTION

The motion of the magnetization $\underset{\sim}{M}$ is ultimately based upon the motion of each atomic magnetic moment. The classical lossless equation of motion of the average atomic magnetic moment on a macroscopic scale is

$$\frac{\partial \underset{\sim}{M}(\underset{\sim}{r},t)}{\partial t} = -\gamma\, \underset{\sim}{M}(\underset{\sim}{r},t) \times \underset{\sim}{H}(\underset{\sim}{r},t) \quad , \tag{2.2}$$

where $\underset{\sim}{H}$, the total magnetic field at point $\underset{\sim}{r}$, results from internal fields due to the motion of $\underset{\sim}{M}$ as well as from externally applied magnetic fields. The gyromagnetic ratio γ is given by

$$\gamma = \frac{ge}{2mc} \quad . \tag{2.3}$$

With $g = 2.00$ for moments due only to the spin of the electron, the value for $\gamma/2\pi$ becomes 2.8 Mc/Oe. Losses will later be introduced into (2.2) through phenomenological damping.

The assumption is now made that the magnetization is saturated by the application of a sufficiently large dc magnetic field. It will further be assumed that the dc magnetic field, as well as the value of the saturated magnetization, is uniform throughout the sample volume. With these assumptions it is convenient to introduce the unit magnetization vector $\underset{\sim}{\alpha}(\underset{\sim}{r},t)$, whose components are the direction cosines of the magnetization, as follows:

$$\underset{\sim}{\alpha}(\underset{\sim}{r},t) = \frac{\underset{\sim}{M}(\underset{\sim}{r},t)}{M_s} \quad , \tag{2.4}$$

where M_s is the saturated magnetization. Equation (2.2) then becomes

$$\dot{\underset{\sim}{\alpha}}(\underset{\sim}{r},t) = -\gamma\, \underset{\sim}{\alpha}(\underset{\sim}{r},t) \times \underset{\sim}{H}(\underset{\sim}{r},t) \quad , \tag{2.5}$$

where the dot hereafter symbolizes for any quantity the partial derivative with respect to time. Since the unit vector preserves its magnitude, the x-component of the unit magnetization vector is given by

$$\alpha_x = [1 - (\alpha_y^2 + \alpha_z^2)]^{1/2} \quad . \tag{2.6a}$$

The x component has been singled out because the dc magnetic field is applied in the x-direction, and deviations of the saturated magnetization from the x-axis will be small. The y and z components of the equation of motion may be found from an expansion of (2.5) to be

$$\dot{\alpha}_y = -\gamma(\alpha_z H_x - \alpha_x H_z) \tag{2.6b}$$

$$\dot{\alpha}_z = -\gamma(\alpha_x H_y - \alpha_y H_x) \quad . \tag{2.6c}$$

Thus (2.6) constitute the equations of motion of the magnetization for a dc magnetic field applied in the x-direction.

In obtaining components of the total magnetic field $\underset{\sim}{H}$, it is often useful to utilize the following relationship between the magnetic field and the free magnetic energy E :

$$\underset{\sim}{H} = -\frac{1}{M_s} \nabla_\alpha E \quad , \tag{2.7}$$

where ∇_α represents the gradient with respect to the direction cosines of the magnetization. The total magnetic field $\underset{\sim}{H}$ comprises the applied dc and microwave frequency (rf) field terms as well as terms dependent upon $\underset{\sim}{\alpha}$. Because of these terms of $\underset{\sim}{H}$ dependent upon $\underset{\sim}{\alpha}$, the equation of motion [(2.5) or (2.6)] will be nonlinear in $\underset{\sim}{\alpha}$. However, with the application of orthogonal dc and rf magnetic fields and small deviations of $\underset{\sim}{\alpha}$ about static equilibrium, the equations may be linearized. Under the quasi-static approximation to Maxwell's equations ($\nabla \cdot \underset{\sim}{B} = 0$, $\nabla \times H = 0$) there is a uniform solution (uniform precession) to (2.6) and the appropriate magnetostatic boundary conditions, as well as an infinity of spatially-varying solutions.[8] The spatially-dependent solution modes are quite complicated if the exact boundary conditions are matched, but usually it is permissible to make the periodic boundary condition assumption and to regard the modes as plane waves if

$$2\pi/k \ll \text{sample dimensions} \quad .$$

The uniform precession is then often called the $k = 0$ mode.

In the plane wave approximation the general motion of the magnetization is given in the form of a Fourier series expansion of $\underset{\sim}{\alpha}$, namely,

$$\underset{\sim}{\alpha} = \underset{\sim}{\alpha}_0 + \underset{\sim}{\alpha}_s \tag{2.8a}$$

$$\underset{\sim}{\alpha}_s = \sum_{k \neq 0} \underset{\sim}{\alpha}_k \, e^{i\underset{\sim}{k}\cdot\underset{\sim}{r}} \quad , \tag{2.8b}$$

where this expansion is strictly valid only for large k's . These plane wave modes are referred to as spin wave modes--hence the subscript of $\underset{\sim}{\alpha}_s$ in (2.8b). In the above, $\underset{\sim}{\alpha}_k$ is a function of time only and has the form

$$\underset{\sim}{\alpha}_k = \underset{\sim}{a}_k \, e^{i\omega t} + \underset{\sim}{a}_k' \, e^{-i\omega t} \quad , \tag{2.9}$$

which in general may be complex, where the quantity ω is the frequency of the spin waves and the vectors $\underset{\sim}{a}_k$, $\underset{\sim}{a}_k'$ are independent of time. Since the spin wave component of the magnetization $\underset{\sim}{\alpha}_s$ must be real, it follows that

$$\underset{\sim}{\alpha}_{-k} = \underset{\sim}{\alpha}_k^* \quad , \tag{2.10a}$$

and therefore

$$\underset{\sim}{a}_k' = \underset{\sim}{a}_{-k}^* \quad . \tag{2.10b}$$

In general, $\underset{\sim}{\alpha}_s$ will contain pairs of oppositely directed traveling waves, with propagation vectors $\underset{\sim}{k}$ and $-\underset{\sim}{k}$. If nonlinear terms are retained in (2.7) it will be found that terms proportional to the uniform precession $\underset{\sim}{\alpha}_0$ will couple pairs of spin waves $\underset{\sim}{a}_k$ and $\underset{\sim}{a}_{-k}^*$, and that this coupling will lead to exponential growth of pairs of spin waves. For each pair it will be found that

$$|a_k| = |a_{-k}| \quad , \tag{2.11}$$

so that the unstable modes are standing waves.

B. MAGNETIC FIELD COMPONENTS

The total magnetic field $\underset{\sim}{H}$ comprises the following components: the applied dc magnetic field $\underset{\sim}{H}_0$, the pump rf magnetic field $\underset{\sim}{h}_p$, the anisotropy field $\underset{\sim}{H}_a$, the dipolar field $\underset{\sim}{H}_{dip}$, the demagnetizing field $\underset{\sim}{H}_d$, and the exchange field $\underset{\sim}{H}_{ex}$. Figure 2.1 shows the coordinate system employed and gives the direction of the applied magnetic fields and the propagation vector $\underset{\sim}{k}$. The applied dc magnetic field is given by

$$\underset{\sim}{H}_0 = \begin{pmatrix} H_0 \\ 0 \\ 0 \end{pmatrix} \quad . \tag{2.12}$$

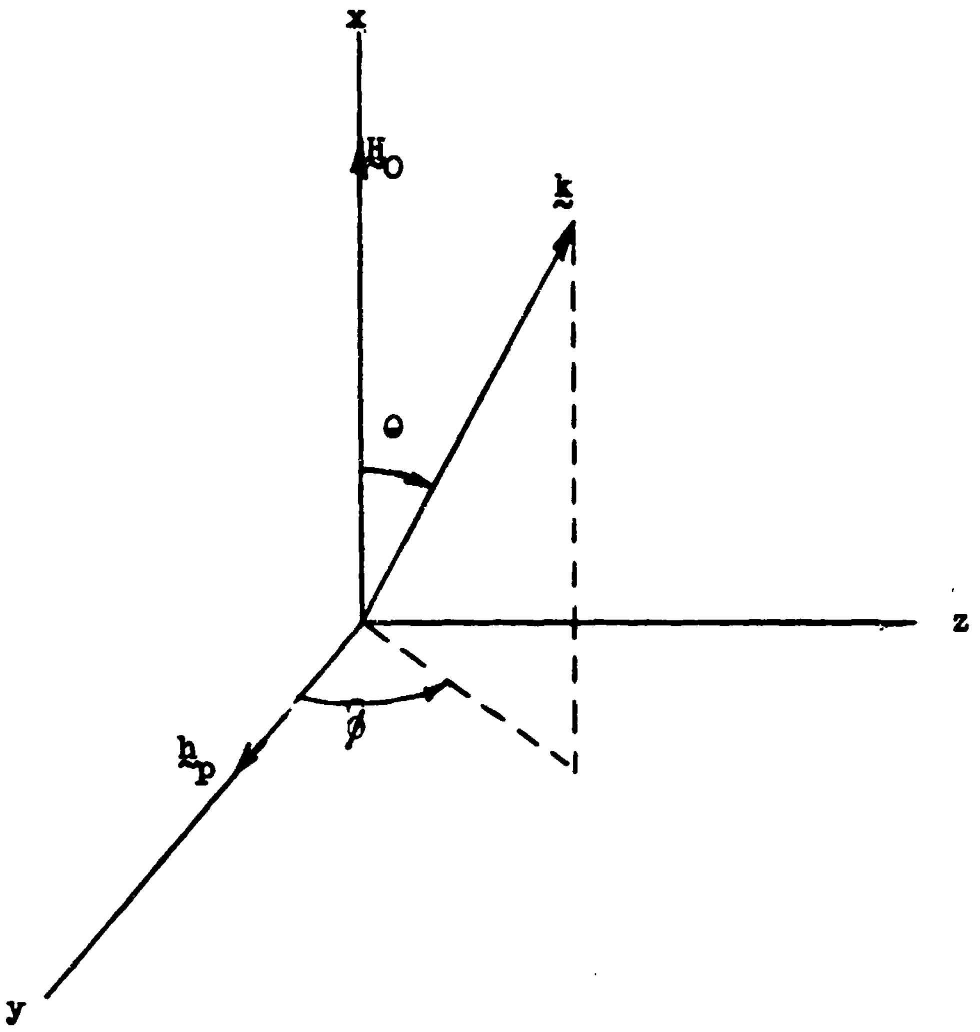

FIG. 2.1--Coordinate system showing direction of applied magnetic fields and propagation vector.

The pump rf magnetic field which is normal to the applied dc magnetic field and is linearly polarized is expressed as

$$\underset{\sim}{h}_p = \begin{pmatrix} 0 \\ h_y \\ 0 \end{pmatrix} , \tag{2.13}$$

where $h_y = h \cos \omega_p t$, h is the maximum amplitude, and ω_p is the frequency of the pump.

The anisotropy magnetic field arises from the crystalline anisotropy energy, which, for a hexagonal crystal, has its origin in magnetic dipole-dipole interaction. From crystal symmetry considerations, the anisotropy energy of a hexagonal crystal is found to be of the form[9]

$$E_a = K_1 \sin^2 \theta' + K_2 \sin^4 \theta' + K_3 \sin^6 \theta' + K_4 \sin^6 \theta' \cos 6\phi' , \tag{2.14}$$

where θ' is the angle the magnetization makes with the "hard" z-axis, and ϕ' is the angle in the basal (x,y) plane. For Zn_2Y the negative constant K_1 in (2.14) is predominant. The energy then assumes the uniaxial form, and when written in terms of the direction cosines of $\underset{\sim}{\alpha}$ becomes

$$E_a = K_1 (1 - \alpha_z^2) . \tag{2.15}$$

Utilizing (2.7), the anisotropy "magnetic" field is defined by

$$\underset{\sim}{H}_a = \begin{pmatrix} 0 \\ 0 \\ - H_A \alpha_z \end{pmatrix} , \tag{2.16}$$

with $H_A = -2K_1/M_s$ defined as the anisotropy field along the "hard" or c-axis.

The demagnetizing and dipolar fields are obtained from the quasi-static approximation to Maxwell's equation written as

$$\nabla \cdot (\mathbf{H} + 4\pi M_s \boldsymbol{\alpha}) = 0 \tag{2.17a}$$

$$\nabla \times \mathbf{H} = 0 \quad . \tag{2.17b}$$

The quasi-static approximation is fulfilled to a good approximation when the dimensions of the ferrite sample are much less than the free space wavelength. The dipolar magnetic field, which is the demagnetizing field for spin waves, is obtained by finding the solution to (2.17) for the spin wave modes (2.8b) which satisfy the periodic boundary conditions. The result obtained is

$$\mathbf{H}_{dip} = -4\pi M_s \sum_{k} \mathbf{k} \, \frac{\mathbf{k} \cdot \boldsymbol{\alpha}_k}{k^2} \, e^{i\mathbf{k}\cdot\mathbf{r}} \quad . \tag{2.18}$$

The demagnetizing field for the uniform $(k = 0)$ mode is obtained from (2.17), together with the exact boundary conditions. For an ellipsoid in a uniform magnetic field the demagnetizing field may be represented by the general expression

$$\mathbf{H}_d = -4\pi M_s \overleftrightarrow{\mathbf{N}} \boldsymbol{\alpha}_0 \quad , \tag{2.19}$$

where $\overleftrightarrow{N}$ is the demagnetizing tensor. For the special case when the applied magnetic fields are along the major ellipsoidal axes of the sample, $\overleftrightarrow{N}$ is diagonal with trace equal to unity. The field may then be expressed as

$$\underset{\sim}{H}_d = - 4\pi M_s \begin{pmatrix} N_x \, \alpha_{0x} \\ N_y \, \alpha_{0y} \\ N_z \, \alpha_{0z} \end{pmatrix} . \tag{2.20}$$

The remaining term of $\underset{\sim}{H}$ is the exchange field $\underset{\sim}{H}_{ex}$, which arises from the quantum mechanical exchange interaction between neighboring atomic spins. The result for a crystal with uniaxial symmetry is

$$\underset{\sim}{H}_{ex} = - \sum_k k^2 e^{i\underset{\sim}{k}\cdot\underset{\sim}{r}} \begin{pmatrix} D_1 \, \alpha_{kx} \\ D_1 \, \alpha_{ky} \\ D_2 \, \alpha_{kz} \end{pmatrix} , \tag{2.21}$$

with

$$D_1 = H_{ex\parallel} \, a^2$$

$$D_2 = H_{ex\perp} \, c^2 \quad ,$$

where $H_{ex\parallel,\perp}$ are scalar quantities of the order of the Weiss field and a,c are the lattice constants of the unit cell. It is apparent from (2.21) that the exchange field becomes especially significant as the wavelength of the propagating wave approaches lattice dimensions.

C. UNIFORM PRECESSION AND SPIN WAVE MODES

The equations of motion are obtained by inserting the total magnetic field $\underset{\sim}{H}$, whose components were developed in the last section, into (2.6). The resulting equations of motion may then be expanded into uniform precession and spin wave mode components by employing (2.8). The uniform mode is separable from the spin wave modes since only the latter contain the spatial dependence. The uniform mode equations become

$$\dot{\alpha}_{0y} = -[\omega_{H_0} + \omega_{H_A} \alpha_{0x} + \omega_M (N_z - N_x) \alpha_{0x}] \alpha_{0z} + \gamma h_z \alpha_{0x} \qquad (2.22a)$$

$$\dot{\alpha}_{0z} = [\omega_{H_0} + \omega_M (N_y - N_x) \alpha_{0x}] \alpha_{0y} - \gamma h_y \alpha_{0x} \quad , \qquad (2.22b)$$

where

$$\omega_{H_0} = \gamma H_0$$

$$\omega_{H_A} = \gamma H_A$$

$$\omega_M = \gamma 4\pi M_s \quad .$$

Also, the equations for the k^{th} spin wave mode are found to be

$$\begin{aligned}\dot{\alpha}_{ky} = & -\omega_{H_0}\,\alpha_{kz} + \gamma h_z\,\alpha_{kx} - \omega_{H_A}\,(\alpha_{0x}\,\alpha_{kz} + \alpha_{0z}\,\alpha_{kx}) \\ & + \omega_M\,(N_x\,\alpha_{0x}\,\alpha_{kz} - N_z\,\alpha_{0z}\,\alpha_{kx}) \\ & + \frac{\omega_M}{k^2}\,(k_x\alpha_{0z} - k_z\,\alpha_{0x})\,(k_x\,\alpha_{kx} + k_y\,\alpha_{ky} + k_z\,\alpha_{kz}) \\ & + \gamma D_1\,k^2\,\alpha_{0z}\,\alpha_{kx} - \gamma D_2\,k^2\,\alpha_{0x}\,\alpha_{kz}\end{aligned} \tag{2.23a}$$

$$\begin{aligned}\dot{\alpha}_{kz} = & \;\omega_{H_0}\,\alpha_{ky} - \gamma h_y\,\alpha_{kx} + \omega_M\,(N_y\,\alpha_{0y}\,\alpha_{kx} - N_x\,\alpha_{0x}\,\alpha_{ky}) \\ & + \frac{\omega_M}{k^2}\,(k_y\,\alpha_{0x} - k_x\,\alpha_{0y})\,(k_x\,\alpha_{kx} + k_y\,\alpha_{ky} + k_z\,\alpha_{kz}) \\ & + \gamma D_1\,k^2\,(\alpha_{0x}\,\alpha_{ky} - \alpha_{0y}\,\alpha_{kx}) \quad .\end{aligned} \tag{2.23b}$$

Here nonlinear terms containing the product of the uniform precession and the spin wave components of $\underset{\sim}{\alpha}$ are retained, but terms higher than first order in α_k are neglected. This is a good approximation since the unstable spin waves must build up from thermal amplitudes. It is through the terms in (2.23) containing the uniform precession that energy is coupled from the uniform mode to the spin wave modes. The latter eventually will be found to go unstable when the uniform precession angle reaches a critical amplitude.

Before the uniform mode (2.22) and spin wave mode (2.23) equations can be solved, it is necessary to utilize (2.6a) to eliminate the x-component dependence of the magnetization. By inserting relation (2.8a) into (2.6a), and retaining only first degree terms in the spin wave amplitudes as above, the following relations are obtained for the uniform and spin wave mode components of the magnetization along the x-direction:

$$\alpha_{0x} = (1 - \alpha_{0y}^2 - \alpha_{0z}^2)^{1/2} \tag{2.24a}$$

$$\alpha_{kx} = -(\alpha_{0y}\,\alpha_{ky} + \alpha_{0z}\,\alpha_{kz})\,\alpha_{0x}^{-1} \quad . \tag{2.24b}$$

Since $\alpha_{0y}^2 + \alpha_{0z}^2$ is less then unity, then α_{0x} may be expanded in a binomial series in powers of α_{0y}^2 and α_{0z}^2 . For purposes of solving the spin wave equations, the expanded form of (2.24) is substituted into (2.23), thus obtaining the spin wave mode equations of motion for α_{ky} and α_{kz} . The resulting equations are linear in the spin wave direction cosines, but contain terms which are modulated by the uniform precession direction cosines. Such equations are of the Matthieu-Hill type, and instability thresholds will be found. Since substitution of (2.24) into (2.23) leads to the appearance of higher powers of α_{0y} and α_{0z} , instabilities of higher than first order are to be expected.

D. SOLUTION OF UNIFORM PRECESSION EQUATION

The solution of the uniform precession mode is necessary to determine the relation between the driving magnetic field and the precession angle of the magnetization. The simple solution is found by letting $\alpha_x = 1$ in (2.22), giving

$$\dot{\alpha}_{0y} = -\omega_1\,\alpha_{0z} + \gamma h_z \tag{2.25a}$$

$$\dot{\alpha}_{0z} = \omega_2\,\alpha_{0y} - \gamma h_y \quad , \tag{2.25b}$$

where

$$\omega_1 = \omega_{H_A} + \omega_{H_0} + \omega_M (N_z - N_x)$$

$$\omega_2 = \omega_{H_0} + \omega_M (N_y - N_x)$$

and the ferromagnetic resonance frequency is given by

$$\omega_0 = (\omega_1 \omega_2)^{1/2} \quad .$$

For the special case of a disk lying in the easy plane of the crystal, the demagnetizing factor in the plane of the disk is given by

$$N_y = N_x = N_{\|} \quad ,$$

and the solution to (2.25) is found to be

$$\alpha_{0y} = \frac{\gamma\omega_1 k_1}{\omega_0^2} h \cos \omega_p t = k_1 \frac{h_y}{H_0} \tag{2.26a}$$

$$\alpha_{0z} = \frac{\gamma\omega_p k_1}{\omega_0^2} h \sin \omega_p t \quad , \tag{2.26b}$$

where

$$k_1 = \frac{1}{1 - \left(\frac{\omega_p}{\omega_0}\right)^2} \quad .$$

For operation on ferromagnetic resonance it would be necessary to include phenomenological damping in these equations by letting $\omega_0 \rightarrow \omega_0 + i\eta_0$. But with the pump frequency significantly below ferromagnetic resonance, damping has negligible effect on either the magnitude or the phase of $\underset{\sim}{\alpha}$. In fact, it can be shown that the magnitude of the precession angle off resonance $(\omega_p^2 \ll \omega_0^2)$ is $1/Q_0$ times that on resonance for the same rf field strength. This factor Q_0 is related to the phenomenological damping parameter η_0 by $\eta_0 = \omega_0/2Q_0$.

The ratio of the magnitudes of α_{0z} to α_{0y} gives a measure of the confinement of the motion of the magnetization to the easy plane. This ratio is called the inverse ellipticity of the uniform mode and becomes

$$e^{-1} = \frac{|\alpha_{0z}|}{|\alpha_{0y}|} = \frac{\omega_p}{\omega_1} \quad . \tag{2.27}$$

Using typical experimental values of the parameters for Zn_2Y in (2.27), a value for the inverse ellipticity of 0.044 is obtained. This indicates that the motion of the magnetization is confined almost exclusively to the easy plane. This is not surprising, considering the large anisotropy field of Zn_2Y . To the same approximation that the motion of the magnetization is in the easy plane, the value of k_1 may be taken to be unity. Thus from (2.26a) it is seen that, to first order, α_{0y} becomes just the ratio of the applied rf and dc magnetic fields.

Since α_{0y} is by far the dominant component of the magnetization, an approximate higher order solution for the uniform precession is obtained by letting $\alpha_{0z} = 0$ in (2.22). Thus for the special case of a disk in the easy plane, the relation

$$\alpha_{0y}/\alpha_{0x} = h_y/H_0 = \left(h/H_0\right)\cos \omega_p t \tag{2.28a}$$

is obtained as a solution for the uniform mode. The ratio defined by

$$A_p = h/H_0 \tag{2.28b}$$

will hereinafter be referred to as the <u>pumping angle</u>.

In order to solve (2.28a) for α_{0y}, the LHS of (2.28a) may first be expanded in a power series of α_{0y}, since $\alpha_{0y} < 1$. The method of successive approximation demonstrates that α_{0y} may be expressed as a Fourier series of odd harmonic terms in the pump frequency ω_p. The result of the second iteration is

$$\alpha_{0y}^{(2)} = A_{m_0} \cos \omega_p t + A_{m_1} \cos 3\omega_p t + A_{m_2} \cos 5\omega_p t + \ldots, \tag{2.29a}$$

where

$$\begin{aligned} A_{m_0} &= A_p - \frac{3}{8} A_p^3 - \frac{15}{64} A_p^5 + \ldots \\ A_{m_1} &= - \frac{1}{8} A_p^3 - \frac{15}{128} A_p^5 + \ldots \end{aligned} \tag{2.29b}$$

Since the pumping angle A_p is usually very small $(A_p \ll 1)$, then A_{m_0} and A_{m_1} are given approximately by the first term in the expansion for each case.

E. DERIVATION OF EXPRESSIONS FOR THE INSTABILITY THRESHOLDS

The equations from which the thresholds of spin wave instabilities are to be calculated are obtained from (2.23) and (2.24). At this point the assumption is made that the motion of the uniform precession of the magnetization is confined to the x-y or easy plane (see Fig. 2.1). This amounts to neglecting α_{0z} in comparison with α_{0y}. Assuming also that $\alpha_{0y} \ll 1$, it is then possible to express h_y by a power series in α_{0y} [see (2.28)]. The equations of motion, greatly simplified by these assumptions, may be written as

$$\dot{\alpha}_{ky} = a_0 \alpha_{kz} + a_1 \alpha_{ky} \tag{2.30a}$$

$$\dot{\alpha}_{kz} = b_0 \alpha_{kz} + b_1 \alpha_{ky} \quad , \tag{2.30b}$$

with coefficients a_0, a_1, b_0, b_1 expanded in powers of the uniform precession amplitude α_{0y} as follows:

$$\frac{a_0}{\omega_M} = a_{00} + a_{02}\,\alpha_{0y}^2 + a_{04}\,\alpha_{0y}^4 + \dots$$

$$\frac{a_1}{\omega_M} = -\frac{b_0}{\omega_M} = a_{10} + a_{11}\,\alpha_{0y} + a_{12}\,\alpha_{0y}^2 + a_{14}\,\alpha_{0y}^4 + \dots \tag{2.30c}$$

$$\frac{b_1}{\omega_M} = b_{10} + b_{11}\,\alpha_{0y} + b_{12}\,\alpha_{0y}^2 + b_{14}\,\alpha_{0y}^4 + \dots \quad .$$

The coefficients in the expansions (2.30c) are

$$
\begin{aligned}
a_{00} &= -(x + d + p \sin^2 \Theta \sin^2 \phi) \\
a_{02} &= 4a_{04} = \tfrac{1}{2}(-N_{\|} + d + p + \sin^2 \Theta \sin^2 \phi) \\
a_{10} &= -2a_{12} = -8a_{14} = -\tfrac{1}{2} \sin^2 \Theta \sin 2\phi \\
a_{11} &= \tfrac{1}{2} \sin 2\Theta \sin \phi \\
b_{10} &= x + d + \sin^2 \Theta \cos^2 \phi \\
b_{11} &= -\sin 2\Theta \cos \phi \\
b_{12} &= x + \tfrac{1}{2} N_{\|} + \tfrac{1}{2} d + \cos^2 \Theta - \tfrac{1}{2} \sin^2 \Theta \cos^2 \phi \\
b_{14} &= x + \tfrac{3}{8} d + \tfrac{5}{8} N_{\|} + \tfrac{1}{2} \cos^2 \Theta - \tfrac{1}{8} \sin^2 \Theta \cos^2 \phi \quad ,
\end{aligned}
\tag{2.30d}
$$

where

$$
\begin{aligned}
x &= \frac{H_0 - N_{\|} 4\pi M_s}{4\pi M_s} = \frac{H}{4\pi M_s} \\
p &= \frac{H_A}{4\pi M_s} \\
d &= \frac{Dk^2}{4\pi M_s} \quad .
\end{aligned}
\tag{2.30e}
$$

Equations (2.30) show that the coefficients in the spin wave equation of motion are functions of time. Eliminating α_{kz} from (2.30a) and (2.30b) and utilizing the relation $b_0 = -a_1$, results in

$$\ddot{\alpha}_{ky} - \frac{\dot{a}_0}{a_0}\dot{\alpha}_{ky} + \left(-a_1^2 - b_1 a_0 - \dot{a}_1 + \frac{a_1 \dot{a}_0}{a_0}\right)\alpha_{ky} = 0 \quad . \qquad (2.31)$$

If α_{ky} were eliminated instead of α_{kz}, then the differentiated (dotted) coefficients would be different. However, it will presently be shown that these dotted coefficients may be neglected. In this case the differential equation has the same form for either α_{ky} or α_{kz}. Equations (2.9) and (2.10) yield:

$$\underset{\sim}{\alpha}_k = \underset{\sim}{a}_k e^{i\omega t} + a^*_{-k} e^{-i\omega t} \quad . \qquad (2.32)$$

The uniform mode amplitude α_{0y} appearing in the coefficients of the differential equation (2.31) is given by (2.29). If only the dominant first harmonic pump frequency component of α_{0y},

$$\alpha_{0y} = \frac{A_{m0}}{2}\left(e^{i\omega_p t} + e^{-i\omega_p t}\right) \quad , \qquad (2.33)$$

is used, (2.31) is a Matthieu equation.

From (2.30), (2.31), and (2.33) it is seen that terms like $a_1^2 \alpha_{ky}$ or $b_1 a_0 \alpha_{ky}$ are proportional to $\omega_M^2 a_k$, while terms like $(a_1 \dot{a}_0 / a_0)\alpha_{ky}$ or $\dot{a}_1 \alpha_{ky}$ are proportional to $i\omega_p \omega_M a_k$. The latter terms may be neglected since they are smaller by the factor $\omega_p/\omega_M \ll 1$ as well as being in quadrature with the former terms. The term containing $\dot{\alpha}_{ky}$ is proportional to $\omega \omega_p$ and may also be neglected since $\omega \omega_p \ll \omega_M^2$. This is not a loss term, since two time derivatives are involved. With the above negligible terms omitted, and with the inclusion of phenomenological damping, (2.31) may now be written as

$$\ddot{\alpha}_{ky} + \frac{\omega}{Q}\dot{\alpha}_{ky} + C\alpha_{ky} = 0 \quad , \tag{2.34}$$

where

$$C = -a_1^2 - b_1 a_0 \quad .$$

From (2.30c) it is possible to express C as a series in powers of α_{0y} as follows:

$$C = C_0 + C_1 \alpha_{0y} + C_2 \alpha_{0y}^2 + C_3 \alpha_{0y}^3 + \ldots \quad , \tag{2.35}$$

where

$$\frac{C_0}{\omega_M} = - a_{10}^2 - b_{10} a_{00}$$

$$\frac{C_1}{\omega_M} = - 2 a_{10} a_{11} - b_{11} a_{00}$$

$$\frac{C_2}{\omega_M} = - 2a_{10} a_{12} - a_{11}^2 - b_{12} a_{00} - b_{10} a_{02}$$

$$\frac{C_3}{\omega_M} = - 2a_{11} a_{12} - b_{11} a_{02}$$

$$\frac{C_4}{\omega_M} = - 2 a_{10} a_{14} - a_{12}^2 - b_{10} a_{04} - b_{12} a_{02} - b_{14} a_{00} \quad .$$

Spin wave thresholds are now determined by substituting (2.32) and (2.33) into (2.34). Taking spin waves at the frequency

$$\omega = n\omega_p/2 \tag{2.36}$$

and neglecting off-resonant frequency terms, a secular relation for α_{ky} and α^*_{-ky} is obtained, and from this the instability threshold is found. This procedure may be followed for every order n . In doing this, only that term in (2.35) which has the same degree as the order of the instability is found to be relevant.

Consider as an example the calculation of the first order threshold. By making the above substitutions and keeping only constant and fundamental pump frequency terms in C , then (2.34) becomes

$$\begin{aligned} &\left(-\omega^2 + C_0 + C_2 \frac{A^2_{m_0}}{2} + \frac{3}{8} C_4 A^4_{m_0} + \ldots + \frac{i\omega^2}{Q} \right) a_{ky} \\ &+ \left(C_1 \frac{A_{m_0}}{2} + \frac{3}{8} C_3 A^3_{m_0} + \ldots \right) a^*_{-ky} = 0 \end{aligned} \tag{2.37}$$

and its adjoint (complex conjugate with k → -k), subject to condition (2.36) for $n = 1$. Terms from the uniform precession amplitude up to fourth degree are shown in order to indicate the approximate nature of the threshold calculations. The threshold is determined by setting the determinant of the coefficients of the spin wave amplitudes (a_{ky} , a^*_{-ky}) in (2.37) and its adjoint equal to zero, giving

$$\left| C_1 \frac{A_{m_0}}{2} + C_4 \frac{3}{8} A^3_{m_0} + \ldots \right| = \left| -\omega^2 + C_0 + C_2 \frac{A^2_{m_0}}{2} + \ldots + \frac{i\omega^2}{Q} \right| . \tag{2.38}$$

The resonance condition in (2.38),

$$\omega^2 = C_0 + C_2 A_{m_0}^2/2 + \ldots \quad , \qquad (2.39)$$

is seen to depend upon the uniform precession amplitude. If the uniform precession amplitude is small (the usual practical situation), the RHS of (2.39) may be reduced to $C_0 = \omega_k^2$, where ω_k is the spin wave frequency from linear theory. Then the first order threshold is found from (2.38) to be approximately

$$(A_p)_{cr}^{(1)} = \min \frac{2}{|C_1|} \left[(-\omega^2 + \omega_k^2)^2 + \left(\frac{\omega^2}{Q}\right)^2 \right]^{1/2} \quad , \qquad (2.40)$$

subject to the condition

$$\omega = \omega_p/2 \quad .$$

Here and hereafter the order of the threshold will be indicated by the superscript on A_p .

The higher order thresholds are determined in a similar manner. The thresholds of even order $n = 2,4$ are given by

$$(A_p)_{cr}^{(n)} = \min 2 \left(\frac{\left[(-\omega^2 + \omega_k^2)^2 + \left(\frac{\omega^2}{Q}\right)^2 \right]^{1/2}}{|C_n|} \right)^{1/n} \quad . \qquad (2.41)$$

To find the spin wave with the lowest threshold, (2.41) must be minimized with respect to k, θ, ϕ subject to the condition (2.36). Each order threshold must be considered separately in the minimization process, since C_n as well as ω_k is different for each case. In determining thresholds of odd order higher than the first, it is necessary to take into account the effect of higher odd harmonic terms in the uniform precession amplitude upon the modulation of the spin wave frequency ω_k . The even order thresholds are unaffected by these odd harmonic terms, however, because they contribute only off-resonant frequency terms, which are negligible. The threshold expression for the third order then becomes

$$(A_p)^{(3)}_{cr} = \min 2 \left(\frac{\left[(-\omega^2 + \omega_k^2)^2 + \left(\frac{\omega^2}{Q} \right)^2 \right]^{1/2}}{|C_3 - C_1/2|} \right)^{1/3} , \qquad (2.42)$$

subject to

$$\omega = \frac{3}{2} \omega_p \quad .$$

The higher odd order thresholds are similarly affected by the corresponding odd harmonic terms in the uniform precession amplitude (2.29). However, only thresholds through fourth order are being considered here.

F. OPTIMIZATION AND CALCULATION OF THE THRESHOLDS

In the optimization of spin wave thresholds it will be assumed as an approximation that the phenomenological damping parameter ω/Q is independent of k, θ and ϕ . Hence, for each threshold calculation it will be assumed that Q is a constant.

1. Minimum Thresholds at Spin Wave Resonance

It is clear from the threshold expressions obtained in the previous section that the lowest thresholds occur when the condition

$$\omega_k = \omega \tag{2.43}$$

is satisfied. This means that the pumping of the instability at ω occurs at the spin wave resonant frequency ω_k, i.e., within the spin wave manifold.

The resonant frequency of the spin wave modes given by $\omega_k = C_0^{1/2}$ may be expanded with the aid of (2.30) and (2.35) to yield

$$\omega_k = \omega_M \, [x'(x' + p) + \sin^2 \Theta(x' + p \cos^2 \phi)]^{1/2} \quad . \tag{2.44}$$

Recall that

$$x' = x + d \quad ,$$

and

$$x = H/4\pi M_s$$

$$d = D\,k^2/4\pi Ms$$

$$p = H_A/4\pi M_s \quad ,$$

from (2.31). When plotted as a function of k for a given value of x as shown in Fig. 2.2a, (2.44) describes a continuum of resonant spin wave frequencies, the spin wave manifold. It may be seen from (2.44) that the dependence of ω_k upon ϕ is due to the presence of anisotropy. The

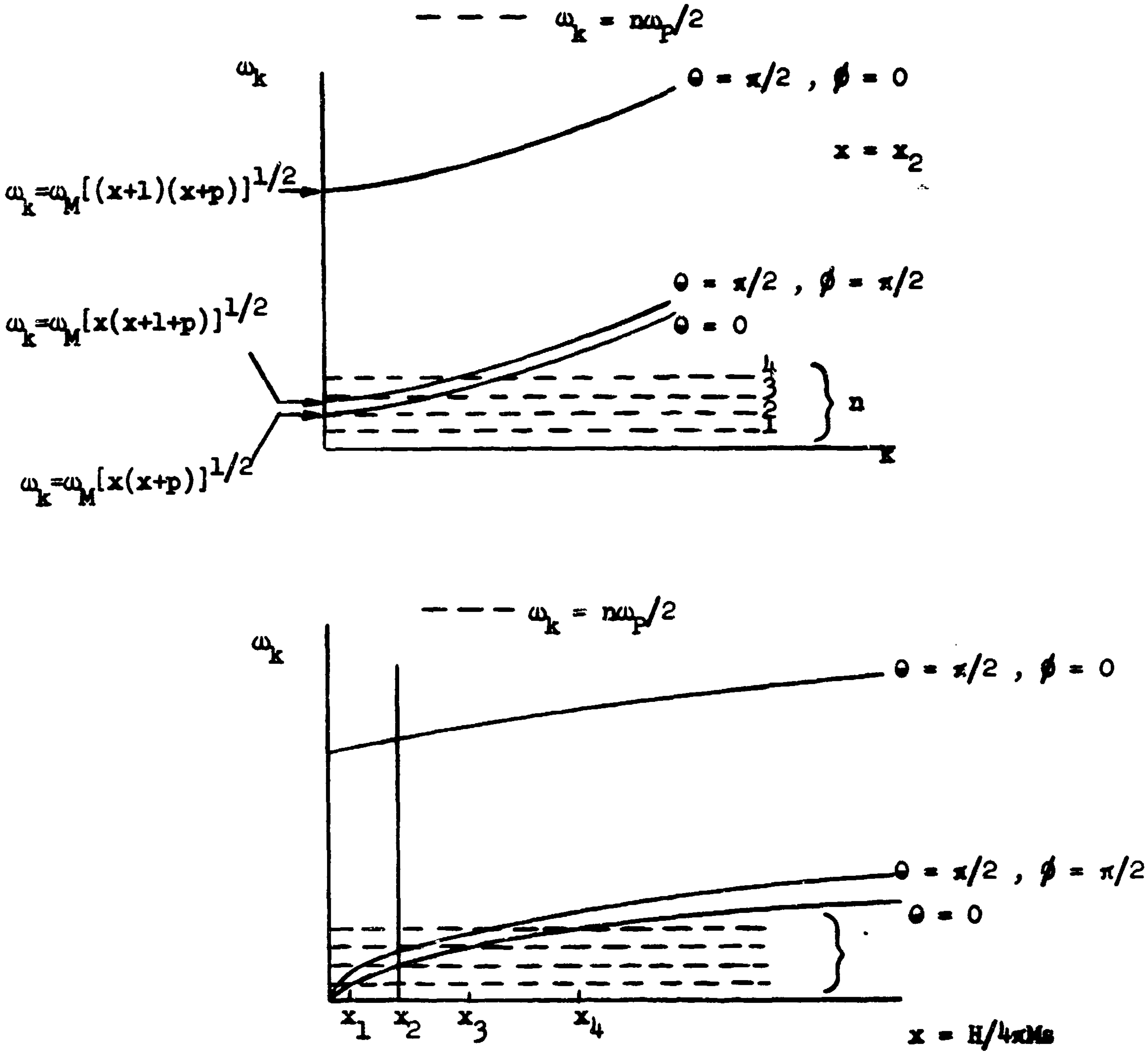

FIG. 2.2--a. Sketch of the spin wave manifold, showing dispersion curves in terms of the propagation angles θ and ϕ.

b. Sketch of the $k = 0$ intercepts of the spin wave manifold as a function of normalized dc field.

The dashed lines in both figures represent the frequency conditions (2.36).

dashed lines indicate the required frequencies for instabilities of various orders. For the case shown, a resonant instability of order one is forbidden; and the k values for higher order instabilities are found from the intersections of the dashed lines with the dispersion curves. Equation (2.44) shows that the position of the manifold shifts with the dc field. This dependence is shown in Fig. 2.2b, as a function of the normalized dc field x, for the $k = 0$ intercepts of the manifold. In this figure the abscissa $x = x_2$ represents the normalized field in Fig. 2.2a, where the second order resonant instability is just on the edge of the forbidden zone. As Fig. 2.2b shows, the number of resonant instabilities varies with the dc field. The critical fields at which the various instabilities "come in" at $k = 0$ are found from the intersections of the dashed and solid curves. For the general case of spin waves with $k = 0$, these critical points are found, with the aid of (2.36) and (2.44) to be

$$n^2 q^2 = x'(x' + p) + (x' + p \cos^2 \phi) \sin^2 \theta \quad , \qquad (2.45a)$$

where the spin wave resonance condition (2.43) has been invoked, and the symbol

$$q = \omega_p/2\omega_M$$

has been defined for convenience. Since the pump frequency is far below ferromagnetic resonance, then $q \ll 1$.

Since $x' \geq 0$ and $p \geq 0$, (2.45) requires that

$$|\sin \theta \cos \phi| \leq nq\, p^{-1/2} \quad , \qquad (2.45b)$$

which places some restrictions on the permissible values of Θ and ϕ. The RHS of (2.45) is much less than unity for the parameters to be used. Hence, either Θ is near zero or else ϕ is near $\pi/2$. The reason for this is apparent from Fig. 2.2a, which applies to the case $q \ll 1$, $p \gg 1$.

Assuming a pump frequency of $\omega_p/2\pi = 1.32$ kMc and the parameter values for Zn_2Y at $29^\circ C$, given in Appendix A, the maximum allowable values of x' may be determined from (2.45) by setting $\Theta = 0$. The results for these maximum values of x' are:

$$\begin{aligned} \text{for } n &= 1 \qquad & x_1' &= 0.00250 \\ n &= 2 & x_2' &= 0.00998 \\ n &= 3 & x_3' &= 0.0224 \\ n &= 4 & x_4' &= 0.0396 \quad . \end{aligned} \tag{2.46a}$$

Recall that

$$x' = x + d \quad ,$$

where $x = H/4\pi M_s$ is the normalized internal magnetic field and $d = Dk^2/4\pi M_s$ is the normalized exchange field. It is apparent from Figs. 2.2a and 2.2b that, within the spin wave manifold, x' (and hence the internal magnetic field) is small because the pump frequency is near the bottom of the spin wave manifold. For the $k = 0$ intercepts of the manifold (shown in Fig. 2.2b) the maximum values of $x' = x_n'$ given above become maximum values of $x = x_n$. The corresponding values of the applied (external) magnetic field H_0 then become

$$H_{0n} = (x_n + N_{\|})\, 4\pi M_s \quad . \tag{2.46b}$$

These fields will be "passed through" during the experimental measurements of instability thresholds in order to see if any spin wave instability effects are present (see Chapter VI). Thus, as x is increased (by increasing the dc magnetic field H_0) above a certain x_n, the n^{th} order spin wave instability is forced off resonance. The x_n then, corresponds to the dc field at which the n^{th} order spin wave instability first becomes allowed on resonance. Since these maximum values of x' are so small, it will be quite permissible later to neglect x and d in any term containing p, since $p > 1$.

Each threshold will now be considered separately and optimized with respect to the four parameters ω, Θ, ϕ, k. The first order threshold at spin wave resonance $(\omega = \omega_k)$ in terms of these four parameters is found from (2.40) to be

$$(A_p)_{cr}^{(1)} = \min \frac{2q^2}{Q} \frac{1}{(x' + p) \cos \phi \sin 2\Theta} \qquad (2.47)$$

subject to (2.45) for $n = 1$. To minimize (2.47) as it stands would require $\phi = 0$ and $\Theta = \pi/4$. However, the frequency condition (2.45) precludes this combination of ϕ, Θ by specifying that either Θ or $\pi/2 - \phi$ is small. Since the denominator of (2.47) is doubly periodic in Θ, only values $0 \leq \Theta \leq \pi/4$ ought to be considered. Moreover, from (2.45) it is clear that a smaller Θ permits a large value of $\cos \phi$; or, conversely, a small value of $\pi/2 - \phi$ permits a large value of $\sin 2\Theta$. Minimization then reduces to consideration of the following two cases: (1) Θ small, $\phi = 0$ and (2) $\Theta = \pi/4$, ϕ near $\pi/2$. The former yields the lowest threshold and is given approximately by

$$(A_p)_{cr}^{(1)} = \frac{q^2}{Qp^{1/2} [q^2 - x'(x' + p)]^{1/2}} \qquad . \qquad (2.48)$$

It is evident from (2.48) that the actual minimum threshold occurs when $x' = x + d$ is smallest, that is, when $d \approx 0$. Therefore, those spin waves which go unstable must be those of lowest $k \approx 0$. This tends to violate the original plane wave assumption for large k. The method is justified in practice, though, since measured thresholds have been found to agree with the theory.[3]

The second order threshold at spin wave resonance is obtained from (2.41) by proceeding in a similar manner. The result is

$$(A_p)^{(2)}_{cr} = \min\left(\frac{16\, q^2}{Q\left[\cos^2\Theta\left(p+d+x-1-\frac{N_\parallel}{2}\right)-\sin^2\Theta\cos^2\phi\,(p+d+1)+(N_\parallel+x)(x+d+p/2)+1+\frac{N_\parallel}{2}\right]}\right)^{1/2} . \tag{2.49}$$

Since, by (2.45b), $\sin\Theta\cos\phi$ is a very small quantity, then clearly the minimum threshold occurs for $\Theta = 0$. Inserting $\Theta = 0$ into (2.49) gives

$$(A_p)^{(2)}_{cr} = \left(\frac{16\, q^2}{Qp\left(1+\frac{N_\parallel}{2}\right)}\right)^{1/2} \tag{2.50}$$

where x, d terms have been neglected since $x + d < 0.01$. For $\Theta = 0$, it is seen from (2.45a) that d may be large when $x \ll x_n'$. This means that the unstable spin waves may have large k, by contrast with the first order case. From (2.50) the threshold is independent of k. This result for the on-resonance second order threshold for spin waves is compatible with the on-resonance threshold result obtained by Schlömann, et al.,[10] for the case of an infinitely thin disk $(N_\parallel = 0)$.

The third order threshold at spin wave resonance is found from (2.42) to be

$$(A_p)_{cr}^{(3)} = \min\left(\frac{72\ q^2}{Q \sin 2\Theta \cos \phi \left(p + d + \frac{x - N_x}{2}\right)}\right)^{1/3} . \qquad (2.51)$$

The denominator has the same form as the first order threshold. Hence, the minimum occurs at $\phi = 0$, Θ small, and $d \approx 0$ -- giving, with the usual assumptions,

$$(A_p)_{cr}^{(3)} = \left(\frac{36\ q^2}{Qp^{1/2}\ [9q^2 - x\ (x + p)]^{1/2}}\right)^{1/3} . \qquad (2.52)$$

The fourth order threshold at spin wave resonance is determined from (2.41) to be

$$(A_p)_{cr}^{(4)} = \min\left(\frac{512\ q^2}{Q(N_{\|} + x)\left[1 + \frac{3}{4}(p + d) - \sin^2\Theta\left(\frac{1}{4} + \cos^2\phi\right)\right]}\right)^{1/4} , \qquad (2.53)$$

where second order product terms in d, x, $N_{\|}$ have been neglected. Employing the same type of reasoning as used for the second order threshold above, the minimum of (2.53) is found to occur at $\phi = 0$, $\Theta = 0$, and d large. The resulting fourth order threshold becomes approximately

$$(A_p)_{cr}^{(4)} = \left(\frac{512\ q^2}{Q\left(N_{\|} + x\right)\left(1 + \frac{3}{4}\ p\right)}\right)^{1/4} . \qquad (2.54)$$

2. Minimum Thresholds For Off-Resonance Spin Waves

Recall from the last section that when x' is increased above a certain x_n' (by increasing the dc magnetic field), the n^{th} order spin wave instability is forced off resonance. In this case, for a given n, the relationship between the frequency ω at which the instability is being pumped and the resonant spin wave frequency ω_k is

$$\omega_k > \omega = n\omega_p/2 \quad . \tag{2.55}$$

The first order threshold for off-resonance spin waves may be found from (2.40) by substituting the value for C_1 as was done for the on-resonance thresholds. The result is

$$(A_p)^{(1)}_{cr} = \min \frac{2\left[(-\omega^2 + \omega_k^2)^2 + \left(\frac{\omega^2}{Q}\right)^2\right]^{1/2}}{\omega_M^2(x' + p)\cos\phi \sin 2\theta} \quad , \tag{2.56}$$

subject to the parametric frequency condition

$$\omega = \omega_p/2 \quad ,$$

where the off-resonant spin wave condition (2.55) must be satisfied. The frequency condition (2.55) places only a lower bound on ω_k ; and (2.56) is to be minimized with respect to k,θ,ϕ , subject to this side condition. From (2.44), condition (2.55) will be satisfied for all spin waves if it is satisfied for the $\theta = 0$, $k = 0$ spin waves. Therefore (2.56) may be minimized independently with respect to k,θ , and ϕ . From (2.46) the condition on x corresponding to (2.55) is

$$x > 0.0025 \tag{2.57}$$

for the first order process and the parameters used before.

Given that $p \gg x'$, the only substantial dependence of (2.56) upon k occurs in the numerator through ω_k in the resonance term. From Eq. (2.44) or Fig. 2.2a it is apparent that (2.56) is a minimum for $k \approx 0$. To simplify the calculation, the assumption will now be made that ω is sufficiently far off resonance (below ω_k) that

$$(-\omega^2 + \omega_k^2)^2 \gg \left(\frac{\omega^2}{Q}\right)^2 \quad . \tag{2.58}$$

Thus (2.56) may be written approximately as

$$(A_p)^{(1)}_{\substack{cr \\ \text{off res}}} = mi \; \frac{2\left[x - \frac{q^2}{p} + \sin^2\theta\left(\frac{x}{p} + \cos\phi\right)\right]}{\cos\phi \sin 2\theta} \quad . \tag{2.59}$$

The minimum of (2.59) occurs for $\phi = 0$ and for θ small, with

$$\theta_{opt} \approx (x - q^2/p)^{1/2} \quad . \tag{2.60}$$

Inserting (2.60) into (2.59) yields the following minimum threshold expression for frequencies far off spin wave resonance:

$$(A_p)^{(1)}_{\substack{cr \\ \text{off res}}} = 2\theta_{opt} = 2(x - q^2/p)^{1/2} \quad . \tag{2.61}$$

The second order threshold off spin wave resonance may be found from (2.41) by substituting the value of C_2 , as was done in the case of the on-resonance thresholds of second order. The result obtained is

$$(A_p)^{(2)}_{cr} = \min \left\{ \frac{4\left[(-\omega^2 + \omega_k^2)^2 + \left(\frac{\omega^2}{Q}\right)^2 \right]^{1/2}}{\omega_M^2 \left[\cos^2\Theta \left(p+d + x-1 - \frac{N_\parallel}{2}\right) - \sin^2\Theta \cos^2\phi (p+d+1) + (N_\parallel + x)(x+d+p/2)+1 + \frac{N_\parallel}{2} \right]} \right\}^{1/2} , \tag{2.62}$$

subject to the parametric frequency condition

$$\omega = \omega_p \quad ,$$

where the off-resonance spin wave condition (2.55) must be satisfied. From (2.46) the condition on x is now

$$x > 0.00998 \quad . \tag{2.63}$$

As in the case of the first order process, (2.62) may be minimized independently with respect to the parameters k, Θ, ϕ .

The numerator of (2.62) is a minimum when $\Theta = 0$ and $k = 0$, since at these parameter values ω_k is a minimum. The denominator (discussed in the preceeding section) is a maximum at $\Theta = 0$ and is insensitive to the value of k . Therefore, the minimum occurs for $\Theta = 0$ and $k \approx 0$. Neglecting terms in the denominator which do not contain p , (2.62) becomes

$$\underset{\text{off res}}{(A_p)^{(2)}_{cr}} = \left\{ \frac{4\left[(-\omega^2 + \omega_k^2)^2 + \left(\frac{\omega^2}{Q}\right)^2 \right]^{1/2}}{\omega_M^2 \, p \left(1 + \frac{N_\parallel}{2}\right)} \right\}^{1/2} , \tag{2.64}$$

where

$$\omega_k^2 = \omega_M^2 (p + x)x \quad .$$

If the unstable spin wave is far off resonance, Eq. (2.58) applies, and (2.64) becomes

$$(A_p)_{cr}^{(2)} = 2\left(\frac{x - 4q^2/p}{1 + N_{\|}/2}\right)^{1/2} \quad , \qquad (2.65)$$

which is independent of the spin wave Q . It is interesting that this result has the same form as (2.61). It differes in the allowed values of x , which are given by (2.63), rather than by (2.58). Consideration of off-resonance thresholds for processes of higher order will be shown to be unnecessary.

3. Spin Wave Q

It has been assumed as an approximation in each of the above minimizations that the phenomenological damping parameter ω/Q is the same for all spin waves--i.e., the same for all k,θ,ϕ . The relaxation frequency η_k is related to the phenomenological damping parameter by

$$\eta_k = \omega/2Q \quad . \qquad (2.66)$$

This parameter is usually defined in terms of the spin wave linewidth ΔH_k as follows:

$$\eta_k = \gamma\Delta H_k/2 \quad . \qquad (2.67)$$

Thus from (2.6[illegible]) and (2.6[illegible]) an expression for the spin wave Q becomes

$$Q = \omega/(\gamma\Delta H_k) \quad . \tag{2.68}$$

For polycrystalline yttrium iron garnet with aluminum substitutions (YAlIG) , the spin wave linewidth is found to be proportional to frequency for $\theta = 0$ spin waves.[11] The spin wave linewidth in single crystal YIG at the higher frequencies is also proportional to frequency; but at the lower frequencies, due to splitting processes, it is no longer so.[12,13,14,15] Each of the thresholds derived in the previous sections for Zn_2Y have minima for small k , and small θ or $\theta \approx 0$-- since instabilities occurred at frequencies near the bottom of the spin wave manifold (see Fig. 2.2a). For such spin waves, splitting processes of relaxation are not possible. Confluence processes, however, are possible but not likely because $k \approx 0$. It is therefore to be expected that the linewidth of $\theta \approx 0$ spin waves in single crystal YIG will be proportional to frequency, even at low frequencies. The spin wave linewidth of Zn_2Y at 1.32 kMc is not known, but on the basis of a superficial comparison with YIG , it might be expected that the spin wave linewidth of Zn_2Y for $\theta \approx 0$ is also proportional to frequency at low frequencies. If this is true, then the spin wave Q of (2.68) will be a constant independent of frequency.

Before the Q can be determined it is necessary to obtain some estimate for the spin wave linewidth of Zn_2Y . Dixon, et al.[16] measured a spin wave linewidth of $\Delta H_k = 1.24$ Oe (for $\theta = \pi/2$, $\phi = 0$ spin waves) in a parallel pump experiment performed at 17.2 kMc for single crystal samples of Zn_2Y with substituted manganese. They obtained a ferrimagnetic resonance linewidth of 3.8 Oe at 9 kMc for the minimum linewidth case. The ferrimagnetic resonance linewidth of the single crystal Zn_2Y sample used in the experiments of Chapter VI was about 35 Oe at 6.5 kMc. Schlömann, et al.,[17] found for YIG that the ratio of the resonance to the spin wave linewidths remains constant. Assuming this relationship holds for Zn_2Y and that ΔH_k is proportional to frequency, the spin wave linewidth at 1.32 kMc is estimated to be

$$\Delta H_k = 2.44 \text{ Oe} \quad . \tag{2.69}$$

Assuming as an approximation that the spin wave linewidth is independent of Θ, then (2.69) may be assumed for all spin waves. The spin wave Q may now be calculated from (2.68), with the following result:

$$Q = 193 \quad , \tag{2.70}$$

independent of frequency, and propagation direction. It is also assumed that Q is independent of k.

4. Calculation of Thresholds

From the ferrite properties given by Appendix A and the spin wave Q given by (2.70), the spin wave thresholds may now be calculated. The actual parameter values employed are

$$p = 3.22$$

$$q = 0.0898 \quad ,$$

and

$$N_{||} = 0.099$$

is the demagnetizing factor in the plane of the ferrite disk used in the experiments reported in Chapter VI.

Figure 2.3 shows curves of the spin wave thresholds through fourth order derived in this chapter. Thresholds for both the on-resonance $(\omega_k = \omega)$ and off-resonance $(\omega_k > \omega)$ cases are shown. The even order resonant thresholds are nearly constant over the permissible range of x,

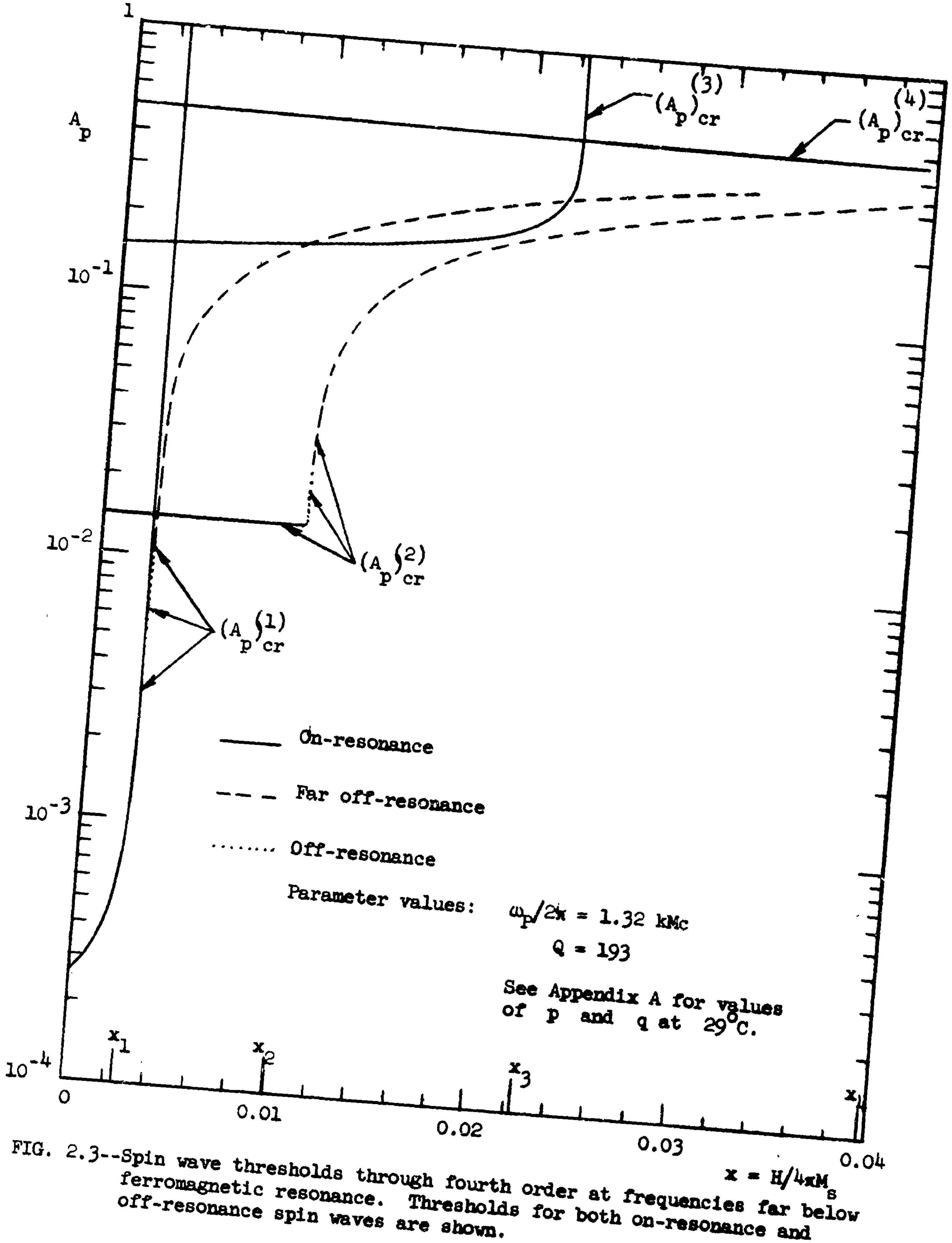

FIG. 2.3--Spin wave thresholds through fourth order at frequencies far below ferromagnetic resonance. Thresholds for both on-resonance and off-resonance spin waves are shown.

and it has been shown that the unstable spin waves propagate along the direction of the dc magnetic field $(\Theta_1 = 0)$ over this range of x. The odd order resonant thresholds vary significantly with x due to the dependence of each threshold upon Θ. At the bottom of the spin wave manifold, the value of Θ is zero and the value of x is a maximum [see (2.46)]. At $x = 0$, Θ is a maximum--with $\Theta_{max} = 0.05$ for $n = 1$ and $\Theta_{max} = 0.15$ for $n = 3$. All of the resonant thresholds show discontinuities at the maximum values of x corresponding to unstable waves at the edge of the spin wave manifold. Hence, for each order n, the spin wave instability of order n is no longer allowed on resonance above a maximum value of x [determined by (2.46)].

For both the even and odd order instabilities, the off-resonance thresholds exist of x greater than these maximum values. However, for values for x slightly less than the critical value x_n, the off-resonance threshold dominates the on-resonance threshold. The reason for this is that the odd order on-resonance thresholds become infinite at the value of x corresponding to the edge of the spin wave manifold, and the finite off-resonance threshold takes over before this point is reached in each case. This behavior is shown in Fig. 2.3 for the first order threshold. The second order off-resonance threshold is also shown in the figure. The third and fourth order off-resonance thresholds are similar in shape to the plots of the first and second order thresholds, but have not been shown because they are considerably higher.

The spin wave thresholds calculated for each order n above, were determined on the assumption that the instability for a given order n was the dominant one. However, it is clear from Fig. 2.3 that the instability with the lowest threshold, regardless of its order, will dominate the rest. Thus for the spin wave $Q \doteq 193$, the first order threshold is dominant at the lowest values of x. Where the off-resonance first order threshold intersects the second order threshold, the latter "takes over." The third and fourth order thresholds are never reached, since the second order off-resonance threshold dominates them even at the higher values of x. If the spin wave Q is actually larger than the estimated value of 193, then the thresholds will have a behavior similar to those shown in Fig. 2.3. This is due to the inverse dependence of the thresholds upon the n^{th} root of Q, where n is the order of the threshold. Hence for Q's larger than 193, the thresholds of lowest order will be reduced the most. If the spin wave Q is actually smaller than 193, then the lowest order thresholds will be increased the most due to the change in Q. In such a situation it is possible that the second order off-resonance threshold will intersect the third order resonance threshold and the latter will dominate for a small range of x. It is seen in Fig. 2.3 that this intersection is nearly possible with a Q of 193.

It is significant that with such a small range of x it is possible to pass through so many orders of spin wave thresholds. This is possible only because the pump frequency is so low (1.32 kMc). Another advantage of having a low pump frequency in an investigation of phonon instabilities is that spin wave thresholds are high; and it is likely that phonon thresholds will be observed. An investigation of the level of phonon thresholds is the subject of the next chapter.

G. SUMMARY

In this chapter the uniform precession and spin wave mode solutions to the equation of motion of the magnetization were obtained by assuming transverse pumping of a Zn_2Y disk with the easy plane lying in the plane of the disk. The pump frequency of the rf magnetic field is assumed to be far below ferromagnetic resonance. The motion of the magnetization in the uniform precession mode is shown to be confined almost exclusively to the easy plane. Owing to the nonlinearity of the equation of motion of the magnetization, spin wave modes are coupled to the uniform mode and thresholds of spin wave instabilities are determined up to fourth order. These spin wave instabilities occur at multiples of one-half the pump frequency. The threshold expression for each order instability is minimized separately for on-resonance and off-resonance spin waves. Assuming the relaxation frequency is the same for all spin waves, an estimate was then obtained for the spin wave Q. Having the spin wave

Q and the parameters of the ferrite disk, the optimum thresholds were then calculated as a function of the internal dc magnetic field of the ferrite. The results show that the dominant spin wave thresholds are the first and second order on- and off-resonance spin wave thresholds. The first order threshold is dominant only for very small internal dc fields. The third and fourth order thresholds are never reached for the value of Q assumed.

CHAPTER III

FIRST ORDER PHONON INSTABILITY THRESHOLDS

A. COUPLING MECHANISMS FOR PHONON INSTABILITIES

Chapter II showed that spin wave instabilities result from nonlinear coupling of the uniform mode of the magnetization to spin wave modes through the free magnetic energy of the ferrite. Similarly, nonlinear coupling of the uniform mode to elastic wave modes takes place through the magnetocrystalline energy. These elastic wave modes will then likewise experience instabilities when the uniform mode reaches a certain threshold. These elastic wave or phonon thresholds will be observed if they are lower than the spin wave thresholds. Some of the reasons why the phonon thresholds are expected to be lower than spin wave thresholds were given in Chapter I.

The magnetocrystalline energy referred to above is the free energy of the crystal which depends upon the magnetization and crystal strain. This energy is due to the dipolar and pseudo-dipolar interaction and the dependence of such interaction upon lattice distortion. Since the strain is always many orders of magnitude less than unity, the magnetocrystalline energy E_κ is given accurately by a Taylor expansion with respect to strain, as follows:

$$E_\kappa = E_a(\underset{\sim}{\alpha}) + \sum_{ij} \left. \frac{\partial E_\kappa(\underset{\sim}{\alpha})}{\partial \epsilon_{ij}} \right|_{\epsilon_{ij}=0} \epsilon_{ij} + \sum_{ijk\ell} \left. \frac{\partial^2 E_\kappa(\underset{\sim}{\alpha})}{\partial \epsilon_{ij}\, \partial \epsilon_{k\ell}} \right|_{\epsilon_{ij}=\epsilon_{k\ell}=0} \epsilon_{ij}\, \epsilon_{k\ell} + \cdots , \tag{3.1}$$

where the strains ϵ_{ij} represent distortions of the crystal with respect to the unmagnetized state and $\underset{\sim}{\alpha}$ is the normalized magnetization vector. Each of the subscripts i, j, k, ℓ, etc., takes on the coordinate values x , y , z . Since the magnetocrystalline energy must be invariant to spatial inversion of the magnetization, an expansion of the coefficients of (3.1) must contain only even powers of the magnetization direction cosines. The development of the anisotropy energy term E_a in this way leads to the anisotropy constants--independent of the crystal strains. The anisotropy energy for a hexagonal crystal was given by (2.14). The second term in (3.1) is called the magnetostrictive energy term. The coefficients of the lowest order terms in $\underset{\sim}{\alpha}$ for this term are called the magnetoelastic coupling constants. The third term in (3.1) is sometimes referred to as the intrinsic energy term, and the lowest order coefficients in the expansion of this term are called the magnetoelastic stiffness constants.[7]

Regardless of the magnetic state of the crystal, the elastic energy E_e is given by a Taylor expansion with respect to strain, as follows:

$$E_e = \frac{1}{2} \sum_{ijk\ell mn\ldots} \left(c_{ijk\ell}\, \epsilon_{ij}\, \epsilon_{k\ell} + c_{ijk\ell mn}\, \epsilon_{ij}\, \epsilon_{k\ell}\, \epsilon_{mn} + \ldots \right), \tag{3.2}$$

where $c_{ijk\ell}$ are the elastic stiffness constants and $c_{ijk\ell mn}$ are the coefficients of the lowest order anharmonic elastic energy term.

Consider now that the crystal is magnetized due to the application of a saturating dc magnetic field. This causes linear saturation magnetostriction, and the resulting equilibrium strains which will be present are determined by the relations

$$\frac{\partial}{\partial \epsilon_{ij}} (E_\kappa + E_e) = 0 \quad , \tag{3.3}$$

thereby minimizing the total strain-dependent part of the crystal energy. These equilibrium (static) strains establish an "operating point" about which dynamic strain deviations can take place due to applied dynamic stresses and elastic wave oscillations. For the following, dynamic strains and strain waves are of particular interest, since they are capable of giving rise to instabilities under certain conditions. It will be useful then to resolve each strain component into two parts:

$$\epsilon_{ij} \rightarrow \epsilon_{ij}^{(0)}(\underset{\sim}{\alpha}) + \epsilon_{ij} \quad , \tag{3.4}$$

where $\epsilon_{ij}^{(0)}(\underset{\sim}{\alpha})$ represent the static or equilibrium strains determined by (3.3), and the new ϵ_{ij} represent the dynamic strains of the magnetized crystal.

The strain given by (3.4) will now be inserted into the expression (3.1) for the magnetocrystalline energy. The anisotropy term is unaffected by the strain. A typical example of a magnetostrictive energy term would be

$$b\,\alpha_k\,\alpha_j\,(\epsilon_{ij}^{(0)}(\underset{\sim}{\alpha}) + \epsilon_{ij}) \quad , \tag{3.5}$$

where b is a magnetoelastic constant. Since the energy must still contain only even powers of α, then $\epsilon_{ij}^{(0)}(\underset{\sim}{\alpha})$ must also contain only even powers of α, besides being very small. Thus the first term of (3.5) contributes only a small higher order correction to the anisotropy term. The second term of (3.5) has the same form as the original magnetostrictive energy term. It is this term which is responsible for what is called the magnetoelastic effect. Similarly, a typical example of an intrinsic energy term would be

$$d\,\alpha_m\alpha_n\,(\epsilon_{ij}^{(0)}(\underset{\sim}{\alpha})\epsilon_{k\ell}^{(0)}(\underset{\sim}{\alpha}) + \epsilon_{ij}^{(0)}(\underset{\sim}{\alpha})\,\epsilon_{k\ell} + \epsilon_{k\ell}^{(0)}(\underset{\sim}{\alpha})\,\epsilon_{ij} + \epsilon_{ij}\,\epsilon_{k\ell}) \quad , \tag{3.6}$$

where d is the magnetoelastic stiffness constant. For the reason given above, the $\epsilon_{ij}^{(0)}(\underset{\sim}{\alpha})$ must contain only even powers of $\underset{\sim}{\alpha}$, besides being very small. Thus the first term in (3.6) contributes a small higher order correction term to the anisotropy energy. The second and third terms contribute a higher order correction to the magnetostrictive energy. The last term in (3.6) is the only one which has the form of the intrinsic energy--and this form is the same as appeared in the original energy expression (3.1). It is this last term which is responsible for what is called the <u>intrinsic effect</u>. It is apparent from (3.6) that this effect does not depend upon strain produced due to the orientation of the magnetization. From the above discussion it is therefore concluded that the magnetocrystalline energy given by (3.1) may be accurately used in its present form to express the energy of the dynamic strains.

The strain (3.4) will next be inserted into the expression (3.2) for the elastic energy. A typical example of the first term in (3.2) would be

$$c_{ijl\ell}\,(\epsilon_{ij}^{(0)}(\alpha)\,\epsilon_{k\ell}^{(0)}(\underset{\sim}{\alpha}) + \epsilon_{ij}^{(0)}(\underset{\sim}{\alpha})\,\epsilon_{k\ell} + \epsilon_{k\ell}^{(0)}(\underset{\sim}{\alpha})\,\epsilon_{ij} + \epsilon_{ij}\epsilon_{k\ell}) \ . \tag{3.7}$$

Using the previous argument regarding $\epsilon_{ij}^{(0)}(\underset{\sim}{\alpha})$, it is seen that the first term in (3.7) is a higher order correction to the anisotropy energy. The second and third terms are higher order contributions to the magnetostrictive energy. The last term in (3.7) represents the elastic energy as given in the original expression (3.2). A typical example of the anharmonic energy term in (3.2) would be

$$\begin{aligned} c_{ijklmn} \Big(& \epsilon_{ij}^{(0)}(\underset{\sim}{\alpha})\epsilon_{k\ell}^{(0)}(\underset{\sim}{\alpha})\,\epsilon_{mn}^{(0)}(\underset{\sim}{\alpha}) + \epsilon_{ij}^{(0)}(\underset{\sim}{\alpha})\,\epsilon_{k\ell}^{(0)}(\underset{\sim}{\alpha})\,\epsilon_{mn} \\ & + \epsilon_{ij}^{(0)}(\underset{\sim}{\alpha})\epsilon_{k\ell}\,\epsilon_{mn} + \epsilon_{ij}\,\epsilon_{k\ell}\,\epsilon_{mn} \Big) \ . \end{aligned} \tag{3.8}$$

The last term in (3.8), which is an anharmonic term in the dynamic strains, is neglected. The first and second terms are higher order corrections to the anisotropy and magnetostrictive energies, respectively. The third term has the same form as the dynamic intrinsic energy term in (3.6) and is responsible for what is called the <u>morphic effect</u>.

Even though the energy of the intrinsic and morphic effects have the same form, there is a possibility of distinguishing between these two effects. The energy of the morphic effect [third term in (3.8)], unlike that of the intrinsic effect, depends upon a distortion of the lattice in response to the direction of the magnetization.

Therefore, if the magnetization is changing direction with time, it is likely that the inertia of the crystal will be a factor in determining the magnitude of the morphic effect. It has been suggested that the morphic effect should probably be the most effective at tens of megacycles where crystals of a reasonable size exhibit well-defined elastic resonances.[7] Hence, at microwave frequencies, it is likely that the morphic effect will be negligible in comparison with the intrinsic effect.

From the above discussion it has been shown that the magnetocrystalline energy expression (3.1) and the elastic energy expression (3.2) may be used in their original form to express the energy contained in the dynamic strains when a saturating magnetic field is present.

From the energy expressions above it is apparent that the energy associated with the morphic and intrinsic effects is a factor of the order of the elastic strain smaller than the energy associated with the magnetoelastic effect. It is not surprising, then, that experiments in single crystal nickel show the dependence of the propagation velocity of acoustic waves to be well explained on the basis of the magnetoelastic effect alone.[18] Even for large bias fields, the intrinsic effect was negligible in comparison with the magnetoelastic effect. Therefore, the magnetoelastic effect may reasonably be assumed to be the dominant mechanism in the investigation of phonon instabilities in Zn_2Y . It will be found later from the experiments described in Chapter VI that this assumption appears to be substantiated.

Physically, the magnetoelastic effect described above causes a reactive loading and damping of the elastic waves by motion of the magnetization.[19] It is further to be shown in this chapter that, when the magnetization is pumped by the application of a sufficiently large rf magnetic field (in the presence of a dc magnetic field), these elastic waves exhibit instabilities when the uniform precession amplitude exceeds a threshold value.

B. ELASTIC AND MAGNETOELASTIC ENERGY CONTRIBUTIONS TO EQUATIONS OF MOTION

In Chapter II it was indicated why Zn_2Y may be be regarded as a uniaxial crystal to a first approximation. It has been shown from symmetry arguments that the elastic energy for a uniaxial crystal is given by[7,20]

$$E_e = \frac{1}{2} C_{zzzz} \epsilon_{zz}^2 + 2C_{\xi\eta\xi\eta}(\epsilon_{xx} + \epsilon_{yy}) + C_{\xi\xi\eta\eta} [(\epsilon_{xx} - \epsilon_{yy})^2 + 4\epsilon_{xy}^2]$$

$$+ 2C_{\xi\eta zz} \epsilon_{zz}(\epsilon_{xx} + \epsilon_{yy}) + 4C_{\xi z\eta z} (\epsilon_{xz}^2 + \epsilon_{yz}^2) \quad , \tag{3.9}$$

where the subscripts of the elastic constants refer to the transformed variables $\xi = x + iy$, $\eta = x - iy$, z .

Similarly, it has been shown that the magnetoelastic energy for a uniaxial crystal is given by[7]

$$E_m = B_1 \epsilon_{zz} \alpha_z^2 + B_2 (\epsilon_{xx} + \epsilon_{yy}) (\alpha_x^2 + \alpha_y^2)$$

$$+ B_3[(\epsilon_{xx} - \epsilon_{yy})(\alpha_x^2 - \alpha_y^2) + 4\epsilon_{xy} \alpha_x\alpha_y] + B_4 [\epsilon_{xz} \alpha_x + \epsilon_{yz} \alpha_y] \alpha_z \quad , \tag{3.10}$$

where the transformed variable subscripts have been suppressed to simplify the expression and to enable it to be written in an analogous form to (3.9).

Since the magnetoelastic energy contains both strain and direction cosines of the magnetization, it will contribute both to the equation of motion of the magnetization (2.6) as well as to the elastic equation of motion. It is through the magnetoelastic term that energy is transferred from spin waves to elastic waves.

1. Spin Wave Equations

The contribution of the magnetoelastic energy to the equations of motion (2.6), and ultimately to (2.23), is determined by inserting (3.10) into the relation (2.7) to give the effective magnetic field, and then inserting the latter into (2.6). The following results are obtained:

$$\begin{aligned}(\dot{\alpha}_x)_m = \frac{\gamma}{M_s}\,[&2B_1\alpha_y\alpha_z\epsilon_{zz} - 2B_2\alpha_y\alpha_z(\epsilon_{xx} + \epsilon_{yy}) \\ &+ 2B_3\alpha_y\alpha_z(\epsilon_{xx} - \epsilon_{yy}) - 4B_3\alpha_x\alpha_z\epsilon_{xy} \\ &+ B_4(\alpha_y^2 - \alpha_z^2)\epsilon_{yz} + B_4\alpha_x\alpha_y\epsilon_{xz}]\end{aligned} \tag{3.11a}$$

$$\begin{aligned}(\dot{\alpha}_y)_m = \frac{\gamma}{M_s}\,[&- 2B_1\alpha_x\alpha_z\epsilon_{zz} + 2B_2\alpha_x\alpha_z(\epsilon_{xx} + \epsilon_{yy}) \\ &+ 2B_3\alpha_x\alpha_z(\epsilon_{xx} - \epsilon_{yy}) + 4B_3\alpha_y\alpha_z\epsilon_{xy} \\ &- B_4(\alpha_x^2 - \alpha_z^2)\epsilon_{xz} - B_4\alpha_x\alpha_y\epsilon_{yz}]\end{aligned} \tag{3.11b}$$

$$\begin{aligned}(\dot{\alpha}_z)_m = \frac{\gamma}{M_s}\,[&4B_3\alpha_x\alpha_y(\epsilon_{yy} - \epsilon_{xx}) + 4B_3(\alpha_x^2 - \alpha_y^2)\epsilon_{xy} \\ &+ B_4\alpha_z(\alpha_x\epsilon_{yz} - \alpha_y\epsilon_{xz})] \quad .\end{aligned} \tag{3.11c}$$

2. Elastic Wave Equations

The fundamental elastic wave equation of motion is given by

$$\rho_0\,\ddot{R}_i = \sum_j \frac{1}{2}(1 + \delta_{ij})\,\frac{\partial^2 E}{\partial x_j\,\partial\epsilon_{ij}} \quad , \tag{3.12}$$

where i , $j = 1$, 2 , 3 ; R_i is the elastic displacement in the direction of the Cartesian coordinate x_i ; ρ_0 is the density; and E is the free energy of the crystal. The factor $\frac{1}{2}(1 + \delta_{ij})$ is needed because symmetrical physical strain terms in the free energy have been combined. The strains combined in this way are referred to here as <u>pseudo-physical strains</u> since the transformation properties of the physical strain tensor are still retained; no distinction is made between equivalent strain components. Each component of the strain written in tensor form is given by

$$\epsilon_{ij} = \frac{1}{2}\left(\frac{\partial R_i}{\partial x_j} + \frac{\partial R_j}{\partial x_i}\right) . \tag{3.13}$$

The only effective contributions to the free energy E in (3.12) will be due to elastic and magnetoelastic energies, since other terms of the free energy are independent of the strain. The expanded form of the elastic equations of motion are obtained by the substitution of (3.9) and (3.10) into (3.12) with the subsequent utilization of (3.13). The result is written symbolically as the sum of the elastic and magnetoelastic contributions

$$\rho_0\ddot{R}_i = (\rho_0\ddot{R}_i)_e + (\rho_0\ddot{R}_i)_m \quad , \tag{3.14a}$$

with the elastic terms given by

$$\begin{aligned}(\rho_0\ddot{R}_x)_e = {} & 2(2C_{\xi\eta\xi\eta} + C_{\xi\xi\eta\eta})\frac{\partial^2 R_x}{\partial x^2} + 2C_{\xi\xi\eta\eta}\frac{\partial^2 R_x}{\partial y^2} + 2C_{\xi z\eta z}\frac{\partial^2 R_x}{\partial z^2} \\ & + 4C_{\xi\eta\xi\eta}\frac{\partial^2 R_y}{\partial x\partial y} + 2(C_{\xi\eta zz} + C_{\xi z\eta z})\frac{\partial^2 R_z}{\partial x\partial z}\end{aligned} \tag{3.14b}$$

and

$$(\rho_0 \ddot{R}_y)_e = 2(2C_{\xi\eta\xi\eta} + C_{\xi\xi\eta\eta}) \frac{\partial^2 R_y}{\partial y^2} + 2C_{\xi\xi\eta\eta} \frac{\partial^2 R_y}{\partial x^2} + 2C_{\xi z\eta z} \frac{\partial^2 R_y}{\partial z^2}$$

$$+ 4C_{\xi\eta\xi\eta} \frac{\partial^2 R_x}{\partial y \partial x} + 2(C_{\xi\eta zz} + C_{\xi z\eta z}) \frac{\partial^2 R_z}{\partial y \partial z} \tag{3.14c}$$

$$(\rho_0 \ddot{R}_z)_e = 2(C_{\xi z\eta z} + C_{\xi\eta zz}) \left(\frac{\partial^2 R_x}{\partial x \partial z} + \frac{\partial^2 R_y}{\partial y \partial z} \right)$$

$$+ 2C_{\xi z\eta z} \left(\frac{\partial^2 R_z}{\partial x^2} + \frac{\partial^2 R_z}{\partial y^2} \right) + C_{zzzz} \frac{\partial^2 R_z}{\partial z^2} \quad , \tag{3.14d}$$

and the magnetoelastic terms by

$$(\rho_0 \ddot{R}_x)_m = \frac{\partial}{\partial x} [B_2(\alpha_x^2 + \alpha_y^2) + B_3(\alpha_x^2 - \alpha_y^2)]$$

$$+ \frac{1}{2} \frac{\partial}{\partial y} (4B_3 \alpha_x \alpha_y) + \frac{1}{2} \frac{\partial}{\partial z} (B_4 \alpha_x \alpha_z) \tag{3.14e}$$

$$(\rho_0 \ddot{R}_y)_m = \frac{\partial}{\partial y} [B_2(\alpha_x^2 + \alpha_y^2) + B_3 (\alpha_y^2 - \alpha_x^2)]$$

$$+ \frac{1}{2} \frac{\partial}{\partial x} (4B_3 \alpha_x \alpha_y) + \frac{1}{2} \frac{\partial}{\partial z} (B_4 \alpha_y \alpha_z) \tag{3.14f}$$

$$(\rho_0 \ddot{R}_z)_m = \frac{1}{2} \frac{\partial}{\partial x} (B_4 \alpha_x \alpha_z) + \frac{1}{2} \frac{\partial}{\partial y} (B_4 \alpha_y \alpha_z)$$

$$+ \frac{\partial}{\partial z} (B_1 \alpha_z^2) \quad . \tag{3.14g}$$

Since (3.14) is invariant under a transformation to any rotated axes x', y' , the magnetoelastic behavior is isotropic in the x-y plane. Outside the easy plane the behavior is anisotropic.

As in the case of the spin wave modes, the assumption of periodic boundary conditions is valid for acoustic wave propagation because $2\pi/k \ll$ sample dimensions. Hence a plane wave solution for the displacement $\underset{\sim}{R}$ of (3.8) is in order and is given by the Fourier series expansion

$$\underset{\sim}{R} = \sum_{k} \underset{\sim}{R}_k \, e^{i\underset{\sim}{k}\cdot\underset{\sim}{r}} \quad . \tag{3.15}$$

The displacement $\underset{\sim}{R}_k$ contains the time dependence of the wave, and has the form

$$\underset{\sim}{R}_k = \underset{\sim}{r}_k \, e^{i\omega t} + \underset{\sim}{r}_k' \, e^{-i\omega t} \quad . \tag{3.16}$$

which in general may be complex, where the quantity ω is the frequency of the elastic waves and the vectors $\underset{\sim}{r}_k$, $\underset{\sim}{r}_k'$ are independent of time. Since the elastic displacement $\underset{\sim}{R}$ must be real, then the elastic wave amplitudes are related by

$$\underset{\sim}{R}_{-k} = \underset{\sim}{R}_k^* \quad , \tag{3.17a}$$

and therefore

$$\underset{\sim}{r}_k' = \underset{\sim}{r}_{-k}^* \quad . \tag{3.17b}$$

In general, $\underset{\sim}{R}$ will contain pairs of oppositely directed traveling waves, with propagation vectors $\underset{\sim}{k}$ and $-\underset{\sim}{k}$. As in the spin wave case, the uniform precession will be found to couple pairs of elastic waves $\underset{\sim}{r}_k$ and $\underset{\sim}{r}_{-k}^*$, and this coupling will lead to exponential growth of pairs of elastic waves. For each pair it will be found that

$$|r_k| = |r_{-k}| \quad , \tag{3.18}$$

so that the unstable modes are standing waves.

3. Solutions to the Elastic Wave Equation

An examination of (3.14) reveals that the simplest solutions of the form of a single term in (3.15) occur when the propagation vector $\underset{\sim}{k}$ is along one of the crystal axes x , y or z . Since the magnetoelastic equations are isotropic in the x-y or easy plane, it may be arbitrarily assumed that the propagation vector $\underset{\sim}{k}$ is along the x-axis. The obvious independent solutions to (3.14) for elastic waves propagating in the x-y plane are therefore of the form

$$R_y\,(t,\,x)$$

$$R_x\,(t,\,x), \qquad (3.19a)$$

and

$$R_z\,(t,\,x) \quad .$$

For elastic waves propagating along the z-axis the obvious independent solutions to (3.14) have the form

$$R_x\,(t,\,z)$$

$$R_y\,(t,\,z) \qquad (3.19b)$$

and

$$R_z\,(t,\,z) \quad .$$

Because of the isotropy of the x,y plane the first two are equivalent, and the second solution will not be considered further. The solution to (3.14) with wave propagation outside of the easy plane and not along the z-axis is much more complicated than are the above solutions. Such waves are called quasi-longitudinal and quasi-transverse.[21] The name quasi is applied to these waves because, in general, the displacement vector $\underset{\sim}{R}_k$ is neither parallel nor normal to the propagation vector $\underset{\sim}{k}$. To avoid unnecessary complications, the simple solutions to (3.14) will first be considered and phonon instability thresholds will be calculated from these. It might be expected, due to the large anisotropy field, that parametric excitation of elastic waves propagating or polarized outside of the easy plane will be greatly suppressed. If the thresholds of such waves having the simple forms given above are, indeed, substantially higher than the thresholds of waves propagating and polarized in the easy plane, then it will be assumed that the thresholds of the quasi-longitudinal and quasi-transverse waves mentioned above are also substantially higher.

C. EQUATIONS OF MOTION IN A ROTATED COORDINATE SYSTEM

The direction of propagation of acoustic waves propagating in the easy plane will not necessarily be in the same direction as the applied dc magnetic field. Therefore it becomes necessary to consider acoustic wave propagation at an arbitrary angle with respect to the applied dc field. Hence, rotation of the x , y axes through an arbitrary constant angle ψ_0 relative to the field is required (see Fig. 3.1). Any vector component A_i in the original system is transformed to the rotated system $A_{i'}$. Thus, the transformation becomes

$$A_{x'} = A_x \cos \psi_0 + A_y \sin \psi_0$$

$$A_{y'} = - A_x \sin \psi_0 + A_y \cos \psi_0$$

$$A_{z'} = A_z \quad , \tag{3.20}$$

where A_i can stand for α_i , k_i or, in particular, any component of the right hand side of the equation of motion for the magnetization (2.6) (see Fig. 3.1). In making the transformation it is desirable to retain the identity, so to speak, of the displacement components R_i in the fixed system, so it will be possible to identify the simple modes. This will be done explicitly in the individual cases. Where there are only terms in $\underset{\sim}{\alpha}$, as in the spin wave equations of motion before the

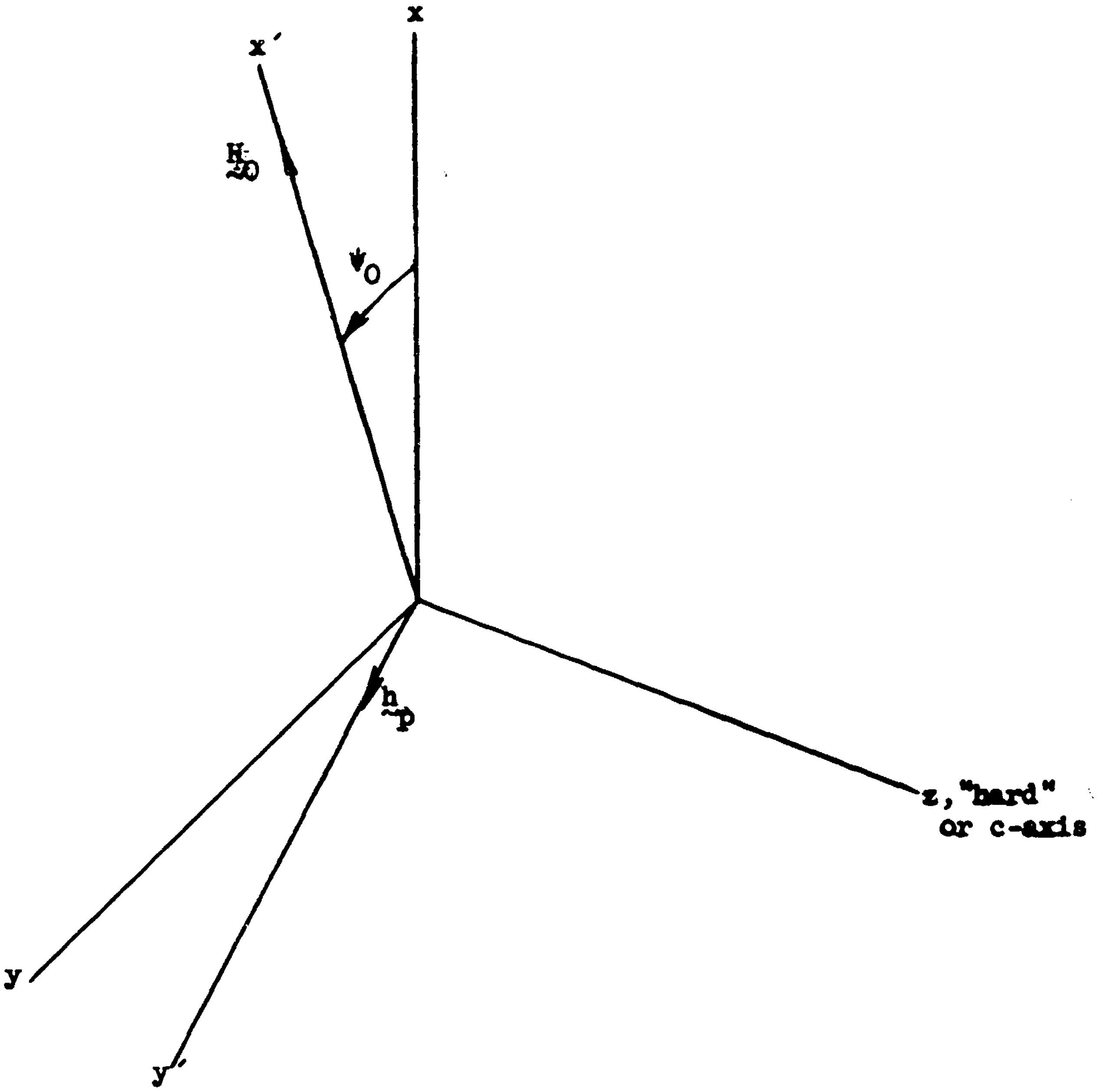

FIG. 3.1--Orientation of rotated coordinate system with respect to fixed system, showing applied magnetic fields in the rotated system.

magnetoelastic effect was considered, every term in the new system has the same form as in the old and may simply be primed. The magnetoelastic terms, containing components of $\underset{\sim}{R}$ as well as $\underset{\sim}{\alpha}$, are transformed to the rotated system by (3.20). Then $\underset{\sim}{\alpha}$ is referred to the rotated system by using the inverse of (3.20). The displacement $\underset{\sim}{R}$, on the other hand, is left in the fixed system in order to retain the identity of the elastic wave. Adding the magnetoelastic terms then yields

$$\dot{\alpha}_{ky'} = a_0'\alpha_{kz'} + a_1'\alpha_{ky'} + (\dot{\alpha}_{ky'})_m \tag{3.21a}$$

$$\dot{\alpha}_{kz'} = b_0'\alpha_{kz'} + b_1'\alpha_{ky'} + (\dot{\alpha}_{kz'})_m \quad , \tag{3.21b}$$

where the primes on the coefficients mean that uniform precession amplitudes contained therein are also primed.

D. DERIVATION OF FIRST ORDER THRESHOLDS

Only the first order pumping of phonon instabilities will be of interest, since the first order thresholds are lowest. Taking only first order terms in $\alpha_{0y'}$ and neglecting $\alpha_{z'} \ll \alpha_{y'}$ as before, the coefficients given in (3.21) become

$$\frac{a_0'}{\omega_M} = a_{00}'$$

$$\frac{a_1'}{\omega_M} = -\frac{b_0'}{\omega_M} = a_{10}' + a_{11}'\,\alpha_{0y'}$$

$$\frac{b_1'}{\omega_M} = b_{10}' + b_{11}'\,\alpha_{0y'} \quad , \tag{3.22}$$

where

$$a'_{00} = -\left(x + d + p + \frac{k_{z'}^2}{k^2}\right)$$

$$a'_{10} = -\frac{k_{y'}k_{z'}}{k^2}$$

$$a'_{11} = \frac{k_{z'}k_{x'}}{k^2}$$

$$b'_{10} = x + d + \frac{k_{y'}^2}{k^2}$$

$$b'_{11} = -2\,\frac{k_{x'}k_{y'}}{k^2} \quad .$$

Each type of elastic wave propagation will now be considered in the order shown in (3.19). For waves propagating in the x-y plane, it is assumed that $\underset{\sim}{k}\cdot\underset{\sim}{r} = kx$ in (3.15). The first such wave $R_y(t,x)$ is for a wave polarized, or having particle displacement, in the x-y or easy plane. This case will be treated in detail and will serve as a basis for the other cases. The relevant components of (3.11), which contain only terms in ϵ_{xy}, become

$$(\dot{\alpha}_x)_m = -\frac{4B_3\,\gamma}{M_s}\,\alpha_x\,\alpha_z\,\epsilon_{xy}$$

$$(\dot{\alpha}_y)_m = \frac{4B_3\,\gamma}{M_s}\,\alpha_y\,\alpha_z\,\epsilon_{xy}$$

$$(\dot{\alpha}_z)_m = \frac{4B_3\,\gamma}{M_s}\,(\alpha_x^2 - \alpha_y^2)\,\epsilon_{xy} \quad . \tag{3.23}$$

Here the strain is related to the elastic displacement by

$$\epsilon_{xy} = \sum_k \frac{ik}{2}\,R_{ky}\,e^{ikx} \quad , \tag{3.24}$$

which follows from (3.13) and (3.15). Each component $(\dot{\alpha}_i)_m$ of (3.23) must be transformed into the rotated coordinate system in accordance with (3.20), and each direction cosine α_i must be transformed by the inverse of (3.20). Since it is desired to retain the identity of the elastic mode, the components of the displacement $\underset{\sim}{R}$ are referred to the fixed coordinate system. Recalling from (2.8) that each direction cosine α_i (and hence $\alpha_{i'}$) has uniform precession and spin wave components, and retaining the spatially-dependent terms, $\underset{\sim}{\alpha}_k$, only to first order gives

$$(\dot{\alpha}_{kx'})_m = (\dot{\alpha}_{ky'})_m = 0$$

$$(\dot{\alpha}_{kz'})_m = \frac{2i\gamma B_2}{M_s} (\cos 2\psi_0 - 2\alpha_{0y'} \sin 2\psi_0)\, k\, R_{ky}\, e^{ikx} \,. \qquad (3.25)$$

Substitution of (3.25) into (3.21) and elimination of $\alpha_{kz'}$ yields the following equation:

$$(\ddot{\alpha}_{ky'} + \omega_m^2\, \alpha_{ky'} = K_{mp}\, R_{ky} \quad , \qquad (3.26a)$$

where

$$\omega_m^2 = \omega_M^2\, (x' + p)\, (x' + \sin^2 \psi_0 + \sin 2\, \psi_0\, \alpha_{0y'}) \qquad (3.26b)$$

$$K_{mp} = - \frac{2i\gamma k B_2 \omega_M}{M_s} (x' + p)\, (\cos 2\psi_0 - 2 \sin 2\psi_0\, \alpha_{0y'}) \quad . \qquad (3.26c)$$

The frequency ω_m is simply the resonant spin wave frequency [see also (2.44)], and K_{mp} is the coupling coefficient between the spin waves and the elastic waves arising from the magnetoelastic coupling. It has been assumed in deriving (3.26) that the magnitude and direction of the propagation vector $\underset{\sim}{k}$ is the same for elastic waves as for spin waves. This is reasonable since maximum mutual coupling between the spin and elastic waves requires the magnitude and direction of $\underset{\sim}{k}$ to be the same.

The elastic wave equation for the case under consideration is the one for which $i = y$ in (3.12). Utilizing the transformation (3.13) for the direction cosines and retaining spatially dependent terms only to first order, the magnetoelastic contribution (3.14f) becomes

$$(\rho_0 \ddot{R}_y)_m = 2iB_3 \left(\cos 2\psi_0 - 2\alpha_{0y'} \sin 2\psi_0\right) \sum_k k\, \alpha_{ky'}\, e^{ikx} . \quad (3.27)$$

Adding (3.27) to the strictly elastic term (3.14c) gives the equation

$$\ddot{R}_{ky} + \omega_p^2 R_{ky} = K_{pm}\, \alpha_{ky'} \quad , \qquad (3.28a)$$

where

$$\omega_p^2 = \frac{2C_{\xi\xi\eta\eta}\, k^2}{\rho_0} \qquad (3.28b)$$

$$K_{pm} = \frac{2ik\, B_3}{\rho_0} \left(\cos 2\psi_0 - 2\alpha_{0y'} \sin 2\psi_0\right) \quad , \qquad (3.28c)$$

where again the spin wave and phonon k's must be equal.

The equations of motion for the combined magnetic-elastic system are (3.26) and (3.28). Losses are introduced phenomenologically into these equations, with the result

$$\ddot{\alpha}_{ky'} + 2\eta_m \dot{\alpha}_{ky'} + \omega_m^2 \alpha_{ky'} = K_{mp} R_{ky} \qquad (3.29a)$$

$$\ddot{R}_{ky} + 2\eta_p \dot{R}_{ky} + \omega_p^2 R_{ky} = K_{pm}\, \alpha_{ky'} \quad , \qquad (3.29b)$$

where the relaxation frequencies $\eta_m = \omega_m/2Q$, $\eta_p = \omega_p/2Q_p$ are defined in terms of the respective resonance frequencies and Q factors.

A physical interpretation of (3.29) is found by assuming zero pumping field (i.e., $\alpha_{0y} \to 0$). First insert (2.9) primed and (3.16) into (3.29). A nontrivial solution exists only when the secular determinant is set equal to zero. If the frequency is assumed to be complex,

$$\omega \rightarrow \omega + i\eta \quad , \tag{3.30}$$

the solution may be expressed as

$$(\omega_p^2 - \omega^2)(\omega_m^2 - \omega^2) = K_{pm} K_{mp} \tag{3.31a}$$

$$\eta = \frac{\eta_p(\omega_m^2 - \omega^2) + \eta_m(\omega_p^2 - \omega^2)}{\omega_m^2 + \omega_p^2 - 2\omega^2} \quad , \tag{3.31b}$$

where it has been assumed that $\eta \ll \omega$. Note the symmetry of the solutions with respect to ω_m, ω_p. If the roots of (3.31a) are plotted as a function of k, as in Fig. 3.2, the usual dispersion curve is obtained. The interaction is greatest at the cross-over frequency, where $\omega_p = \omega_m$. In the system considered here, however, it will be required that $\omega \ll \omega_m$. Under these conditions, (3.31) can be approximated as

$$\omega_{p0}^2 = \omega_p^2 - \frac{K_{mp} K_{pm}}{\omega_m^2} \tag{3.32a}$$

$$\eta = \eta_p + \eta_m \frac{K_{mp} K_{pm}}{\omega_m^4} \quad . \tag{3.32b}$$

This applies to the lower part of the lower branch in Fig. 3.2, where the mode is substantially an elastic wave. The phonon-like nature of the resonance (3.32a) is denoted by the subscript p on ω_{p0}. Equation (3.32a) indicates the dependence of the phonon frequency ω_{p0} upon the

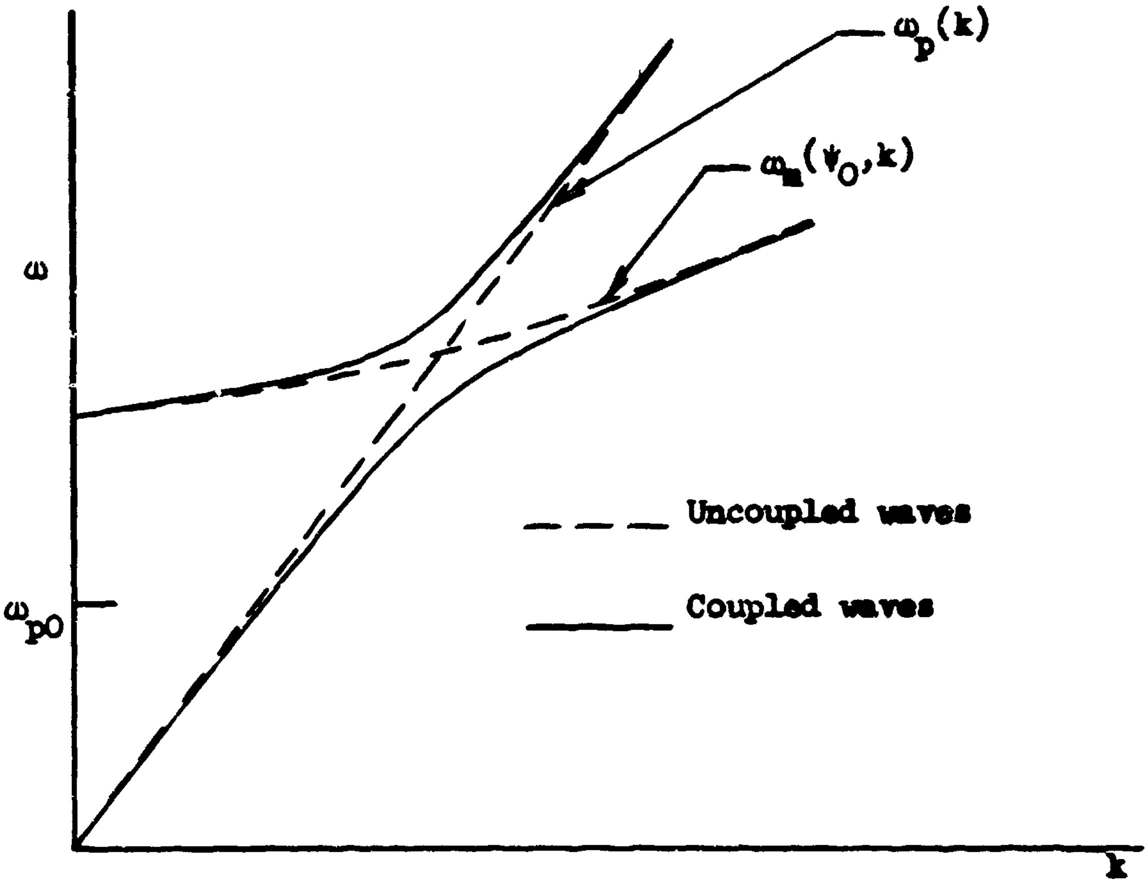

FIG. 3.2--Dispersion curve showing effect of elastic and spin wave mode coupling at constant ψ_0 .

spin wave frequency ω_m , as well as upon the spin wave-phonon coupling parameters K_{mp} , K_{pm} . For typical values of the parameters it is found that $K_{pm} K_{mp} \ll \omega_p^2$. Then, since $\omega_m^2 \gg \omega_p^2$, the frequency ω_{p0} is nearly equal to the unperturbed phonon frequency ω_p . Also, the relaxation frequency η is nearly equal to the phonon value η_p , and is relatively insensitive to the value of ω_m .

Equation (3.31), and hence (3.32), were derived under the assumption of zero pumping field (i.e., $\alpha_{0y'} = 0$) . In determining the phonon instability threshold, the modulation of ω_m and η through the time-varying quantity $\alpha_{0y'}$ must be considered. The threshold is determined most simply by obtaining the differential equation for R_{ky} alone. First, writing (3.29a) in operator form results in

$$(D^2 + 2\eta_m D + \omega_m^2)\, \alpha_{ky'} = K_{mp} R_{ky} \quad , \tag{3.33}$$

where D symbolizes the partial time derivative operator. Assuming operation far below the spin wave manifold, the first term in (3.33) may be neglected by comparison with ω_m^2 , and $\alpha_{ky'}$ may be expressed as

$$\alpha_{ky'} = \frac{K_{mp}}{\omega_m^2} \left(1 + \frac{2\eta_m}{\omega_m^2} D \right)^{-1} R_{ky} \quad . \tag{3.34}$$

Expanding the operator expression and taking only the first two terms (assuming $2\eta_m/\omega_m^2 = 1/\omega_m Q_m \ll 1$) , and substituting (3.34) into (3.29) gives the result

$$\ddot{R}_{ky} + 2\eta\, \dot{R}_{ky} + \omega_p'^2 R_{ky} = 0 \quad , \tag{3.35}$$

where R_k has the form (3.16) and the values of η and ω_p' are of the same form as (3.32) for the case $\alpha_{0y'} = 0$. However, in the derivation of (3.35) ω_m , K_{mp} and K_{pm} are functions of the pump or uniform precession amplitude $\alpha_{0y'}$.

It follows that the phonon frequency will be modulated at the pump frequency, and to first order in $\alpha_{0y'}$ will give

$$\omega_p'^2 = \omega_{p0}^2 (1 + G\,\alpha_{0y'}) \quad , \tag{3.36}$$

where from (2.29), $\alpha_{0y'} = A_p \cos \omega_p t$ to the first approximation. The modulation parameter G is given by

$$G = \frac{1}{\omega_{p0}^2} \frac{\partial \omega_{p0}^2}{\partial \alpha_{0y'}} = \frac{1}{\omega_{p0}^2} \left[\frac{K_{mp} K_{pm}}{\omega_m^4} \frac{\partial \omega_m^2}{\partial \alpha'_{0y}} - \frac{1}{\omega_m^2} \frac{\partial (K_{pm} K_{mp})}{\partial \alpha_{0y'}} \right] . \tag{3.37}$$

The damping parameter η will also be modulated by the pump amplitude $\alpha_{0y'}$ through the dependence of η upon ω_m and the coupling coefficients. However, η is nearly equal to the phonon damping parameter η_p , as was previously discussed, and if the phonon Q_p is fairly large, then $\eta_p \ll \omega_{p0}$. Therefore, the effect of modulation of the damping parameter η upon the instability threshold will be negligible, as can be seen by comparing the contributions of the second and third terms in (3.35) in the following procedure.

Substituting (3.16) into (3.35), and assuming the frequency condition

$$\omega = \omega_p/2 \tag{3.38}$$

for a first order instability yields the equation

$$\left(- \omega^2 + \frac{i\omega\omega_p}{Q_p} + \omega_{p0}^2 \right) r_{ky} + \frac{GA_p}{2} \omega_{p0}^2 r^*_{-ky} = 0 \tag{3.39}$$

and its adjoint (complex conjugate with k → -k) , where nonresonant frequency terms have been neglected.(1) Since a nontrivial solution to

---

(1) Chapter IV gives a more complete treatment of the solution to (3.35), including operation above threshold where the solution is unstable.

(3.38) exists only when the secular determinant is equated to zero, then the minimum pumping threshold becomes

$$(A_p)_{cr} = \min \frac{2}{G\omega_{p0}^2} \left[(-\omega^2 + \omega_{p0}^2)^2 + \left(\frac{\omega\, \omega_p}{Q_p} \right)^2 \right]^{1/2} . \qquad (3.40)$$

It is apparent from (3.40) that the minimum threshold will obtain when the resonance condition

$$\omega_{p0} = \omega \qquad (3.41)$$

is satisfied. Since the second term in (3.32a) is small, ω_{p0} is given approximately by ω_p of (3.28). The minimum phonon threshold on resonance then becomes

$$(A_p)_{cr} = \min \frac{2}{GQ_p} , \qquad (3.42)$$

subject, of course, to (3.38) and (3.41). Conditions (3.38) and (3.41) determine the value of the optimum propagation constant k at which the minimum threshold occurs. The threshold (3.42) must then be further minimized relative to the angle ψ_0, which appears as a variable in the modulation parameter G. For the spin wave threshold calculations, a similar condition to (3.41) included a dependence upon the direction of propagation of the waves, and the value of k was not specified by the frequency condition alone. However, in the phonon case k is determined by (3.41). As a result, the normalized exchange parameter d is a constant.

Returning to the special case R_y (t,x) by inserting parameters given in (3.26) and (3.28) into (3.37) and finally into (3.42), the threshold of instability is found to be

$$(A_p)_{yx} = \frac{(4\pi M_s)^2\, C_{\xi\xi\eta\eta}(x' + \sin^2 \psi_0)}{2\pi\, Q_p\, B_3^2 \sin 4\psi_0 \left(4 + \dfrac{\cos 2\psi_0}{x' + \sin^2 \psi_0}\right)} \; . \tag{3.43}$$

The coordinate subscripts of A_p here, as well as hereafter, refer to the direction of polarization and propagation, respectively, of the unstable elastic waves. It is noteworthy that the second term in the denominator of (3.43) is the most significant in lowering the threshold, because x' is much less than unity and the angle ψ_0 is of the order of several degrees (to be shown in the next section)--also very small. This term comes from the modulation of the spin wave mode frequency ω_m of (3.26), as can be shown from (3.37). The first term in the denominator of (3.43) is not completely ignorable, however, and comes from modulation of the coupling between the spin wave and acoustic wave modes.

The procedure for determining the pumping threshold A_p for the remaining types of elastic waves in (3.19) is basically the same as described above for the $R_y(t,x)$ case. The frequency of the spin wave mode ω_m is the same for all cases and is given by (3.26b). The velocity of propagation (ω_p/k) of the elastic wave, however, depends upon the mode and direction of propagation. The magnetoelastic coupling parameters K_{mp} , K_{pm} also depend upon the mode and direction of propagation of the elastic wave, and hence are different for each case considered.

The pump threshold angle for longitudinal waves $R_x(t,x)$ propagating in the x-y plane is

$$(A_p)_{xx} = \frac{(4\pi M_s)^2\, (2C_{\xi\eta\xi\eta} + C_{\xi\xi\eta\eta})(x' + \sin^2 \psi_0)}{2\pi\, Q_p\, B_3^2 \sin 4\, \psi_0 \left(4 \cdot \dfrac{\sin^2 2\psi_0}{(x' + \sin^2 \psi_0) \cos 2\psi_0}\right)} \; . \tag{3.44}$$

In this case, modulation of the spin wave mode frequency has less effect than does the coupling parameter modulation. The reason is that the magnitude of the magnetoelastic coupling is weaker (for small angles) for longitudinal elastic waves than it is for transverse elastic waves. It will be found that for the first two cases the lowest threshold occurs for elastic waves propagating nearly along the applied dc magnetic field (i.e., ψ_0 will be small).

The remaining case for waves propagating in the easy plane is $R_z(t,x)$, which represents a transverse wave polarized (i.e., with particle displacement) in the z-direction. The result for the pump threshold angle is

$$(A_p)_{zx} = \frac{4C_{\xi z\eta z}\,(4\pi M_s)^2\,(x' + p)}{\pi\, Q_p\, B_4^2 \sin 2\psi_C} \,. \tag{3.45}$$

Here, the weak magnetoelastic coupling as well as the influence of the anisotropy "magnetic" field greatly increases the threshold. There is only one term in the denominator of (3.43), because the modulation effects of the coupling parameters K_{mp}, K_{pm} and the spin wave frequency ω_m upon ω_{p0} of (3.32a) combine algebraically into a single term.

Now consider the two cases of elastic waves propagating along the c- or z-axis. First take $R_x(t,z)$, which is a transverse wave polarized in the easy plane. The threshold pumping angle is given by

$$(A_p)_{xz} = \frac{4C_{\xi z\eta z}\,(4\pi M_s)^2\,(1 + x' + p)}{\pi\, Q_p\, B_4^2 \sin 2\psi_0} \,. \tag{3.46}$$

This result is slightly larger than (3.43) due to the dependence of the spin wave frequency upon direction of propagation. For propagation of spin waves normal to the applied dc magnetic field, the induced dipolar demagnetizing field is maximum--and hence the spin wave frequency is maximum and constant. Therefore, there is only one term in the denominator of (3.44) because only the coupling parameters contribute to the modulation of ω_{p0} . For the thresholds $(A_p)_{yx}$ and $(A_p)_{xx}$, however, the modulation of ω_{p0} was due to variations in ω_m as well as in the coupling parameters.

The last case is for $R_z(t,z)$, a longitudinal elastic wave propagating along the c-axis. The threshold angle for this case is

$$(A_p)_{zz} \approx \infty \quad . \tag{3.47}$$

Actually this result obtains only insofar as α_{0z} is neglected in comparison with unity--a condition well satisfied, since $\alpha_{0z} \ll \alpha_{0y}$ due to the inherent ellipticity of the uniform precession mode. Elastic waves of this type cannot be pumped unless there is some deviation of the uniform motion of the magnetization permitted in the direction of the particle displacement. And of course if such deviation is neglected, then the threshold becomes infinite.

E. OPTIMIZATION AND CALCULATION OF PHONON INSTABILITY THRESHOLDS

1. Minimization of Thresholds

Each pump threshold angle given by relations (3.41) through (3.44) for the various cases is a function of ψ_0 , the angle between the x-axis and the applied dc magnetic field. To determine the minimum threshold angle it is necessary to optimize the pumping threshold A_p with respect to ψ_0 , subject to the condition (3.41) which determines the value of k (and hence d). The optimum propagation angle $(\psi_0)_{opt}$ is found for each kind of instability, and the corresponding optimum threshold angles $(A_p)_{cr}$ are evaluated. By direct comparison, the mode having the lowest threshold is then found.

Starting with the simplest case, $R_z(t,x)$, it is apparent from inspection that $(\psi_0)_{opt} = \pi/4$, and that the minimum pumping threshold angle is therefore

$$\left(A_p\right)_{\substack{zx\\cr}} = \frac{4C_{\xi z\eta z}\,(4\pi M_s)^2\,(x' + p)}{\pi\, Q_p\, B_4^2} \quad . \tag{3.48}$$

The minimum threshold for the case $R_x(t,z)$ has a similar form and is given by

$$(A_p)_{\substack{xz\\cr}} = \frac{4C_{\xi z \eta z} (4\pi M_s)^2 (1 + x' + p)}{\pi Q_p B_4^2} \quad . \tag{3.49}$$

Optimization for the $R_x(t,x)$ and $R_y(t,x)$ cases is not quite so obvious, but the optimum angle may be obtained by following the procedure given in the first paragraph of this section. A rough plot of (3.41) and (3.42) as a function of ψ_0 reveals that this optimum occurs for small angles. Using the small angle approximations for the trigonometric functions in (3.43) and (3.44), differentiation shows the optimum angle to be given to first order by

$$(\psi_0)_{opt} \approx \left(\frac{x'}{3}\right)^{1/2} \quad , \tag{3.50}$$

where it has been assumed that $x' \ll 1$. Inserting (3.50) into the small angle ($\psi_0 \ll 1$) approximations to (3.43) and (3.44) yields the following minimum pump thresholds:

$$(A_p)_{\substack{xx\\cr}} = \frac{(C_{\xi\xi\eta\eta} + 2C_{\xi\eta\xi\eta})(4\pi M_s)^2}{6\sqrt{3}\pi Q_p B_3^2} x'^{1/2} \tag{3.51}$$

$$(A_p)_{\substack{yx\\cr}} = \frac{2C_{\xi\xi\eta\eta}(4\pi M_s)^2 x'^{3/2}}{3\sqrt{3}\pi Q_p B_3^2 (1 + 4.67 x')} \quad . \tag{3.52}$$

Note that these two minimum thresholds are the only ones which depend significantly upon the parameter x' .

2. Comparison of Different Phonon Thresholds

A comparison of the above phonon thresholds will now be made. Knowing $p = 3.24$ for Zn_2Y, and $x' \ll 1$, it is apparent from (3.48) and (3.49) that $(A_p)_{zx_{cr}} < (A_p)_{xz_{cr}}$. Assuming the factor C/Q_pB^2 is approximately the same for each threshold, and that $x' \ll 1$, the following approximate ratios between the other thresholds are obtained:

$$(A_p)_{zx_{cr}} : (A_p)_{xx_{cr}} : (A_p)_{yx_{cr}} = 24\sqrt{3}\,px'^{-1/2} : 1 : 4x'. \quad (3.53)$$

From (3.53) it is seen that the highest threshold occurs for $R_z(t,x)$ elastic waves. The lowest threshold occurs for $R_y(t,x)$, which represents transverse waves propagating and polarized in the easy plane. As was suspected initially, thresholds are substantially higher for elastic waves propagating or polarized outside of the easy plane. Hence the thresholds for the more complex quasi-transverse and quasi-longitudinal elastic waves will not be considered.

3. Calculations for the Lowest Pumping Thresholds

The magnetoelastic constant, the elastic constant, and the phonon Q of Zn_2Y are not known. However, reasonable estimates can be made.

Perhaps the best estimate can be made for the elastic constants, since they do not change so much from one material to another. The elastic energy expressed in terms of engineering strains, rather than in terms of the pseudo-physical strains employed above, is given by

$$E_e = \frac{1}{2} \sum_{i,j=1}^{6} c_{ij}\, e_i\, e_j \quad , \qquad (3.54a)$$

where the c_{ij}'s are the elastic constants, and the strains e_i

are related to the tensor strains by[22]

$$
\begin{aligned}
e_i &= \epsilon_{ii} \quad \text{for } i = 1, 2, 3 \\
e_4 &= 2\epsilon_{12} = 2\epsilon_{21} \\
e_5 &= 2\epsilon_{13} = 2\epsilon_{31} \\
e_6 &= 2\epsilon_{12} = 2\epsilon_{21} \; .
\end{aligned}
\qquad (3.54b)
$$

Expanding (3.54a), substituting the tensor strains given by (3.54b), and comparing the resulting elastic energy expression in terms of the c_{ij}'s with (3.9) gives the following relations:

$$
\begin{aligned}
C_{zzzz} &= c_{33} & C_{\xi\eta zz} &= \frac{1}{2} c_{13} \\
C_{\xi\eta\xi\eta} &= \frac{1}{8}(c_{11} + c_{12}) & C_{\xi z\eta z} &= \frac{1}{4} c_{44} \\
C_{\xi\xi\eta\eta} &= \frac{1}{4}(c_{11} - c_{12}) \; .
\end{aligned}
\qquad (3.55)
$$

The elastic constant $C_{\xi\xi\eta\eta}$ will be estimated by taking the value of $C_{11} - C_{12} = 1.37 \times 10^{12}$ erg/cm^3 for Zn, which has a slightly higher density than Zn_2Y and is in the same crystal class.[22] From (3.55) the elastic constant $C_{\xi\xi\eta\eta}$ may then be found to be

$$C_{\xi\xi\eta\eta} = 3.43 \times 10^{11} \text{ erg/cm}^3 \; . \qquad (3.56)$$

The velocity of transverse phonons propagating in the easy plane may now be found from (3.56) and (3.28b). The result is given by

$$(v_p)_{yx} = \left(\frac{2C_{\xi\xi\eta\eta}}{\rho_0}\right)^{1/2} \approx 3.55 \times 10^5 \text{ cm/sec} \; , \qquad (3.57)$$

where the x-ray density given in Appendix A has been used for ρ_0 .

The magnetoelastic constant of the diagonal strain components for cubic crystal YIG is $b_1 = 5 \times 10^6$ erg/cm^3.[23] The magnetoelastic constants for hexagonal Zn_2Y will be assumed to be the same order of magnitude as this, giving the result

$$B_3 \approx 5 \times 10^6 \text{ erg/cm}^3 \quad . \tag{3.58}$$

The acoustic Q of Zn_2Y is of the order of 10^6 at 1 Mc.[24] Assuming the acoustic Q varies inversely as the frequency, an acoustic Q at $\omega_p/2\pi = 0.66$ kMc is estimated to be

$$Q_p \approx 1500 \quad . \tag{3.59}$$

Inserting (3.59), (3.58) and (3.56) into (3.52), the following numerical expression for the lowest phonon threshold is obtained:

$$(A_p)_{yx_{cr}} = \frac{7.74 x'^{3/2}}{1 + 4.67\, x'} \quad . \tag{3.60}$$

This result is plotted in Fig. 3.3. Figure 3.3 also shows the relationship of h_{cr} to $(A_p)_{cr}$, which is the same here as in Chapter II.

Using the estimated constants above, the assumption made that $\omega_{p0} = \omega_p$ in Equation (3.41) is found to be valid for $x' \geq 0.001$. However, the theory breaks down for another reason even before this value of x' is reached. In deriving the above phonon thresholds, $\omega_p^2 \ll \omega_m^2$ was assumed. At the lower values of x', ω_m approaches the phonon frequency ω_p, and this assumption no longer holds. In particular, when $\omega_m = 3\,\omega_p$ the actual phonon threshold is about 20% lower than the value given by (3.60). At $\omega_m = 2\omega_p$ the actual threshold is about 40% lower. Below the dc magnetic field corresponding to this point it is suggested (below) that spin wave thresholds dominate the phonon threshold.

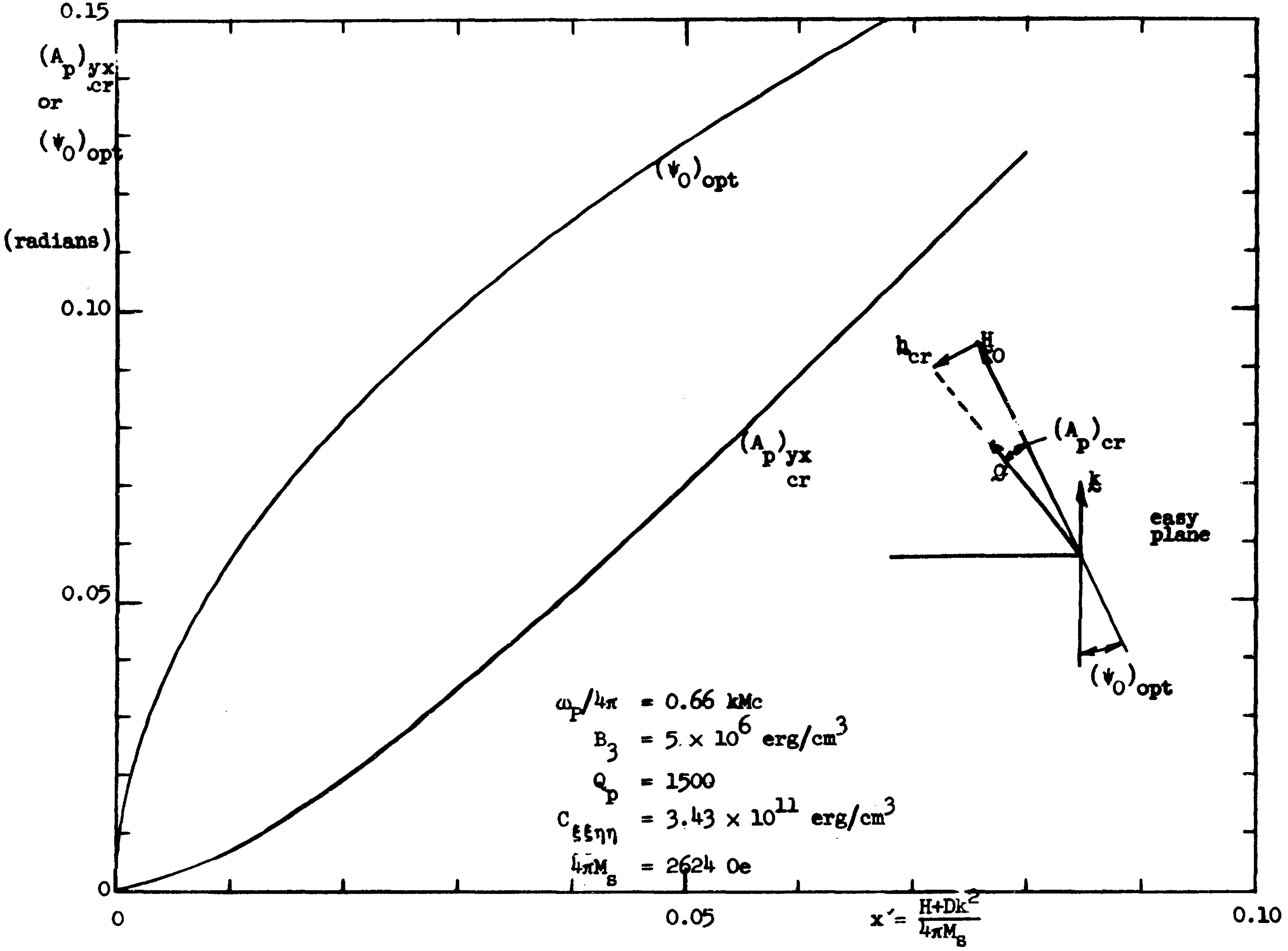

FIG. 3.3--Minimum phonon threshold and optimum phonon propagation angle as a function of normalized internal magnetic field.

F. COMPARISON OF THEORETICAL THRESHOLDS FOR PHONON AND SPIN WAVE INSTABILITIES

The minimum phonon threshold shown in Fig. 3.3 is a function of x' $[=(H + Dk^2)/4\pi M_s]$. The spin wave thresholds, however, shown in Fig. 2.3 are functions of $x(= H/4\pi M_s)$, rather than x'. Consequently, before a comparison of the phonon and spin wave thresholds can be made it is necessary to know the value of the normalized exchange parameter $d = Dk^2/4\pi M_s$ relating x and x'(by $x' = x + d$). The value of d will be found experimentally as described in Chapter VI. Assuming for the useful range of x that d is negligible (i.e., $x \approx x'$), the phonon threshold of Fig. 3.3 may then be compared directly with the spin wave thresholds of Fig. 2.3. It is seen from this comparison that the magnitude of the second order spin wave threshold is comparable with the magnitude of the phonon threshold at values of x below about x_2 , where $\omega_m = 2\omega_p = \omega_P$. On the other hand, if d is not negligible it is possible for a field region to exist where the second order spin wave threshold will dominate the phonon threshold. The reason for this is that the effect of a finite (positive) value of d is to increase the phonon threshold for a given field value x . This effect appears to have been observed, and it will be discussed in Chapter VI.

G. SUMMARY

Various mechanisms which can couple the uniform precession mode of the magnetization to elastic waves are discussed; namely, the magnetoelastic effect, the intrinsic effect, and the morphic effect. In the calculations of this chapter it is assumed that the magnetoelastic effect is the dominant mechanism in the pumping of elastic waves by the uniform precession. The spin wave equations of motion of Chapter II were modified to include contributions from the magnetoelastic energy which couples energy from the uniform precession to elastic waves.

The elastic wave equations follow from the elastic energy, together with the magnetoelastic energy expression. The simple solutions to the elastic wave equations are the ones considered in the elastic wave instability calculations.

In order to take into account propagation of elastic waves in the easy plane at an arbitrary angle with respect to the direction of the dc magnetic field, the equations of motion are expressed in terms of a rotated coordinate system. The elastic displacement components were left in the fixed coordinate system in order to maintain the identity of the simple elastic modes. For each simple mode case the elastic and spin wave equations were combined, and a Matthieu type of equation follows. For each case the first order elastic wave (or phonon) threshold was determined.

The lowest threshold was found to exist for transverse waves propagating and polarized in the easy plane of the ferrite. After making estimations of the elastic constant, the magnetoelastic constant, and the phonon Q , and knowing values for the ferrite parameters, threshold values were calculated as a function of the effective internal dc magnetic field (i.e., internal plus exchange fields). The threshold was found to increase more rapidly than linearly with increasing internal field. Assuming the exchange contribution to the effective internal field is small, a comparison of the lowest phonon threshold was made with the spin wave thresholds of Chapter II. From this comparison it was expected that the phonon threshold would dominate the spin wave thresholds at internal fields greater than that corresponding to the point where the second order off-resonance spin wave threshold begins. Below this point the phonon and spin wave thresholds were expected to be comparable.

CHAPTER IV

THEORETICAL POWER ABSORPTION BY PHONON INSTABILITIES

A. DIVISION OF POWER

Suppose microwave (rf) power P_i is incident upon an electromagnetic resonant system (dielectric resonator) which contains a ferrite. Of this incident pump power P_i a certain portion P_a is absorbed by the resonant system. This absorbed power sustains the rf magnetic field in the dielectric resonator by overcoming losses in the dielectric, the ferrite, and in the waveguide walls. For a transverse pumping experiment, the ferrite loss comprises mainly the loss associated with damping of the magnetic precession. This loss may be due to two-magnon pit scattering, rapidly-relaxing impurity or Kasuya-LeCraw confluence processes.[25]

As the rf power level is increased, additional ferrite loss will occur due to spin wave or elastic wave instabilities. In such a case a transient or irregularity can be observed on the reflected pump pulse when the absorbed power (or rf magnetic field amplitude) has reached a critical level. In Chapter II it was shown that spin wave instabilities might occur when the pump frequency is within the spin wave manifold, and phonon instabilities should occur when the pump frequency is below the spin wave manifold. This chapter is concerned with the prediction of the transient loss due to the growth of phonon instabilities.

B. GROWTH OF PHONON INSTABILITIES FROM THERMAL LEVEL

In Chapter III it was shown that elastic waves are parametrically pumped by the uniform precession mode. When the portion of the pump power going into the growing elastic waves becomes equal to the power being lost through the elastic wave damping, then the elastic wave or phonon threshold is reached. This threshold was calculated in Chapter III. It is clear that below the phonon threshold elastic wave growth will be damped out. Above the phonon threshold, however, there is a net power going into the elastic waves and the latter become unstable. Finally, at a certain level above threshold, the power going into the growing elastic waves will reach a sufficiently high level that it can be observed as a transient or irregularity in the reflected pump pulse waveform. This occurs at the critical power level referred to in Section A above.

1. Solution to the Elastic Wave Equation

It was found in Chapter III that elastic waves having the lowest threshold are transverse waves propagating and polarized in the easy plane and at a frequency of one half the pump frequency. The basic differential equation governing the motion of these elastic waves was given by (3.35). For pumping angles at or below the phonon threshold, the solution had the form given by (3.16) and (3.17b). In order to take into account the growth of unstable elastic waves above threshold, (3.16) is modified to include the exponential growth parameters as follows:

$$R_{ky} = r_{ky}\, e^{(i\omega+s)t} + r^{*}_{-ky}\, e^{(-i\omega+s)t} \quad . \tag{4.1}$$

This expression for the elastic displacement will be inserted into the elastic wave equation (3.35) to determine the growth parameters for operation above threshold; but first (3.35) will be modified to include the time dependence of the rf magnetic field amplitude.

In deriving the phonon thresholds of Chapter III it was assumed that the pump angle A_p was constant. This implies the power pulse incident upon the ferrite system had the ideal pulse characteristics of perfect flatness, zero rise and fall times, and no frequency modulation. Such an ideal pulse, sketched in Fig. 4.1a, could not be obtained in practice chiefly because the required pulse length was of the order of 100 μsec. In general, it is difficult to obtain a flat pulse of this length with existing techniques, particularly at the frequency (1.32 kMc) and power

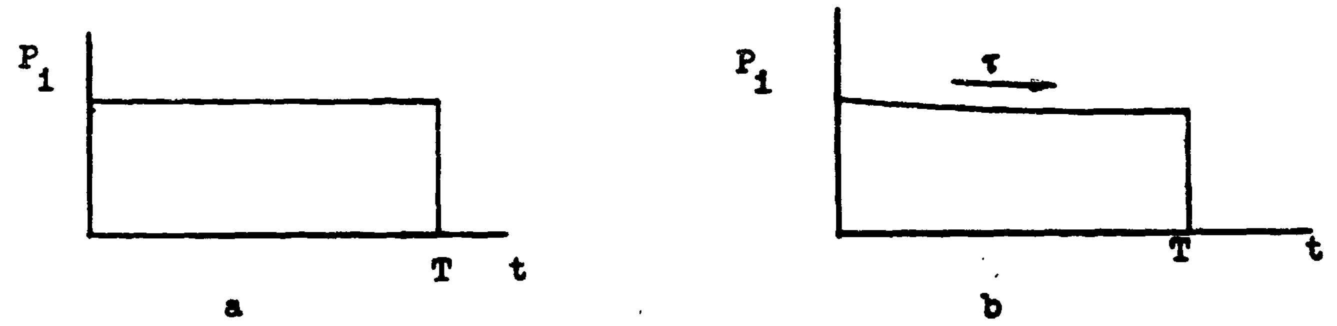

FIG. 4.1--Sketch of time dependence of the incident pump power for the ideal (a) and actual (b) pulses.

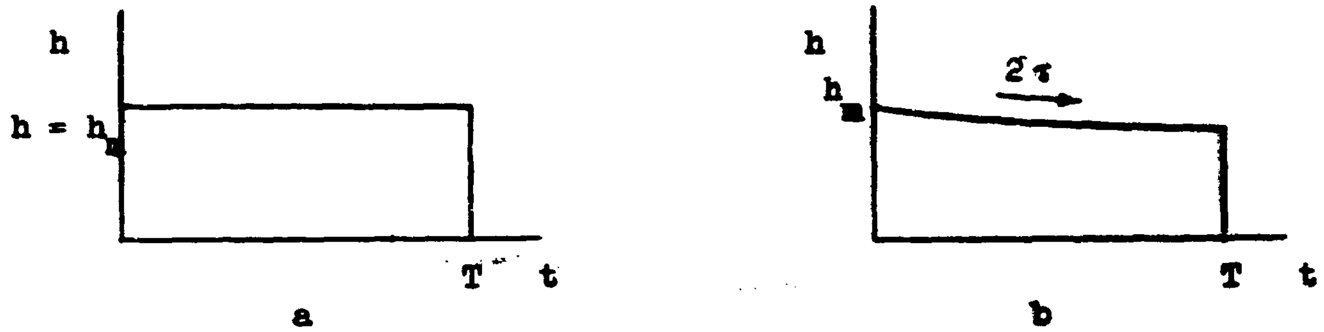

FIG. 4.2--Sketch of time dependence of the rf magnetic field amplitude for the ideal (a) and actual (b) pulse cases.

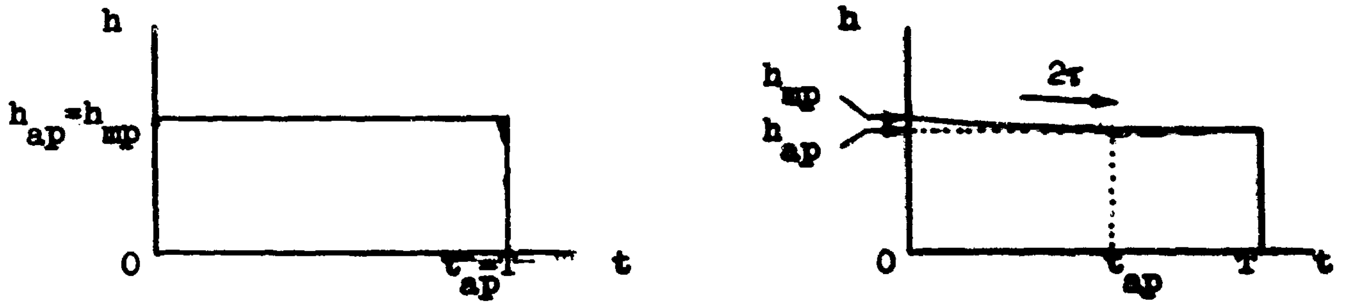

FIG. 4.3--Sketch of time dependence of the rf magnetic field amplitude when the apparent threshold is reached for the ideal (a) and actual (b) pulse cases. The apparent critical field h_{ap} and build-up time t_{ap} indicate the initial appearance of the power absorption due to growth of phonon instabilities.

level (~ 10 W peak) desired. (Refer to Chapter V for details on the technique employed to obtain the 100 μsec pulse; refer to Chapter VI for photographs of the actual power pulse waveforms used in the threshold experiments.) The incident power for the actual pulse is sketched in Fig. 4.1b in terms of the approximate representation

$$P_i = P_{im} e^{-t/\tau} , \tag{4.2}$$

where $t = 0$ specifies the time when the pulse has "settled down" to a frequency within the bandwidth of the resonant system; P_{im} is the incident power at $t = 0$; and τ is the time constant during the useful length of the pulse, which excludes the frequency modulation at the end of the pulse. Since the reflected power level P_r is related to the incident power P_i by

$$P_r = |\Gamma|^2 P_i ,$$

where Γ is the reflection coefficient, then the absorbed power P_a is given by

$$P_a = (1 - |\Gamma|^2) P_i .$$

Chapter V shows that the resonator magnetic field amplitude h is related to the absorbed power P_a as follows:

$$h \propto P_a^{1/2} .$$

Using the above relations between h, P_a, Γ and P_i, then, the time dependence of the field amplitude is found with the aid of (4.2) to be

$$h = h_m e^{-t/2\tau} , \tag{4.3}$$

where h_m is the initial maximum magnetic field amplitude corresponding to P_{im}, and Γ has been assumed to be constant during the pulse. The ideal and actual field amplitude pulse shapes reaching the ferrite sample are sketched in Figs. 4.2a,b. The actual pulse approaches the ideal pulse in flatness as the time constant 2τ becomes infinite. The actual pulse shape is considered here rather than an approximation thereto because it will be found that more information regarding the nature of the phonon absorption can be obtained theoretically from the actual pulse shape.

The pumping angle A_p was defined by (2.28b) as

$$A_p = h/H_0 \;.. \tag{4.4}$$

In Chapters II and III, where h was assumed constant, the threshold pumping angle or critical angle was given by

$$(A_p)_{cr} = h_{cr}/H_0 , \tag{4.5}$$

where h_{cr} is the critical or threshold rf field amplitude and H_0 is the dc field at the ferrite sample. In this chapter where rf field amplitudes greater than h_{cr} are considered, the threshold angle is given by

$$(A_p)_{ap} = h_{ap}/H_0 , \tag{4.6}$$

where $(A_p)_{ap}$ and h_{ap} refer to the apparent threshold angle and apparent critical field, respectively, at which the power absorption due to the growth of instabilities is sufficiently high to be seen as an irregularity in the reflected pump pulse (Fig. 4.3).

For the actual pulse the apparent critical field was determined by measuring the power level of the incident pulse at the time t_{ap} where the instability first appeared on the reflected pulse. Thus the apparent critical field for the actual pulse is given by

$$\text{(actual pulse)} \qquad h_{ap} = h_{mp}\, e^{-t_{ap}/2\tau} \quad , \tag{4.7}$$

where h_{mp} is the corresponding value of h_m. For the ideal pulse, where $\tau \to \infty$, the apparent critical field becomes

$$\text{(ideal pulse)} \qquad h_{ap} = h_{mp} \quad , \tag{4.8}$$

and the instability would first be observed at the end of the pulse, $t_{ap} = T$. The relationships between these quantities expressed in (4.8) and (4.7) for the ideal and actual pulse shapes are shown in Figs. 4.3a and b. The dashed lines indicate the irregularities due to the instability.

Inserting the time-decaying pumping angle (4.4), with h given by (4.3), into the elastic wave equation of motion (3.35) gives

$$\ddot{R}_{ky} + 2\eta\, \dot{R}_{ky} + \omega_{p0}^2 \left(1 + \frac{Gh_m}{H_0}\, e^{-t/2\tau} \cos \omega_p t \right) R_{ky} = 0 \quad . \tag{4.9}$$

A trial solution (4.1) with $s = s(t)$ is now inserted into (4.9), giving

$$\Big[2\dot{s} + t\ddot{s} + (s + t\dot{s})^2 + 2\eta(s + t\dot{s}) + \omega_{p0}^2 - \omega^2 + 2i\omega(s + t\dot{s} + \eta)\Big]\, r_{ky} + \omega_{p0}^2\, \frac{Gh_m}{2H_0}\, e^{-t/2\tau}\, r_{-ky}^* = 0 \quad , \tag{4.10}$$

and its adjoint (complex conjugate, with $k \rightarrow -k$) , where the frequency condition

$$\omega = \omega_p/2 \tag{4.11}$$

has been invoked. The secular equation for this will require that $|r_{ky}| = |r_{-ky}|$, which is the requirement for a standing wave solution as mentioned in Chapter III, especially (3.18).

For reasons to be discussed later, only resonant instabilities will be considered in calculating the power absorbed by the pump. The real part of the coefficient for r_{ky} in (4.10) is therefore assumed to be very nearly zero at all times, giving

$$2i\omega(s + t\dot{s} + \eta)r_{ky} + \omega_{p0}^2\, \frac{Gh}{2H_0}\, r_{-ky}^* = 0 \quad . \tag{4.12}$$

The secular equation of (4.12) and its adjoint in this case yields

$$t\dot{s} + s + \eta = \eta\, \frac{G(\psi_0)}{G\left((\psi_0)_{opt}\right)}\, \frac{h(t)}{h_{cr}} \quad , \tag{4.13}$$

when written in terms of the critical field h_{cr} , specified in general by (4.5) and (3.42) and written as

$$h_{cr} = 2H_0/G\left[(\psi_0)_{opt}\right] Q_p \quad , \tag{4.14}$$

where $[(\psi_\theta)_{opt}]$ is the optimum value of the modulation parameter $G(\psi_0)$, and the phonon Q_p is related to the relaxation frequency η by $\eta = \omega_{p0}/2Q_p$. If $h(t)$ is a slowly varying function of time, the RHS of (4.13) may be expanded in a Taylor series. A series solution for the exponential growth parameter s is thereby found to be

$$s(\psi_0 , t) = -\eta + \eta \frac{G(\psi_0)}{G\left((\psi_0)_{opt}\right)} \frac{h'(t)}{h_{cr}} \quad , \tag{4.15a}$$

where

$$h'(t) = h_m \sum_{n=0}^{\infty} \frac{1}{(n+1)n!} \left(\frac{-t}{2\tau}\right)^n = h_m\left(1 - \frac{t}{4\tau} + \frac{1}{24}\left(\frac{t}{\tau}\right)^2 + \cdot\cdot\cdot\right) \tag{4.15b}$$

is an effective rf field amplitude. The series converges rapidly since $t \ll 2\tau$, and only two or three terms are needed. For small t/τ , $h'(t)$ decreases with a time constant approximately one half that of $h(t)$. .

2. Power Absorbed by the Unstable Modes (Phonon Absorption)

Assuming that all of the pump energy which reaches the elastic wave system goes into pumping the unstable phonon modes, the total elastic energy may then be represented (within a constant) by the energy contained only in the unstable modes. Thus the elastic energy density for transverse accoustic waves propagating and polarized in the easy plane is found from (3.9) to be

$$E_p = 4C_{\xi\xi\eta\eta}\,\epsilon_{xy}^2 \quad , \qquad (4.16)$$

where

$$\epsilon_{xy} = \frac{1}{2}\,\frac{\partial R_y}{\partial x} \quad .$$

Utilizing the expansion

$$R_y = \sum_k R_{ky}\,e^{ikx} \quad , \qquad (4.17)$$

where

$$R_{-ky} = R_{ky}^* \quad ,$$

the time average stored energy in the sample is found for standing wave modes to be

$$\mathcal{E}_p = \int E_p\,dV = C_{\xi\xi\eta\eta}\,V\sum_k k^2\left\{|r_{ky}|^2 + |r_{-ky}|^2\right\}e^{2s_k t} \quad , \qquad (4.18)$$

where a different growth factor has been allowed for each mode, and V is the volume of the sample.

Since the unstable modes will begin growing exponentially from thermal level at $t = 0$, the average thermal energy in the modes must be found in order to evaluate the energy at later times. For microwave frequencies $\hbar\omega$ is much less than $k_B T$ (where k_B is Boltzmann's constant), classical statistics may be used. Thus the average thermal energy contained in each mode is

$$k_B T = C_{\xi\xi\eta\eta} V k^2 \left\{ |r_{ky}|^2 + |r_{-ky}|^2 \right\} \quad . \tag{4.19}$$

The total average energy (4.18) may be written

$$\mathcal{E}_p = 2 k_B T \sum_{k=0}^{\infty} e^{2 s_k t} \quad , \tag{4.20}$$

since there are two standing wave modes ($\sin kx$ and $\cos kx$) for each value of k. The energy $\mathcal{E}_p$ will be used to evaluate the power absorbed from the pump. Equation (4.20) should therefore be summed only over the modes which are growing in time.

In determining the values of k which will contribute significantly to the summation in (4.20) it is helpful to utilize the k-space concept. Figure 4.4 shows a representation of a portion of k-space for periodic boundary conditions.[26] The distance separating modes along a given coordinate direction i in k-space is

$$d_{k_i} = 2\pi / a_i \quad , \tag{4.21}$$

where a_i is the dimension of the sample in the direction i. For a ferrite disk, the mode spacing may be approximated by

$$d_{k_{||}} = 2\pi / d \tag{4.22}$$

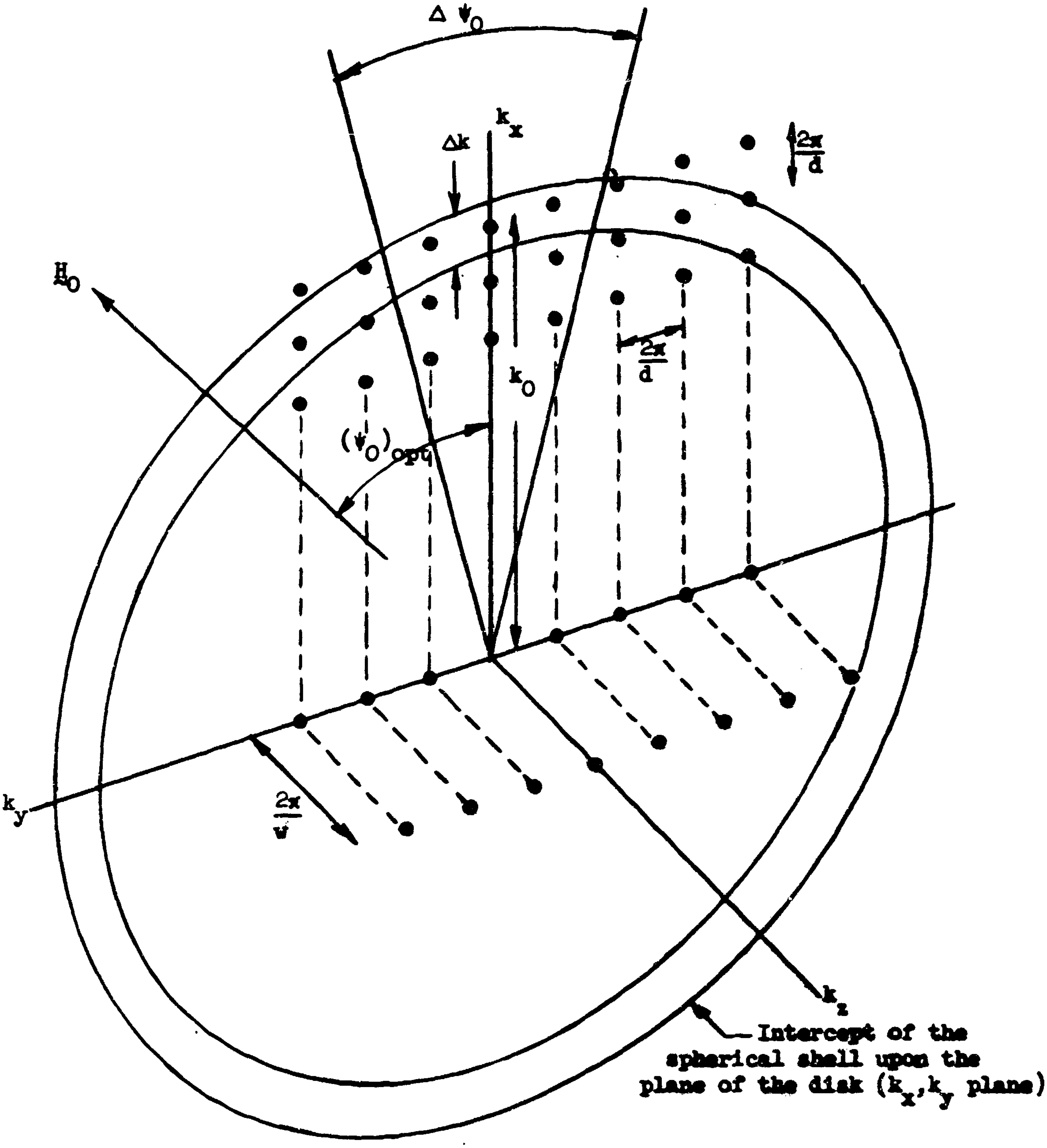

FIG. 4.4--Disposition of modes in k-space showing the range of modes contributing significantly to the pump absorption; H_0 lies in the k_x, k_y plane.

in the plane of the disk, where d is the disk diameter, and by

$$\partial_{k_\perp} = 2\pi/w \tag{4.23}$$

normal to the disk, where w is the disk thickness.

In Chapter III it was assumed that there was only one unstable mode, resonant at $\omega_p/2$. This mode is represented by a single point in k-space, the magnitude of the wave vector $\underset{\sim}{k}_0$ being determined by the frequency condition (3.41) and the orientation of $\underset{\sim}{k}_0$ by the direction of propagation relative to the dc magnetic field. In Chapter III an optimum value was found for the angle ψ_0 between $\underset{\sim}{k}$ and the dc field. For convenience, the axes in k-space will be chosen so that k_x corresponds to this optimum direction, and the k_x, k_y plane corresponds to the plane of the disk sample (see Fig. 4.4). Although the assumption of a single mode is a valid one in the determination of the phonon threshold angle or critical rf magnetic field, it is not valid for operation above threshold. The reason is that other modes will be pumped. This case will now be considered.

The first restriction on the modes which will contribute to (4.20) is that $\omega_p/2$ should be within the mode bandwidth. Otherwise they will grow only very slowly, if at all. This bandwidth is

$$\Delta\omega_p = \omega_p/Q_p \quad , \tag{4.24}$$

and from (3.28b) the corresponding "wavenumber bandwidth" is

$$\Delta k = k_0/Q_p \ll k_0 \quad . \tag{4.25}$$

This shows that the relevant modes must lie within a thin spherical shell of radius k_0 and thickness Δk in k-space (see Fig. 4.4). In order to compare the "wavenumber bandwidth" with the mode spacing, typical parameters

$$\omega_p/4\pi = 0.66 \text{ kMc}$$
$$d = 0.054 \text{ in.}$$
$$Q_p \approx 10^3 - 10^4$$

are chosen. It can then be verified that

$$\Delta k \ll d_{k_\parallel} \quad ,$$

as shown in Fig. 4.4. The radius of the shell, k_0 , is not shown to scale. Using the parameters assumed above results in

$$k_0 \approx 150 \frac{2\pi}{d} \approx (10^3 - 10^4)\, \Delta k \quad , \qquad (4.26)$$

and the thickness of the shell is very small compared with its radius.

A more significant restriction on the modes relates to the dependence of the modulation parameter G on the angle ψ_0 . This limits the contributing modes to a portion of the above mentioned spherical surface in the neighborhood of the axes k_x . Figure 4.5 shows a plot of the threshold angle $(A_p)_{yx}$ vs ψ_0 with a typical experimental value of $x' = 0.05$ and parameter values as specified by Chapter III. The angle $(\psi_0)_{opt}$ indicated was calculated from the small angle approximation (3.50). It is seen to agree closely with the actual minimum of $(A_p)_{yx}$. The threshold becomes infinite at $\psi_0 = \pi/4$. The magnitude of the threshold $|A_p|$ as a function of ψ_0 is shown in Fig. 4.6a. Due to

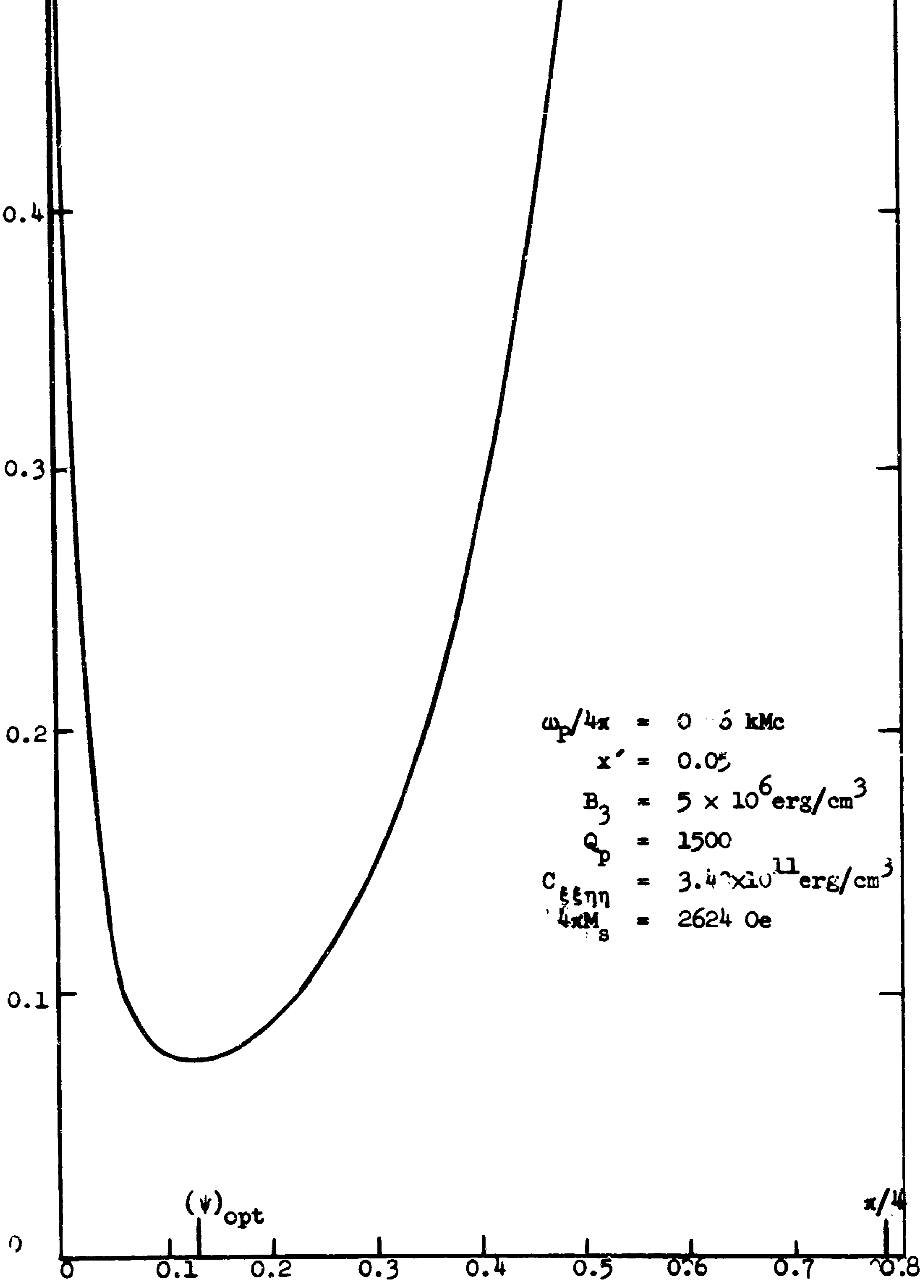

FIG. 4.5--Threshold $(A_p)_{yx}$ vs. rotation angle ψ_0 for resonant modes ($\omega = \omega_{p0} = \omega_p/2$) .

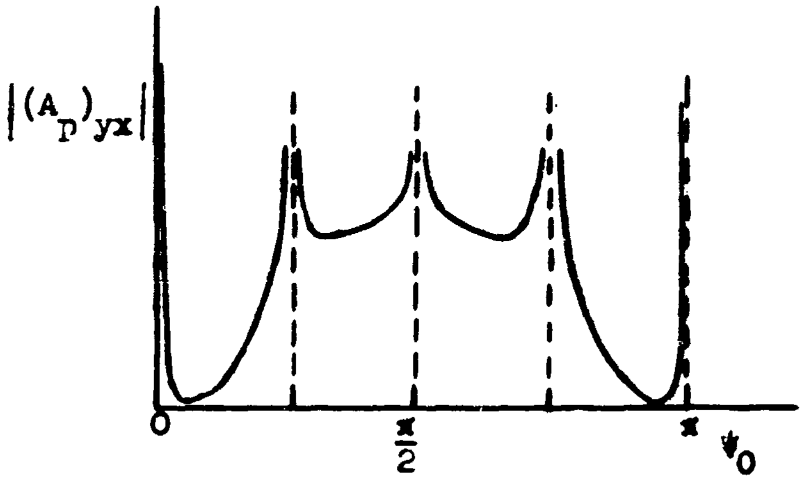

FIG. 4.6a--Sketch showing one cycle variation in the magnitude of the resonant threshold angle $|(A_p)_{yx}|$ vs rotation angle ψ_0. The function is repetitive with period π.

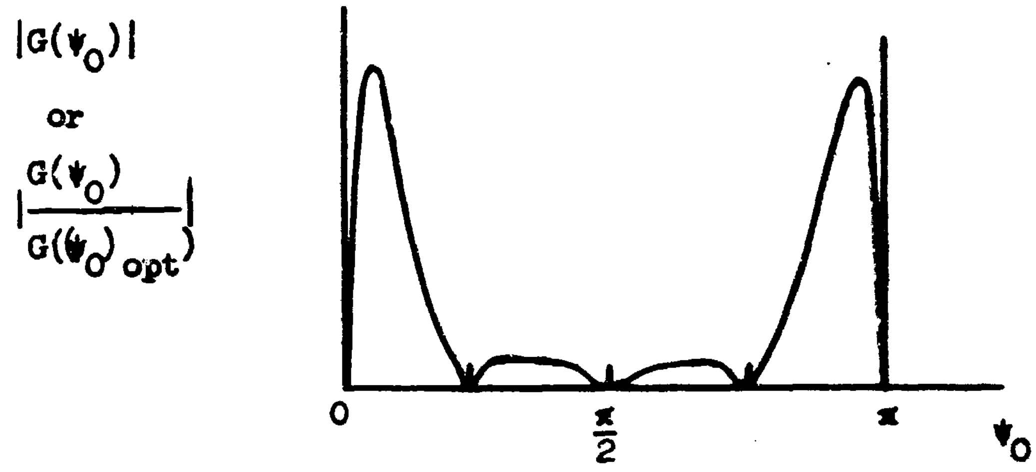

FIG. 4.6b--Sketch showing one cycle variation of the modulation parameter magnitude $|G(\psi_0)|$ corresponding to the threshold variation of Fig. 4.6a.

the inverse dependence of A_p upon $\sin 4\psi_0$, A_p has singularities at $\psi_0 = \frac{n\pi}{4}$, where n is any integer. Figure 4.6b shows the modulation parameter $G(\psi_0)$, which varies inversely with A_p, in accordance with (3.42). Note the narrow range of ψ_0 over which G is large. This means that, when the rf pump field is only slightly greater than h_{cr}, the growing modes in the k_x, k_y plane of Fig. 4.4 lie within a range of angles $\Delta\psi_0$ about $(\psi_0)_{opt}$.

The threshold angles shown in Figs. 4.5 and 4.6 apply only to transverse modes with the wave vector and polarization in the plane of the disk (k_x, k_y in Fig. 4.4). Modes lying outside the k_x, k_y plane in Fig. 4.4 should also be considered in evaluating (4.20). Furthermore, there will be two transverse and one longitudinal mode associated with each point in Fig. 4.4, and these should all be included in the summation. It was shown in Chapter III, however, that the threshold angle is very much larger when the wave vector is normal rather than parallel to the plane of the disk. On the basis of this result, and the wider spacing of the modes along the k_z axis (Fig. 4.4), Eq. (4.20) will only be summed over the k_x, k_y plane. Since it was also shown in Chapter III that the transverse wave polarized in the plane has the lowest threshold, the restriction of the summation in (4.20) to modes of this kind will be retained.

From the above considerations it is seen that the summation in (4.20) will be taken only over modes lying within the intercept of the spherical shell upon the k_x, k_y plane in Fig. 4.4. Within this region the modes are distributed with an approximately uniform angular spacing,

$$\frac{2\pi}{k_0 d} = \frac{d_{k_\parallel}}{k_0} \ll 1 \text{ radian}$$

(from 4.26); and there will be only one mode at each angular position, since Δk is much less than $2\pi/d$. The summation in (4.20) may therefore be approximated by an integral

$$\mathcal{E}_p = \frac{4k_B T\ k_0}{d_{k_\parallel}} \int_{\psi_1=(\psi_0)_{opt}-\frac{\Delta\psi_0}{2}}^{\psi_2=(\psi_0)_{opt}+\frac{\Delta\psi_0}{2}} e^{2s_k(\psi_0,k,t)t}\, d\psi_0 \quad . \tag{4.27}$$

It is not necessary to consider negative values of k_x, since two standing wave modes for each value of k have been allowed for in (4.20). In obtaining (4.27) from (4.20), a factor of 2 has been taken out of the summation to account for phonon modes which occur for k near $\psi_0 = -(\psi_0)_{opt}$ as well as near $\psi_0 = (\psi_0)_{opt}$. Figure 4.6 shows that these values of ψ_0 are the ones near which $G(\psi_0)$, and hence $s(\psi_0)$ [(4.15a)], has its maximum values.

Since all modes considered in (4.27) are close to resonance, the growth parameter for a resonant mode $s(\psi_0,k_0)$ will be used in evaluating the integral. Also, the first term of a Taylor series expansion about $(\psi_0)_{opt}$ will be used for the modulation parameter

$$G(\psi_0) = G\Big((\psi_0)_{opt}\Big) + \frac{G''\Big((\psi_0)_{opt}\Big)}{2!}\Big(\psi_0 - (\psi_0)_{opt}\Big)^2 \quad ; \tag{4.28}$$

therefore

$$\frac{G(\psi_0)}{G\Big((\psi_0)_{opt}\Big)} \approx 1 - \frac{9}{4x'}\Big(\psi_0 - (\psi_0)_{opt}\Big)^2 \tag{4.29}$$

and

$$s_{k_0}(\psi_0, k_0, t) \approx \eta\left(-1 + \frac{h'(t)}{h_{cr}}\left[1 - \frac{9}{4x'}\left(\psi_0 - (\psi_0)_{opt}\right)^2\right]\right) . \quad (4.30)$$

Using (4.27) and (4.30) gives

$$\mathcal{E}_p = \frac{4k_B T\, k_0}{d_{k_\parallel}}\, e^{2\eta t(-1+h'/h_{cr})} \int_{\psi_1}^{\psi_2} e^{\frac{-9\eta t\, h'}{2h_{cr}\, x'}\left(\psi_0 - (\psi_0)_{opt}\right)^2} d\psi_0 \quad .$$

(4.31)

For t greater than $1/\eta$ and $\psi_0 - (\psi_0)_{opt}$ of the order $(\psi_0)_{opt}$, the integrand of (4.31) becomes vanishingly small, and the integration limits may be extended to infinity without significantly affecting the value of the integral--in accordance with the usual procedure for the method of steepest descent.[27] The integral reduces to

$$I = \left(\frac{2\pi x'\, h_{cr}}{9\eta t\, h'}\right)^{1/2} \quad . \quad (4.32)$$

From (4.20), (4.31), and (4.32) the total stored energy in the growing modes is

$$\mathcal{E}_p \approx N k_B T\, e^{2\eta t(-1 + h'/h_{cr})} \quad , \quad (4.33)$$

where

$$N = \frac{4k_0 I}{d_{k_\parallel}} = \frac{2k_0 d}{3}\left(\frac{2x' h_{cr}}{\pi\eta h' t}\right)^{1/2} , \quad (t > 1/\eta) \quad , \qquad (4.34)$$

is the effective number of growing modes. Equation (4.34) shows that the effective number of growing modes decreases with time, even when the pump field amplitude h' is constant. From (4.33) the effective number of modes is defined relative to the maximum growth rate. As time increases, the modes with small growth rates become less and less significant by comparison with the rapidly growing modes, and the number of effective modes decreases. When the condition $t > 1/\eta$ is not satisfied, the method of steepest descent is not valid. Fortunately, the experimental effects are observed at times satisfying this condition.

Knowing the phonon energy as a function of time, the total power P_p going into the phonon system may be determined from

$$P_p = \frac{d\mathcal{E}_p}{dt} + 2\eta\mathcal{E}_p \quad . \qquad (4.35)$$

The first term in (4.35) represents the increase in stored energy. If the stored energy were not increasing there would still be a power loss in the phonon system. This additional power loss, represented by the second term of (4.35), is associated with the phonon Q_p . Inserting (4.33) into (4.35) yields

$$\begin{aligned} P_p &= \mathcal{E}_p\left\{\frac{d}{dt}2\eta t\left(-1+\frac{h'(t)}{h_{cr}}\right)+\frac{dN(t)/dt}{N(t)}+2\eta\right\} \\ &= 2\eta\mathcal{E}_p\left[\frac{h'}{h_{cr}}-\frac{1}{4\eta t}\right]\left[1+\frac{t}{h'}\frac{dh'}{dt}\right] \quad . \end{aligned} \qquad (4.36)$$

Since h' is a slowly varying function of time, it may be taken as a constant in (4.36) except in the exponential factor of $\mathcal{E}_p$. Assuming that t is greater than a few μsec $[(1/4\eta t) \ll 1]$, the phonon power absorption is given approximately by

$$P_p \approx 2\eta \frac{h_m}{h_{cr}} N(t) k_B T \, e^{2\eta t \left[-1 + \frac{h_m}{h_{cr}}\left(1 - \frac{t}{4\tau}\right)\right]} , \qquad (4.37a)$$

where $N(t)$ is approximately

$$N(t) \approx \frac{2k_0 d}{3} \left(\frac{2x' \, h_{cr}}{\pi\eta t \, h_m} \right)^{1/2} . \qquad (4.37b)$$

The damping parameter η is related to the phonon Q_p by

$$\eta = \omega_{p0}/2Q_p . \qquad (4.37c)$$

C. PHONON ABSORPTION IN TERMS OF MEASURABLE PARAMETERS

It is now necessary to relate the phonon absorption P_p to the transient observed in the reflected pump pulse. From simple conservation of power, the reflected power P_r is given by

$$P_r = P_i - P_a , \qquad (4.38)$$

where P_i is the incident power and P_a is the absorbed power. Given that P_i is constant, the differential relation which follows from (4.38), namely

$$\Delta P_r = -\Delta P_a \quad , \tag{4.39}$$

shows that any increase which occurs in P_a (due to phonon absorption) will be accompanied by a corresponding decrease in P_r .

The power P_a absorbed by the dielectric resonator system is given in terms of the stored energy U by the familiar expression

$$P_a = \frac{\omega_p U}{Q_0} \quad , \tag{4.40}$$

where ω_p is the pump frequency and Q_0 is the effective Q of the resonator system. Since the absorbed power is a function of the stored energy as well as of the system Q , the following differential relationship is obtained from (4.40):

$$\Delta P_a = \Delta P_{fld} + \Delta P_F \quad , \tag{4.41a}$$

where ΔP_{fld} represents the additional power loss required to sustain the increased energy of the electromagnetic field, and is given by

$$\Delta P_{fld} = \frac{\omega_p}{Q_0} \Delta U \quad . \tag{4.41b}$$

The increase in ferrite power absorption ΔP_F is given by

$$\Delta P_F = \omega_p U \Delta\left(\frac{1}{Q_0}\right) \quad . \tag{4.41c}$$

This power absorption takes place only when the Q_0 of the system is changed by introducing additional losses into the system--for instance, through growth of spin wave or elastic wave instabilities in the ferrite.

For an overcoupled resonator system, the external Q is given by

$$Q_{ext} = Q_0/r_0 \quad , \tag{4.42}$$

where r_0 is the voltage standing wave ratio (VSWR) at resonance. For a given position of the movable short, Q_{ext} is constant (see Chapter V). Therefore (4.41c) becomes

$$\Delta P_F = - P_a \frac{\Delta r_0}{r_0} \quad . \tag{4.43}$$

It is desired to obtain the ferrite absorption in terms of the reflected power deviation ΔP_r . The reflected power P_r is related to the incident power by the familiar expression

$$P_r = |\Gamma|^2 P_i \quad , \tag{4.44}$$

where the magnitude of the reflection coefficient $|\Gamma|$ is defined by

$$|\Gamma| = \frac{r_0 - 1}{r_0 + 1} \quad . \tag{4.45}$$

By taking the differential of (4.44) with respect to r_0, it can be shown that

$$\Delta P_r = |\Gamma| \, P_a \frac{\Delta r_0}{r_0} \quad . \tag{4.46}$$

Combining this result with (4.43) yields the following for the change in the power absorbed by the ferrite:

$$\Delta P_F = \frac{-\Delta P_r}{|\Gamma|} \quad . \tag{4.47}$$

Consider now that the change in ferrite absorption ΔP_F represents the increasing transient power loss due to the growth of instabilities within the ferrite. Since the growth of phonon instabilities is assumed to be the dominant transient loss mechanism, it may be concluded that

$$\Delta P_F = P_p \quad . \tag{4.48}$$

It is seen from (4.47) that $\Delta P_F(=P_p)$ is proportional to ΔP_r, the observable change in reflected power, provided the reflection coefficient Γ does not change appreciably. Since the resonant system is overcoupled, $-\Delta P_r$ will be positive and increasing as the ferrite losses increase. Hence the reflected power waveform will show a decrease with increasing time due to the phonon absorption.

The ideal situation from the standpoint of observation of instability thresholds is to have a maximum relative change in reflected power. Thus combining (4.44) with (4.47) and (4.48) yields

$$\frac{-\Delta P_r}{P_r} = \frac{P_p}{|\Gamma| \, P_i} \tag{4.49}$$

The increase in ferrite power absorption ΔP_F is given by

$$\Delta P_F = \omega_p U \Delta \left(\frac{1}{Q_0} \right) \quad . \tag{4.41c}$$

This power absorption takes place only when the Q_0 of the system is changed by introducing additional losses into the system--for instance, through growth of spin wave or elastic wave instabilities in the ferrite.

For an overcoupled resonator system, the external Q is given by

$$Q_{ext} = Q_0/r_0 \quad , \tag{4.42}$$

where r_0 is the voltage standing wave ratio (VSWR) at resonance. For a given position of the movable short, Q_{ext} is constant (see Chapter V). Therefore (4.41c) becomes

$$\Delta P_F = - P_a \frac{\Delta r_0}{r_0} \quad . \tag{4.43}$$

It is desired to obtain the ferrite absorption in terms of the reflected power deviation ΔP_r . The reflected power P_r is related to the incident power by the familiar expression

$$P_r = |\Gamma|^2 P_i \quad , \tag{4.44}$$

where the magnitude of the reflection coefficient $|\Gamma|$ is defined by

$$|\Gamma| = \frac{r_0 - 1}{r_0 + 1} \quad . \tag{4.45}$$

By taking the differential of (4.44) with respect to r_0, it can be shown that

$$\Delta P_r = |\Gamma| \, P_a \frac{\Delta r_0}{r_0} \quad . \tag{4.46}$$

Combining this result with (4.43) yields the following for the change in the power absorbed by the ferrite:

$$\Delta P_F = \frac{-\Delta P_r}{|\Gamma|} \quad . \tag{4.47}$$

Consider now that the change in ferrite absorption ΔP_F represents the increasing transient power loss due to the growth of instabilities within the ferrite. Since the growth of phonon instabilities is assumed to be the dominant transient loss mechanism, it may be concluded that

$$\Delta P_F = P_p \quad . \tag{4.48}$$

It is seen from (4.47) that $\Delta P_F (= P_p)$ is proportional to ΔP_r, the observable change in reflected power, provided the reflection coefficient Γ does not change appreciably. Since the resonant system is overcoupled, $-\Delta P_r$ will be positive and increasing as the ferrite losses increase. Hence the reflected power waveform will show a decrease with increasing time due to the phonon absorption.

The ideal situation from the standpoint of observation of instability thresholds is to have a maximum relative change in reflected power. Thus combining (4.44) with (4.47) and (4.48) yields

$$\frac{-\Delta P_r}{P_r} = \frac{P_p}{|\Gamma| \, P_i} \tag{4.49}$$

for the relative change in reflected power. The incident power P_i is determined by the threshold magnetic field amplitude at which the phonon absorption P_p reaches an observable level. Thus only $|\Gamma|$ remains to be chosen. It is clear, therefore, that the maximum relative change in reflected power will occur for the smallest reflection coefficient compatible with the minimum detectable reflected power.

D. APPARENT CRITICAL FIELD

The relationship between the phonon power absorption P_p and the apparent critical magnetic field amplitude h_{ap} will now be determined.

1. Ideal Pulse

The phonon absorption P_p for the ideal pulse may be found from (4.37a) by letting $\tau \rightarrow \infty$, since the ideal pulse is assumed to be perfectly flat. On defining $P_p = (P_p)_{ap}$ as the observed phonon absorption when saturation of the reflected pump pulse first appears, and recalling that $h = h_m$ (and $h_{ap} = h_{mp}$) for the ideal pulse, an expression may be obtained from (4.37a) for the apparent critical field h_{ap} as follows:

$$h_{ap} = h_{cr} + \frac{h_{cr}}{2\eta t_{ap}} \ln \frac{h_{cr}}{h_{ap}} \frac{(P_p)_{ap}}{2\eta N(t_{ap}) k_B T} \quad . \qquad (4.50)$$

The h_{ap} which appears in the log argument has only a second order effect on the actual value of h_{ap}. From (4.50) it is evident that the longer the build-up time t_{ap} of the phonon instabilities, the closer h_{ap} approaches h_{cr}. Thus, ideally, the critical threshold would be observed with an incident pump pulse of infinite length. Since the pulse must, practically, have a finite length, then it follows that the lowest apparent critical field h_{ap} will be observed at the end of the pulse--at which point the instabilities have had the longest time to grow. Hence the build-up time t_{ap} is equal to the pulse length in the ideal pulse case. It is also noteworthy that the smaller the observable change in the phonon power absorption P_p, the closer h_{ap} approaches the critical value. In practice, the critical field h_{cr} is never reached, and thus the factor h_{ap}/h_{cr} is always greater than unity for observable phonon instability thresholds. Nevertheless, it is possible to extrapolate back in order to find h_{cr} by measuring growth rates as a function of field amplitude h above the critical value.

2. Actual Pulse

The actual pulse, with its finite decay constant τ, is considered next. The phonon absorption P_p in this case is obtained from (4.37a) with τ finite. Solving (4.37a) for h_m in the same way as for the ideal pulse case yields the following result:

$$h_{mp} = \left(1 - \frac{t_{ap}}{4\tau}\right)^{-1} \left[h_{cr} + \frac{h_{cr}}{2\eta t_{ap}} \ln\left(\frac{h_{cr}\,(P_p)_{ap}}{h_{mp}\,2\eta N(t_{ap})\,k_B T}\right)\right], \quad (4.51)$$

where $(P_p)_{ap}$ is again the observed phonon absorption level when saturation of the reflected pump pulse first appears, and h_{mp} is the value of h_m at this threshold absorption level (see Fig. 4.3).

It would now be possible to write the apparent critical field h_{ap} (Fig. 4.3) in terms of (4.51). At this point, however, it is easiest to work with the field amplitude h_{mp}, and the results below will be given in terms of this quantity.

The value of t_{ap} is the chief difference between the actual and the ideal pulse cases. It can be seen by an examination of (4.51) and (4.50) that if t_{ap} is smaller for the actual pulse case, then the threshold will be higher. If the theory for the actual pulse is to be useful in practice, some criterion must be established for determining t_{ap}. From the expression (4.37a) for the phonon power it is noted that the dominant time-dependent factor is the exponential. Initially, as the time increases the exponential grows in magnitude. However, at sufficiently large times the effect of the pump field amplitude

$$h' \approx h_m(1 - t/\tau)$$

becomes significant and the absorbed power P_p goes through a maximum. The effect of the less significant time-dependent factor N is to cause this maximum to appear sooner than it otherwise would.

The assumption is now made that this maximum value of P_p is equal to $(P_p)_{ap}$ occurring at time t_{ap} (Fig. 4.3). The time-dependent portion of (4.37a) is

$$P_p \sim t^{-1/2} \; e^{2\eta t\left[-1 + \frac{h_m}{h_{cr}}\left(1 - \frac{t}{4\tau}\right)\right]} \quad . \tag{4.52}$$

Differentiating (4.52) to obtain the condition for a maximum value of P_p yields

$$t_{ap} = \tau\left(1 - \frac{h_{cr}}{h_{mp}}\right) + \tau\left[\left(1 - \frac{h_{cr}}{h_{mp}}\right)^2 - \frac{h_{cr}}{2\eta\tau h_{mp}}\right]^{1/2} \tag{4.53}$$

as the apparent build-up time of the instability. This result shows that the longer the pulse time constant τ , the longer is the time t_{ap} before the phonon absorption reaches a maximum--provided the pulse length is sufficiently long. If τ approaches infinity, then t_{ap} must approach the pulse length, as in the ideal pulse case.

An assumption is now made, which is justified in practice for the range of the parameters employed, that

$$\left(1 - \frac{h_{cr}}{h_{mp}}\right)^2 \gg \frac{h_{cr}}{2\eta\tau h_{mp}} \quad . \tag{4.54}$$

Using this approximation, (4.53) becomes

$$t_{ap} = 2\tau\left(1 - h_{cr}/h_{mp}\right) \quad . \tag{4.55}$$

Substituting (4.55) into (4.51) and solving for h_{mp}/h_{cr} yields the following result:

$$\frac{h_{mp}}{h_{cr}} = 1 + \frac{\ell}{2}\left[1 + (1 + 4/\ell)^{1/2}\right] \quad , \tag{4.56a}$$

where the definition has been made that

$$\ell = \frac{1}{2\eta\tau} \ln \frac{(P_p)_{ap}\, h_{cr}}{2\eta N(t_{ap})\, k_B T\, h_{mp}} \quad . \tag{4.56b}$$

In determining h_{mp}/h_{cr} , the higher order effect of h_{mp}/h_{cr} in the argument of the logarithm may be neglected to first order, and, if necessary, may be accounted for later by means of successive approximation.

From the above analysis for the actual pulse shape, estimates will now be made for the ratios h_m/h_{cr} and h_{ap}/h_{cr} as well as for the build-up time t_{ap} . The estimated value for the phonon Q_p (≈ 1500) from Chapter III will be used here. Taking the experimental parameters, $\tau = 309\ \mu\text{sec}$ and $(P_p)_{ap} = 0.74\ \text{W}$, associated with experiment I (Chapter VI), the following results are obtained from (4.56), (4.77) and (4.55):

(experiment I)

$$\frac{h_{mp}}{h_{cr}} = 1.202$$

$$\frac{h_{ap}}{h_{cr}} = 1.014 \tag{4.57}$$

$$t_{ap} = 104\ \mu\text{sec} \quad .$$

The pulse length was 120 μsec.

In a similar way, on taking the experimental parameters $\tau = 124\ \mu\text{sec}$ and $(P_p)_{ap} = 0.06W$ associated with experiment II (Chapter VI) we obtain the following results:

(experiment II)

$$\frac{h_{mp}}{h_{cr}} = 1.319$$

$$\frac{h_{ap}}{h_{cr}} = 1.036 \qquad (4.58)$$

$$t_{ap} = 60\ \mu\text{sec} \quad .$$

In this case the pulse length is 90 μsec. The build-up time, t_{ap}, is shorter in experiment II chiefly because the pulse decay time constant τ is shorter. The more sensitive detection used in experiment II also aided in reducing t_{ap}. The amplitude ratios h_{mp}/h_{cr} and h_{ap}/h_{cr} are higher for experiment II because the shorter the pulse decay time constant the higher must be the power level (or field level) to produce a given time average power level. A comparison of the calculated and observed values of t_{ap} will be made in the following section and in Chapter VI.

E. PHONON ABSORPTION EFFECTS

The expression for the theoretical phonon absorption P_p as a function of time is given by (4.37a). Since the effects of phonon absorption were observed in greater detail in experiment II, the theoretical nature of the phonon absorption for the parameters of experiment II will be investigated further. Taking the parameter values for experiment II and the ratio h_{mp}/h_{cr} [given above by (4.58)] for which the minimum detectable phonon power absorption takes place, (4.37a) may be plotted as a function of time. This plot is shown in

Fig. 4.7. The peak absorption occurs at $t_{ap} = 60\ \mu\text{sec}$, as predicted by (4.55). The curve is not quite symmetrical about $t = t_{ap}$, but is, in fact, slightly steeper for t less than t_{ap}.

Next, the effect of this absorption upon the reflected pump pulse will be predicted. Combining (4.2) with (4.44), the reflected pump waveform in the absence of instability is given by

$$P_r = P_{rm}\, e^{-t/\tau} \quad , \tag{4.59}$$

where

$$P_{rm} = |\Gamma|^2\, P_{im} \quad .$$

The reflected pump waveform (4.59) is plotted in Fig. 4.8a for the experiment II value of τ and for an arbitrary power level below threshold. At threshold power levels, (4.59) is incomplete because the effect of the phonon absorption upon the total reflected power must be considered. Then the total reflected power $(P_r)_{tot}$ becomes

$$(P_r)_{tot} = P_r + \Delta P_r \quad , \tag{4.60}$$

where P_r is given by (4.59), and the change in reflected power ΔP_r is found from (4.47) and (4.48) to be

$$\Delta P_r = -\,|\Gamma|\, P_p \tag{4.61}$$

for the overcoupled case. Since ΔP_r is small, it will be assumed that $|\Gamma|$ does not change significantly during the growth of $P_p(t)$.

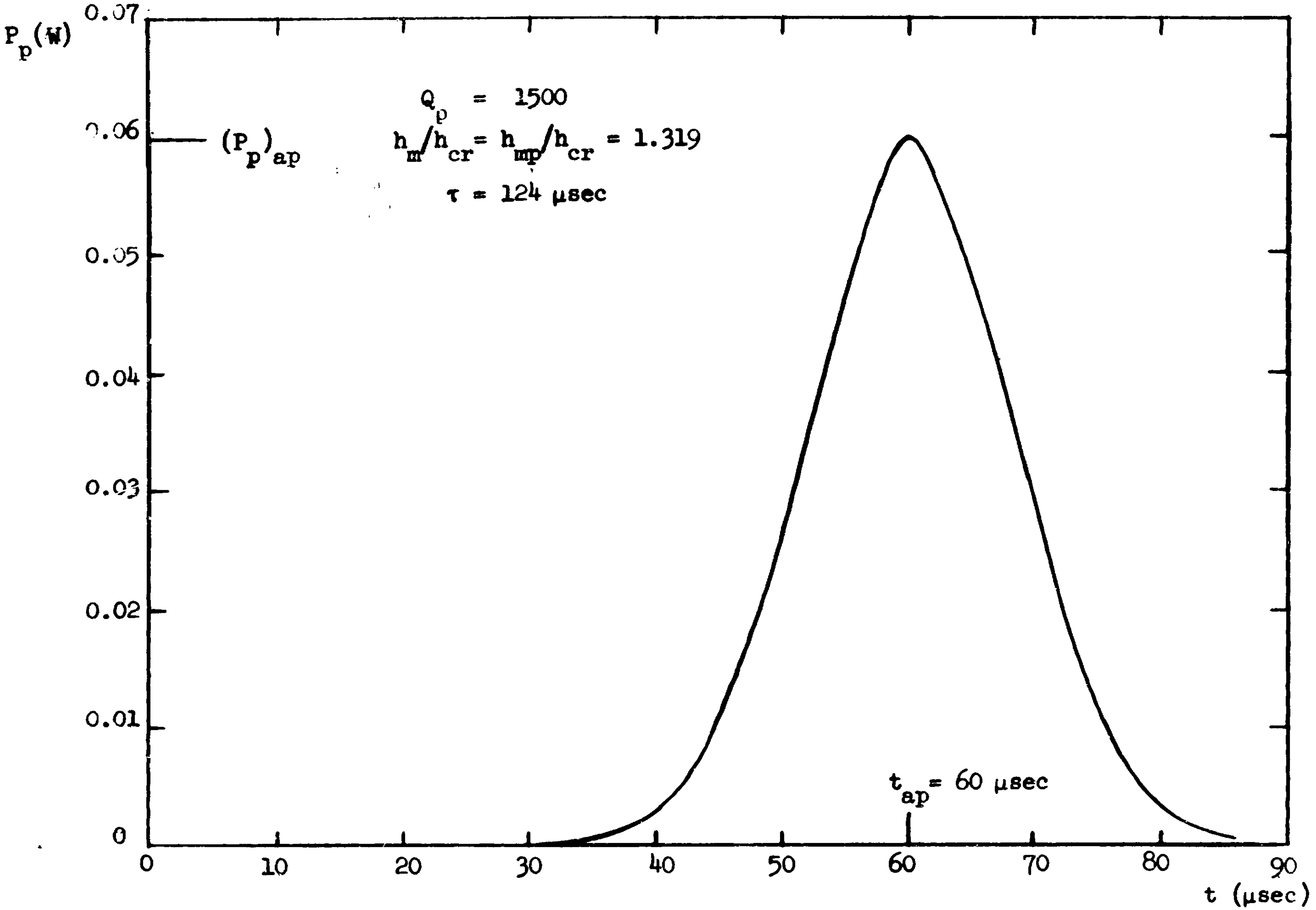

FIG. 4.7--Theoretical phonon absorption (4.37a) at the apparent threshold for experiment II.

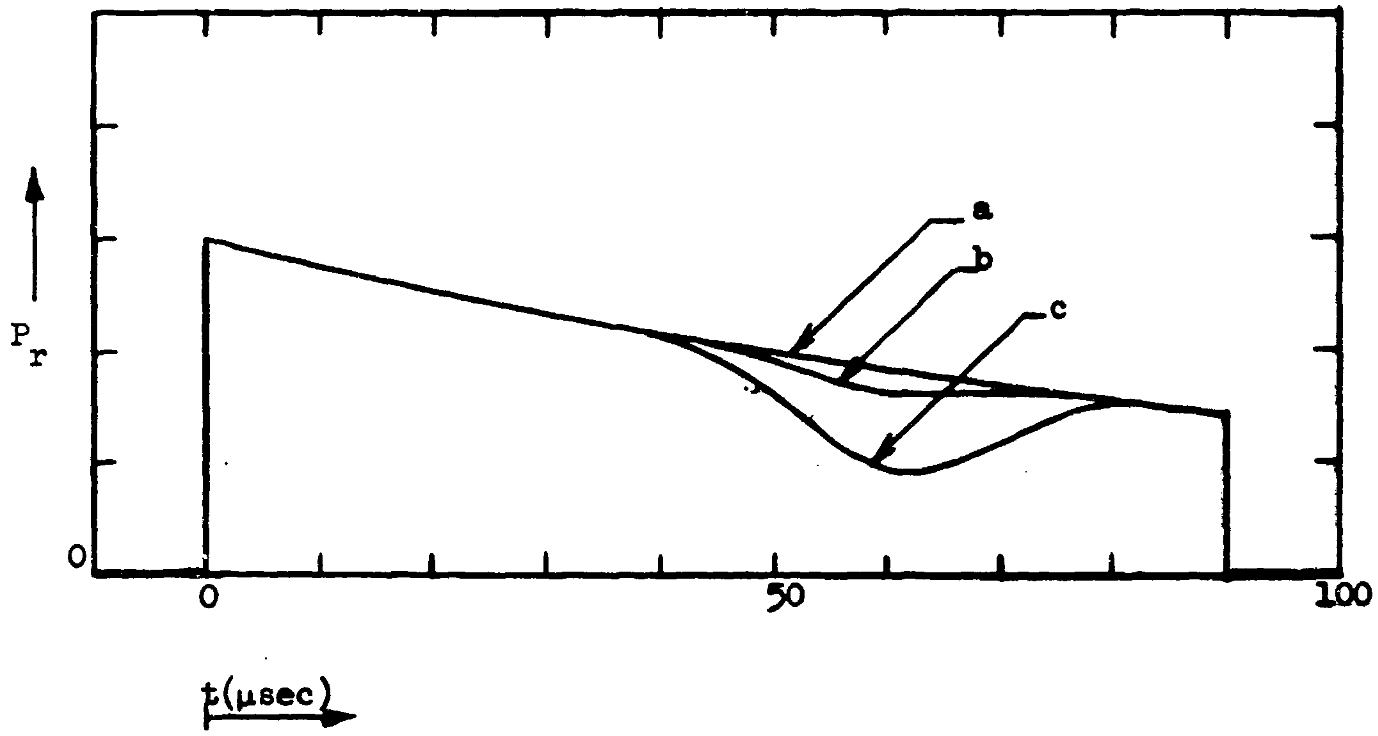

Normalized phonon absorption curves for:

(a) $\frac{h_{mp}}{h_{cr}} < 1.319$, $\frac{h_{ap}}{h_{cr}} < 1.036$

(b) $\frac{h_{mp}}{h_{cr}} = 1.319$, $\frac{h_{ap}}{h_{cr}} = 1.036$, $(P_p)_{ap} = 0.06$ W

$t_{ap} = 60$ μsec

(c) $\frac{h_{mp}}{h_{cr}} = 1.327$, $\frac{h_{ap}}{h_{cr}} = 1.036$, $(P_p)_{ap} = 0.26$ W ,

$t_{ap} = 61.2$ μsec

FIG. 4.8--Normalized reflected power vs time showing the predicted phonon absorption for the parameters of experiment II and $Q_p = 1500$.

Assume now that the ratio of the minimum observed change in reflected power to the reflected power at the apparent threshold is given by

$$\left(\frac{\Delta P_r}{P_r}\right)_{ap} = 0.1 \quad . \tag{4.62}$$

Recall that the phonon absorption build-up to and decay from the apparent threshold peak was plotted in Fig. 4.7 for this case. Through (4.62), (4.60), and Fig. 4.7, the effect of the phonon absorption upon the reflected pump pulse is determined, and the result is plotted in Fig. 4.8b. The reflected pulses for cases (a) and (b) have been normalized in order to show best the deviation in the pulse waveform due to the phonon absorption.

At a still higher ratio of ΔP_r to P_r of

$$\left(\frac{\Delta P_r}{P_r}\right)_{ap} = 0.5 \quad , \tag{4.63}$$

a similar result obtains and is shown in Fig. 4.8c. The curve is again normalized as above. Note the build-up time t_{ap} is slightly longer in this case--in accordance with (4.55). Values of the parameters for each of the above three cases are shown in Fig. 4.8.

The above theory is based upon the assumption that $|\Gamma|$ = constant. However, the fact that $|\Gamma|$ varies by 40% during the pulse [as in case (c)] is not enough to alter significantly the nature of the absorption during the pulse. This is due to the sharpness of the absorption peak. If the variation in $|\Gamma|$ becomes much larger, however, the phonon absorption peak will appear broadened due to two effects. The first follows from (4.47), where the effect of a smaller $|\Gamma|$ is to make the change in reflected power smaller, i.e., a given phonon absorption appears smaller.

The second is due to the effect of a smaller $|\Gamma|$ in decreasing ΔP_{fld} in (4.41a) [see also (4.47) and (4.39)], and hence the rf magnetic field amplitude. The latter has the effect of reducing the growth rate of the absorption [through reduction of h_m/h_{cr} in (4.37a)].

The phonon absorption shown in Fig. 4.8 has been observed experimentally, and the actual waveforms of the pump pulse will be discussed in Chapter VI. The build-up times observed experimentally were considerably shorter than those calculated [(4.57) and (4.58)]. This may imply that the phonon Q_p is actually lower than originally estimated. Following a process almost the reverse of that used above, a value of Q_p can be determined which will correspond to the observed build-up time $(t_{ap})_{exp}$. For instance, knowing $(t_{ap})_{exp}$, then h_m/h_{cr} is found from (4.55) to be

$$h_{mp}/h_{cr} = 1 + \frac{1}{2\tau/t_{ap} - 1} \quad . \qquad (4.64)$$

Having a result for h_{mp}/h_{cr} , the result

$$\ell = (h_{mp}/h_{cr} - 1)^2 / \frac{h_{mp}}{h_{cr}} \qquad (4.65)$$

follows from (4.56a). The value of Q_p may than be determined from the expression (4.56b) for ℓ . Taking the observed build-up time of $(t_{ap})_{exp} = 32$ µsec for experiment I with other parameter values given previously, the value of Q_p obtained is

$$Q_p = 127 \qquad \text{(experiment I)} \qquad (4.66)$$

with

$$h_{mp}/h_{cr} = 1.055$$

$$h_{ap}/h_{cr} = 1.003 \quad .$$

Taking the observed build-up time of $(t_{ap})_{exp} = 28\ \mu\text{sec}$ for experiment II with previously given parameter values, the Q_p in this case becomes

$$Q_p = 294 \qquad \text{(experiment II)} \tag{4.67}$$

with

$$h_{mp}/h_{cr} = 1.127$$

$$h_{ap}/h_{cr} = 0.961 \quad .$$

It is expected on the basis of the linear theory that the two above values of Q_p should be equal. However, if nonlinear damping is present this need not be required. In such a case the above Q_p's may be spoken of as "effective" Q_p's . The nature of nonlinear damping is not known, but the effect of such damping would most likely be to cause the Q_p in (4.37a) to decrease with increasing phonon absorption. This is precisely the relationship which exists for the above results (4.66) and (4.67). A further substantiation of the presence of nonlinear damping is seen in the reflected pump waveforms of experiments I and II of Chapter VI, where the build-up time was found to decrease with increasing absorption levels. Such an observation is contrary to the result (4.55) from the linear theory with Q_p constant, where the reverse is predicted. However, if the "effective" Q_p is allowed to decrease with increasing phonon absorption, then the linear theory [see (4.37)] will also predict the observed behavior.

F. SUMMARY

The various loss mechanisms of a ferrite are discussed briefly. Interest here was in operation at a pump frequency and dc magnetic field where the phonon threshold will dominate other instability thresholds. The elastic wave equation obtained from Chapter III for waves having the lowest threshold was modified to include the time variation of the pumping angle arising from experimental limitations. An approximate solution to this equation was found for values of the pumping angle above the critical threshold angle. A calculation of the power being absorbed by the unstable elastic modes was then made by assuming growth of these modes from thermal energy levels. The effective number of growing modes was found to be a function of time and depends upon the value of the pumping angle above the critical angle, as well as upon the ferrite sample dimensions, phonon Q , and effective internal dc field. The absorption observable experimentally on the reflected pump pulse was found to be proportional to the phonon absorption by the ferrite and inversely proportional to the reflection coefficient.

The optimum conditions required for observation of the relative change in reflected power were also discussed. The apparent critical magnetic field was derived for the ideal and actual pulse cases in terms of the phonon absorption level which is first observable experimentally. The build-up time corresponding to this absorption level was also derived. For experimental and ferrite parameters the phonon absorption and its effect upon the reflected pump pulse were calculated for the actual pulse. The theoretical build-up time to the phonon absorption peak was found to be longer than that observed experimentally. It is suggested that nonlinear damping is present.

CHAPTER V

EXPERIMENTAL TECHNIQUES AND MICROWAVE PARAMETER MEASUREMENTS

A. MICROWAVE CIRCUITRY FOR THRESHOLD MEASUREMENTS

The rf magnetic field required in order to observe the phonon threshold may be estimated from the theoretical results of Chapter III. From Fig. 3.3, a typical threshold angle may be taken to be

$$(A_p)_{cr} \approx 0.1 \quad .$$

Assuming a dc magnetic field of $H_0 \approx 400$ Oe, the amplitude of the critical rf magnetic field will be

$$h_{cr} \approx 40 \text{ Oe} \quad .$$

To achieve such a high rf field at the frequency of interest (1.32 kMc), a conventional metal cavity was first considered. Large incident power levels (~ 100 kW) would be required to achieve the desired rf field strength. This is unfortunate because high voltage breakdown within the cavity is likely to occur at these power levels. The conventional metal cavity at 1.32 kMc also has the disadvantage of having a small filling factor for a ferrite.

Since the prospect of breakdown was to be avoided and a large filling factor was desired, other methods of resonating a microwave electromagnetic field were investigated. Such a method was found in the dielectric resonator.[28,29] A dielectric resonator having a high dielectric constant was considered. In such a case the possibility of breakdown is practically eliminated. Also, a large filling factor can be obtained because the resonator volume is small. Furthermore, large rf fields can be obtained with considerably lower incident power levels than would be required for a metal cavity.

A dielectric resonator was fabricated from single crystal strontium titanate. Strontium titanate possesses a very high isotropic dielectric constant ($\epsilon' \approx 277$), a low loss tangent, and is commercially available in large single crystal boules. With such a high dielectric constant, the resonator dielectric volume at 1.32 kMc was only 1.28 cm^3, and a large ferrite filling factor was obtained. A resonator system Q of over 1000 was also obtainable. Thus, direct observation of absorbed power by the ferrite was easily possible.

In order to achieve the large rf magnetic fields with the dielectric resonator, it was still necessary to employ a moderately high microwave power source--one having a maximum power output of about 50 W peak. Thermal limitations of the dielectric resonator and ferrite dictated pulsed rather than cw operation. The microwave power source was provided by a 500 mW signal generator (General Radio GR-1218-A) in conjunction with an L-band klystron amplifier (Raytheon SAL-81), shown in Fig. 5.1. The klystron beam was pulsed by the high voltage pulser modulator (Levinthal 79-M). The modulator contained the power supply which charged up a 15 kV 1 μfd capacitor. The pulsed discharge from the capacitor furnished the beam current for the klystron. The pulse length, or length of each discharge time, was about 100 μsec. This was long enough to enable observation of the predicted phonon absorption peak. The pulse length was determined by a multivibrator circuit which controlled the capacitor discharge through a vacuum tube circuit. The switching characteristics were limited to a large extent by the quality of the transformer employed at the output of the multivibrator circuit. For transformers available, a compromise had to be made between fast rise and fall times and minimum sag for the 100 μsec pulse. The effect of the transformer sag was, of course, to enhance the sag in the capacitor discharge and hence in the amplified rf output. The pulse repetition rate was controlled by the pulse trigger external to the modulator
It was necessary to make the pulse repetition rate as low as possible

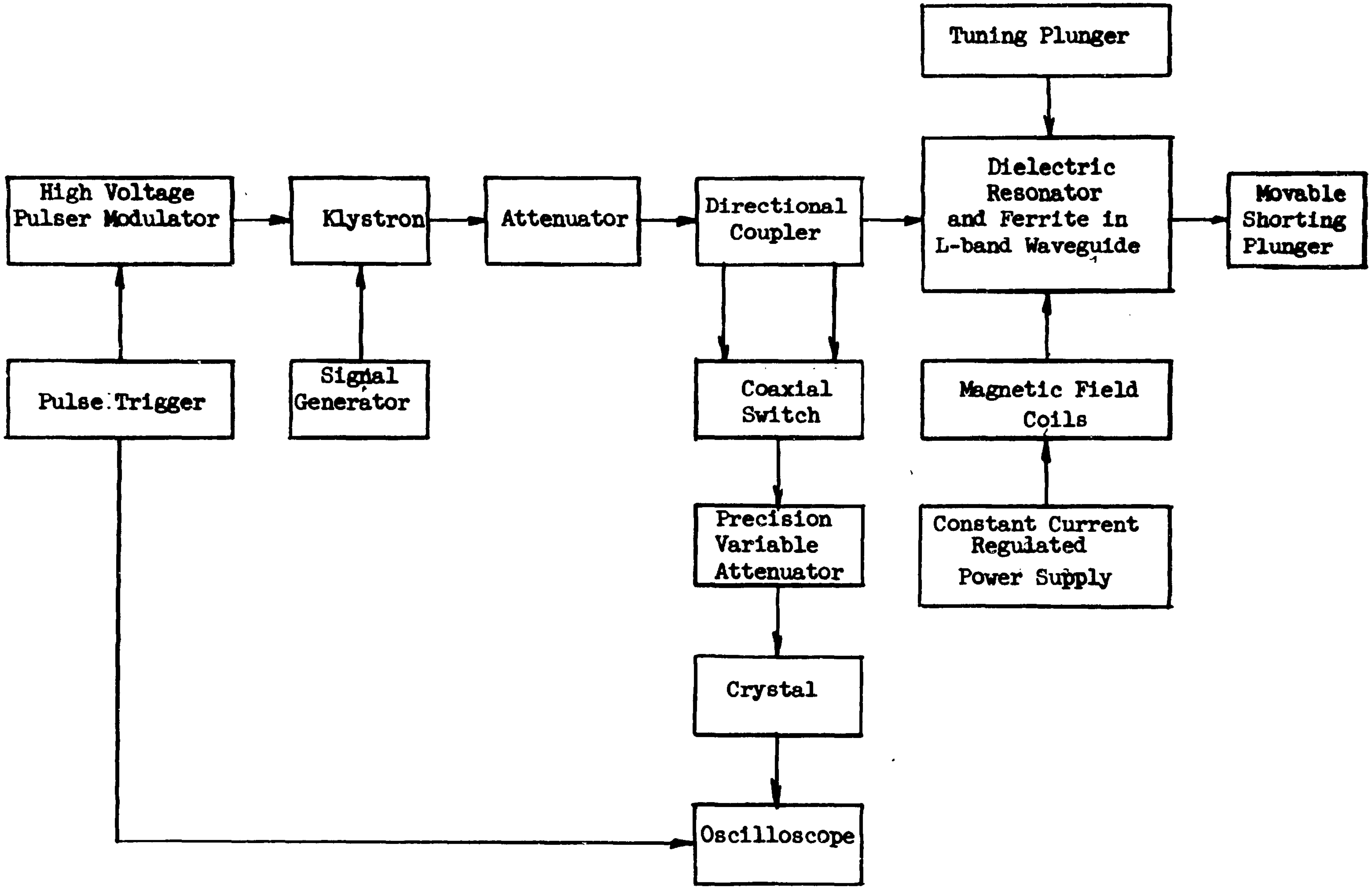

FIG. 5.1--Arrangement of apparatus for transverse pumping experiment.

in order to minimize the sag in the capacitor discharge current. Yet this rate had to be sufficiently high to give a continuous display of the power pulse waveforms on the long persistence screen of the oscilloscope. This determined the pulse repetition rate of 10 cps.

An attenuator pad served to improve the impedance match of the klystron to its load. After the attenuator pad, a dual-directional coupler was inserted for the purpose of detecting incident and reflected power from the dielectric resonator. The output of the dual-directional coupler was fed to a precision variable attenuator (Hewlett-Packard HP-394-A). The crystal at the output of this attenuator detected the power level. All power measurements were made at the convenient minimum signal level of 2 cm deflection (0.1V) on the oscilloscope. Thus, for any given power input to the load, there was a corresponding setting of the precision variable attenuator which gave a 2 cm deflection on the oscilloscope. The variable attenuator was originally calibrated with a thermistor as a load. The thermistor was used in conjunction with a power meter to determine the average power level for each attenuator setting over the desired power range. Knowing the pulse length, pulse repetition rate, and the average power, the peak power level was obtained and the attenuator calibrated accordingly.

The circuitry connections for the above apparatus were made with 7/8 in. and type-N coax. An adapter to the standard L-band rectangular waveguide was employed at the output of the directional coupler. The waveguide provided a means of coupling power to the dielectric resonator. Sufficient spacing between the dielectric resonator and the adapter was allowed to avoid any higher order electromagnetic fringe fields arising from the transition.

The dc magnetic field was first applied across an air gap the width of the L-band waveguide. The field was obtained from an improvised magnet fabricated from two large toroidal field coils and iron bars. The latter provided the necessary low reluctance flux path. With the field coils located near the pole faces (for maximum gap flux), a sufficiently large and fairly uniform dc magnetic field was attained. The magnetic field was first calibrated by a gaussmeter of the Hall effect type--

which was later calibrated by a nuclear magnetic resonance (NMR) probe. The first set of experimental threshold measurements (hereinafter referred to as experiment I) were made by using this magnet and the setup of Fig. 5.1.

Another set of threshold measurements (hereinafter referred to as experiment II) was made with a large commercial magnet (Varian 12 in.). In this case the height of the L-band waveguide had to be reduced to 3 in. to fit inside the magnet air gap. For both magnets a constant current regulated power supply served to maintain a constant magnetic field with a minimum of drift due to coil heating. With the Varian magnet it was possible to obtain a broader range of magnetic field and a greater magnetic field uniformity at the sample, and an NMR probe could be used directly to calibrate the field. Another improvement in experiment II included a circulator, which increased the sensitivity of the critical field measurements.

B. DIELECTRIC RESONATOR SYSTEM

The dielectric resonator system will now be described in greater detail. The experimental arrangement is shown in Fig. 5.2. The dimensions of the strontium titanate dielectric resonator were 0.430 in. × 0.431 in. × 0.423 in. It has been mentioned already that the properties of strontium titanate utilized were its low loss tangent and its very high and essentially isotropic dielectric constant ($\epsilon' = 277$). The rod shown supporting the resonator also had a low loss tangent, but it had a low dielectric constant. The dielectric resonator was located in the center of the L-band waveguide cross-section. A hole (0.061 in.) was cut in the resonator as shown and a ferrite disk (0.054 in. diam × 0.0076 in.) supported by a glass rod was inserted. This resonator operated in the dominant H mode at 1.32 kMc. In the field configuration of this mode the maximum H field occurs at the center of the resonator and is polarized in the direction of the glass rod (see Fig. 5.3). Since the E field is weakest where the H field is strongest, the hole distorts the field pattern very little. The coupling of the resonator H mode to the standing waveguide TE_{10} mode was optimized by positioning the movable short.

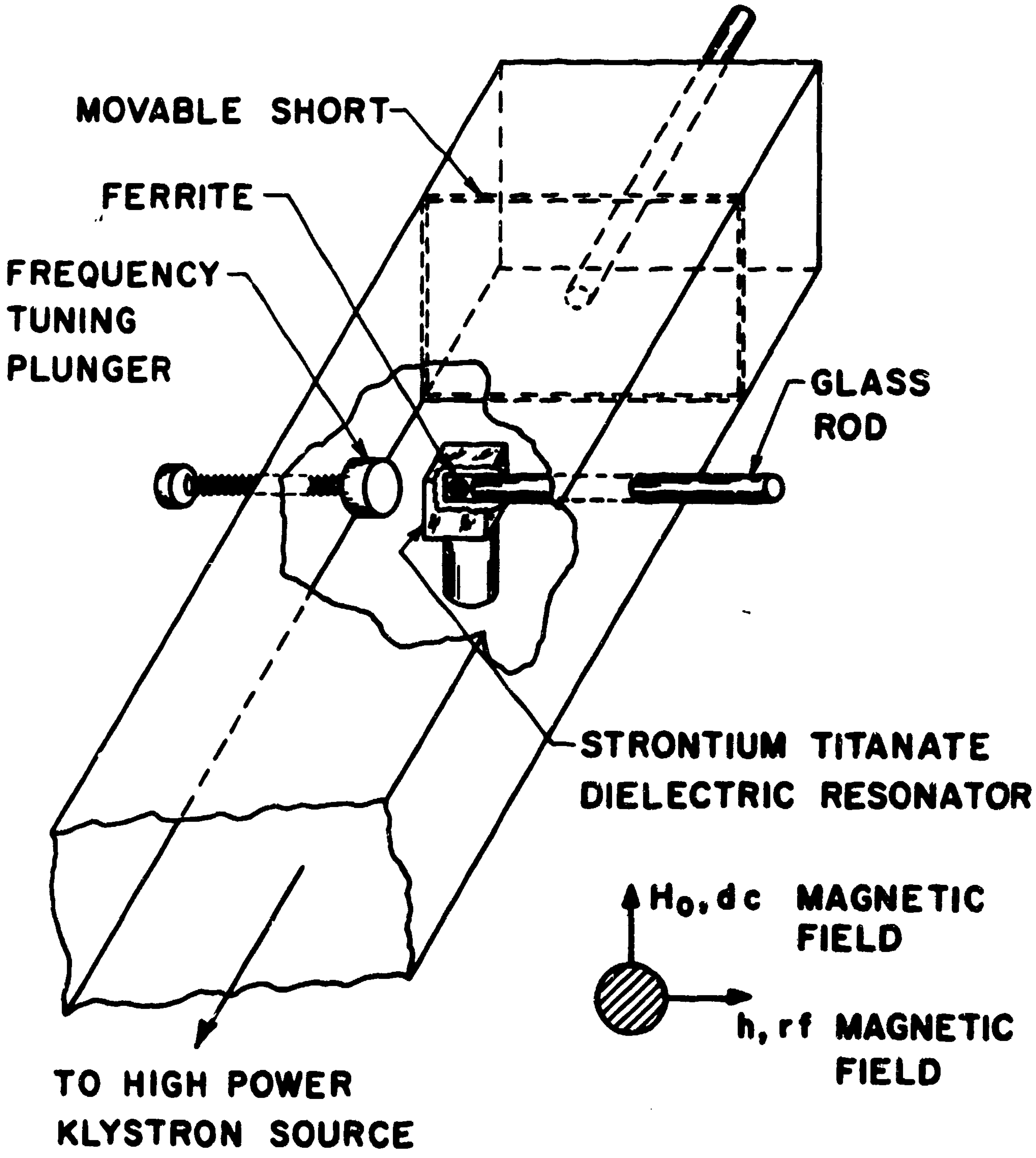

FIG. 5.2--Setup for ferrite transverse pumping experiment using strontium titanate dielectric resonator.

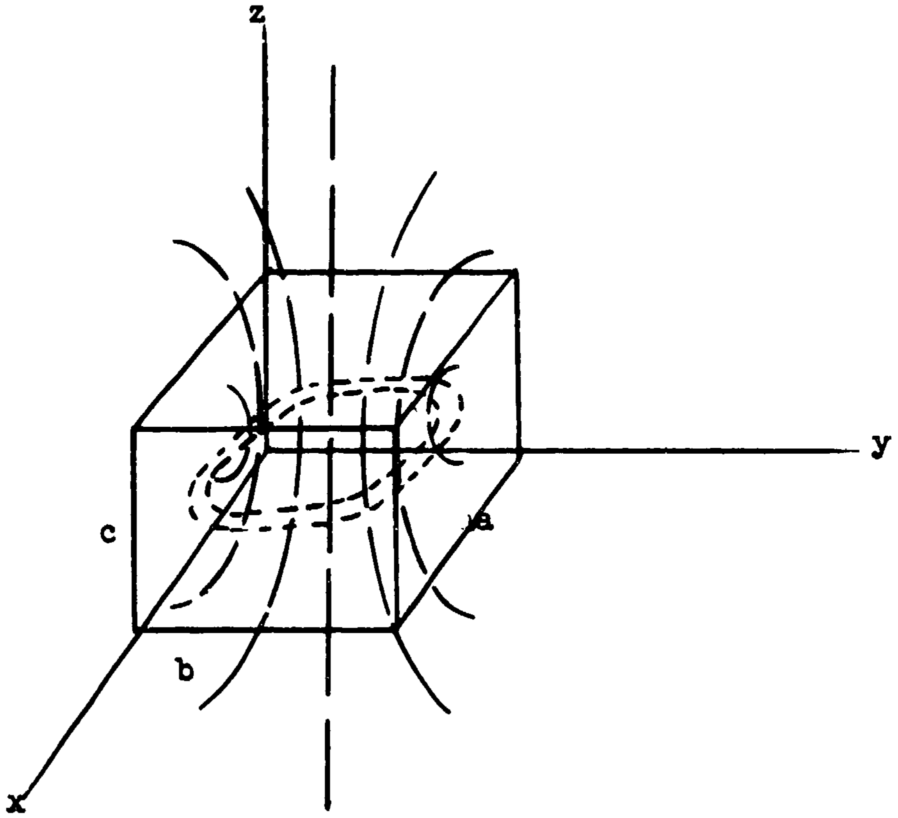

------Electric field lines

___ ___Magnetic field lines

FIG. 5.3--Dielectric resonator shown with coordinate system and a few of the electric and magnetic field lines for the dominant H-mode.

The properties of the ferrite and of the dielectric resonator were found to be significantly temperature-dependent. The ambient temperatures of the resonator and ferrite sample were determined by mounting a thermocouple on the post supporting the dielectric resonator. The dielectric constant of the resonator had the greatest sensitivity to temperature changes as far as the actual threshold measurements were concerned, since the resonator frequency was thereby affected. A frequency perturbation plunger was employed to compensate for this effect. The temperature coefficient of the resonant frequency was about 2.5 Mc/°C. The plunger was capable of changing the resonant frequency over a range of about 25 Mc. With the three cavity klystron adjusted for 1.32 kMc, it was then possible to resonate the dielectric resonator over an ambient temperature range of about 10°C. It was found desirable to perform experiments at ambient temperatures where the plunger could be maintained as far as possible from the resonator and still provide adequate frequency tuning during the data runs. This minimized distortion of the resonator rf field and reduced the dependence of the unloaded Q_0 upon the plunger position.

C. HEATING OF THE DIELECTRIC RESONATOR AND FERRITE

Heating of the dielectric resonator and ferrite due to microwave power absorption will now be investigated. First consider the dielectric resonator without the ferrite. The average microwave power, p_a , absorbed by the dielectric resonator system is dissipated through dielectric loss in the strontium titanate resonator, the dielectric supporting rod, the Ducco cement contact between the rod and resonator, finger contacts of the movable short, and waveguide walls. The power, p_d , actually dissipated in the vicinity of the resonator may be given by

$$p_d = c_1 p_a \quad . \tag{5.1}$$

Assuming that the support rod and the cement contact have a somewhat lower loss than the dielectric resonator, it is estimated that $c_1 = 0.5$.

The energy dissipated within the resonator volume is related to the temperature increase ΔT by

$$E_d = f_d c_d \rho_d V_d \Delta T \qquad , \tag{5.2}$$

where c_d is the specific heat, ρ_d is the density, and V_d is the volume of the dielectric resonator. The factor f_d is a factor greater than unity and is used to account for other energy losses in the vicinity of the resonator due to thermal conduction, convection, and radiation. Equating (5.2) to the energy input $p_d \Delta t$ yields the following for R_d , the rate of change of resonator temperature with time:

$$R_d = \frac{dT}{dt} = \frac{p_d}{f_d c_d \rho_d V_d} \ . \tag{5.3}$$

Taking the typical average power level $p_a = 10$ mW (corresponding to 10W peak power and 10^{-3} duty cycle), and using the values of c_d and ρ_d for strontium titanate given in Appendix A, and the resonator volume $V_d = 1.28 \text{ cm}^3$, R_d is estimated to be

$$R_d(10 \text{ mW}) = \frac{0.23}{f_d} \ ^{\circ}\text{C/min} \qquad , \tag{5.4}$$

where f_d has yet to be evaluated.

The temperature dependence of the strontium titanate dielectric constant strongly affected the resonant frequency of the dielectric resonator. From the value of the temperature coefficient of the dielectric constant given in Appendix A it can be shown that the temperature coefficient of the resonant frequency is about 2.5 Mc/°C. This dependence was observed experimentally as described in the previous section. The time rate of change of resonator frequency at the 10 mW average power level was also observed experimentally. From these observations the time rate of change of resonator temperature was found to be

$$R_{d_{\mathrm{exp}}}(10\ \mathrm{mW}) = 0.07\ {}^{\circ}\mathrm{C/min} \quad . \tag{5.5}$$

By comparison with (5.4) it is estimated that $f_d = 3.3$.

Equation (4.53) expresses the relation between the peak pulse absorbed power P_a and the peak pulse stored energy U in the dielectric resonator system. For the average absorbed power $\bar{p}_a$ and the average stored energy $\bar{u}$, the relation is

$$\bar{p}_a = \frac{\omega_p \bar{u}}{Q_0} \quad . \tag{5.6}$$

This expression applies, of course, to the resonator system with or without the ferrite present. The effect of the ferrite upon $\bar{u}$ is very small. The ratio of the ferrite volume to the volume of the dielectric resonator is of the order of 10^{-4} . Even if the ferrite has a relative permeability as large as 100, the effect of the ferrite upon the stored energy $\bar{u}$ will be negligible (~ 1%) . The effect of the ferrite upon the Q_0 is about an order of magnitude larger. In fact, a typical change in Q_0 observed experimentally was about 10%.

Considering only the effect upon Q_0 , the average power absorbed by the ferrite is found to be

$$\bar{p}_F = \frac{-\bar{p}_a \Delta Q_0}{Q_0} \tag{5.7}$$

Thus the ratio of the total average power absorbed by the ferrite to the average power absorbed by the resonator system is given approximately by the relative change in Q_0 .

The time rate of change of temperature of the ferrite is

$$R_F = \frac{p_F}{f_F \, c_F \, \rho_F \, V_F} \quad , \qquad (5.8)$$

where the parameters are counterparts of those used in (5.3). The factor f_F which accounts for conduction, convection, and radiation losses of the ferrite is expected to be larger than the factor for the resonator. This is because the broad face of the ferrite is mounted on a glass rod which provides a fairly good heat sink--thereby promoting large conduction losses. The dielectric support for the resonator conducts heat away from about one-sixth of the resonator surface area, whereas the glass rod conducts heat away from about one-half of the ferrite area. Consequently, it might be estimated that $f_F = 3f_d$. Thus, with a ferrite volume $V_F = 2.86 \times 10^{-4}$ cm^3 and the values given in Appendix A for the other quantities, (5.8) becomes

$$R_F(10 \text{ mW}) = 0.38 \ {}^{\circ}\text{C/sec} \quad . \qquad (5.9)$$

Therefore, if it takes 10 sec to determine the data for one experimental point, then the temperature increase of the ferrite would be about $\Delta T = 3.8^{\circ}\text{C}$. It is clear that measurements must be taken quickly at these high power levels. The threshold level was usually determined as quickly as possible, but never in much less than about 10 sec. After each threshold measurement the incident power was reduced and the sample was allowed to cool before the next measurement was taken. It was assumed that the ferrite reached the ambient temperature during this cooling period.

At the lowest power levels of about $P_a = 1$ W peak, the estimated ferrite temperature increase for a 10 sec measurement time would be $\Delta T = 0.38^{\circ}\text{C}$. Here, then, the actual temperature of the ferrite differs little from the equilibrium value. This equilibrium temperature was determined experimentally by attaching a thermocouple to the dielectric rod supporting the resonator.

With a pulse repetition rate of 10 cps, the average temperature increase of the ferrite during each pulse was a factor of 10 smaller than the average temperature increase of the ferrite in one second. Thus, heating effects during the pulse were negligible at the average power levels considered.

D. MAGNETIC FIELD DISTRIBUTION IN THE DIELECTRIC RESONATOR

The basic relation between the stored energy U in the rf magnetic field of the resonator and the peak pulse power P_a absorbed by the system is given by Eq. (4.40). In this section, U will be obtained in terms of the maximum rf magnetic field amplitude h_0 .

The rectangular parallelepiped dielectric resonator, together with the coordinate system used to describe the electric and magnetic fields for the dominant H mode, is shown in Fig. 5.3. The electric field is strongest near the resonator faces parallel to the z-axis, while the magnetic field is strongest in the center of the resonator and along the z direction. A few of the strongest field amplitude lines are sketched in Fig. 5.3.

Open circuit boundary conditions (OCB) require that the electric field be parallel to and the magnetic field normal to the boundary. For the dominant H mode described above it is found that at the faces of the dielectric resonator parallel to the z-axis, the OCB conditions are nearly satisfied, since the relative dielectric constant ϵ' is much greater than unity. The advantage of recognizing OCB conditions is that the theory is simplified by terminating the electric and magnetic fields at the air-dielectric boundary. For the faces of the resonator normal to the z-axis, the usual boundary conditions for electric and magnetic fields are used. Using Yee's results[29] for the special case of a rectangular parallelepiped with a square cross section (a=b) , the electric fields based upon the above assumptions are given by

$$E_x = \frac{-j\omega\mu_0 a h_0}{2\pi} \sin \frac{\pi x}{a} \cos \frac{\pi y}{b} A(z) \qquad (5.10a)$$

and

$$E_y = \frac{j\omega\mu_0 a h_0}{2\pi} \cos\frac{\pi x}{a} \sin\frac{\pi y}{b} A(z) \quad , \qquad (5.10b)$$

where h_0 is defined as the maximum value of the magnetic field (at the center of the resonator). Inside the resonator $A(z)$ is defined by

$$A(z) = \cos\zeta\left(z - \frac{c}{z}\right) \quad , \qquad (5.10c)$$

and outside by

$$A(z) = A_0 e^{-\zeta_0\left|z - \frac{c}{z}\right|} \quad , \qquad (5.10d)$$

where the quantity A_0 is obtained by matching boundary conditions at $z = 0$ or c. The quantities ζ and ζ_0 are defined approximately by the relations

$$\frac{\zeta c}{2} \tan\frac{\zeta c}{2} = \frac{\pi}{\sqrt{2}} \frac{c}{a} = \frac{\zeta_0 c}{2} \quad . \qquad (5.11)$$

The magnetic field components may easily be determined by substituting (5.10) into Maxwell's equations. Also from Maxwell's equations, the following expression for the resonant frequency is derived:

$$f_{res} = \frac{1}{2\sqrt{\mu_0\epsilon_0\epsilon'}} \left[\frac{2}{a^2} + \left(\frac{\zeta}{\pi}\right)^2\right]^{1/2} \quad . \qquad (5.12)$$

It was by inserting experimental values for $a = b$, c and the resonant frequency f_{res} into (5.12) that the experimental value for strontium titanate of $\epsilon' = 277$, given in Appendix A, was obtained. This result agrees favorably with values measured by others.[28,29]

The total stored energy in the resonator system is most simply given by the integral of the electric energy density when the latter is a maximum in time, for example

$$U = \frac{1}{2} \int_{\text{space}} \epsilon \, |\underset{\sim}{E}|^2 \, dxdydz \quad . \tag{5.13}$$

It is now assumed that the OCB conditions at the resonator faces parallel to the z-axis, which apply approximately to the fields within the resonator, apply equally well outside of the resonator. With this assumption, the result of taking the integral (5.13) over all space is

$$U = f \frac{1}{8} \mu_0 h_0^2 V_d \quad , \tag{5.14a}$$

where, for a = b the factor f is given by

$$f = \frac{1}{2} \left\{ 1 + \left(\frac{a}{c}\right)^2 \left(\frac{\zeta c}{\pi}\right)^2 + \frac{\sin \zeta c}{\zeta c} \left[1 + \left(\frac{\zeta c}{\zeta_0 c}\right)^2 \right] \right\} \quad . \tag{5.14b}$$

By solving (5.11) and ζc and $\zeta_0 c$, using the resonator dimensions given previously, the value of f obtained is $f = 0.86$. It is interesting that this value of f is comparable to the value of unity which would be obtained if there were no z-dependence of the fields and if all of the energy were contained within the resonator volume.

In deriving the above results, OCB conditions were assumed at four faces of the rectangular parallelepiped dielectric resonator as well as at the extension of these faces external to the resonator. For strontium titanate, the relative dielectric constant is high ($\epsilon' = 277$); and the OCB conditions are well satisfied within the resonator. However, it is not clear how good the OCB assumption is outside the resonator. This problem could, of course, be overcome by solving for fields satisfying the exact boundary conditions, but this would be impossible for the rectangular parallelepiped, except by numerical methods.

There is, fortunately, another alternative by which the validity of the approximate solution for the rectangular resonator may be checked. The spherical dielectric resonator operating in the dominant H mode has electric and magnetic field configurations quite similar to those of the rectangular parallelepiped operating in the same mode. What makes the spherical dielectric resonator of special interest is that the electric and magnetic fields can be determined exactly, and therefore an exact expression for the energy storage can be derived. Using the energy relations given by Yee[29] for the dominant H_{110} mode of the dielectric sphere (where the exact resonance condition for the sphere has been employed), the factor f defined by (5.14a) is found to be $f = 0.85$. Thus a dielectric sphere having the same volume V_d as the rectangular parallelepiped, but necessarily a slightly higher frequency (4%), has about the same energy storage. This result makes more reasonable the original assumption of OCB conditions for the rectangular parallelepiped dielectric resonator, and in particular the extension of these conditions external to the resonator.

On combining (4.53) and (5.14a), the expression for h_0 becomes

$$h_0 = \left(\frac{8P_a Q_0}{f\mu_0 V_d \omega_P}\right)^{1/2} \qquad (5.15)$$

By inserting the aforementioned parameter values, then (5.15) becomes

$$h_0 = 0.332\,(P_a Q_0)^{1/2} \quad . \qquad (5.16)$$

The ferrite is located in the center of the dielectric resonator in the actual experiment, and therefore it is worthwhile to investigate the variation of the magnetic field near this point. Figure 5.4 shows the variation of the dominant magnetic field component h_z as a function of z for $x = a/2$ and $y = b/2$. The magnetic field h_z is a maximum at the center of the resonator and has the same kind of z-variation

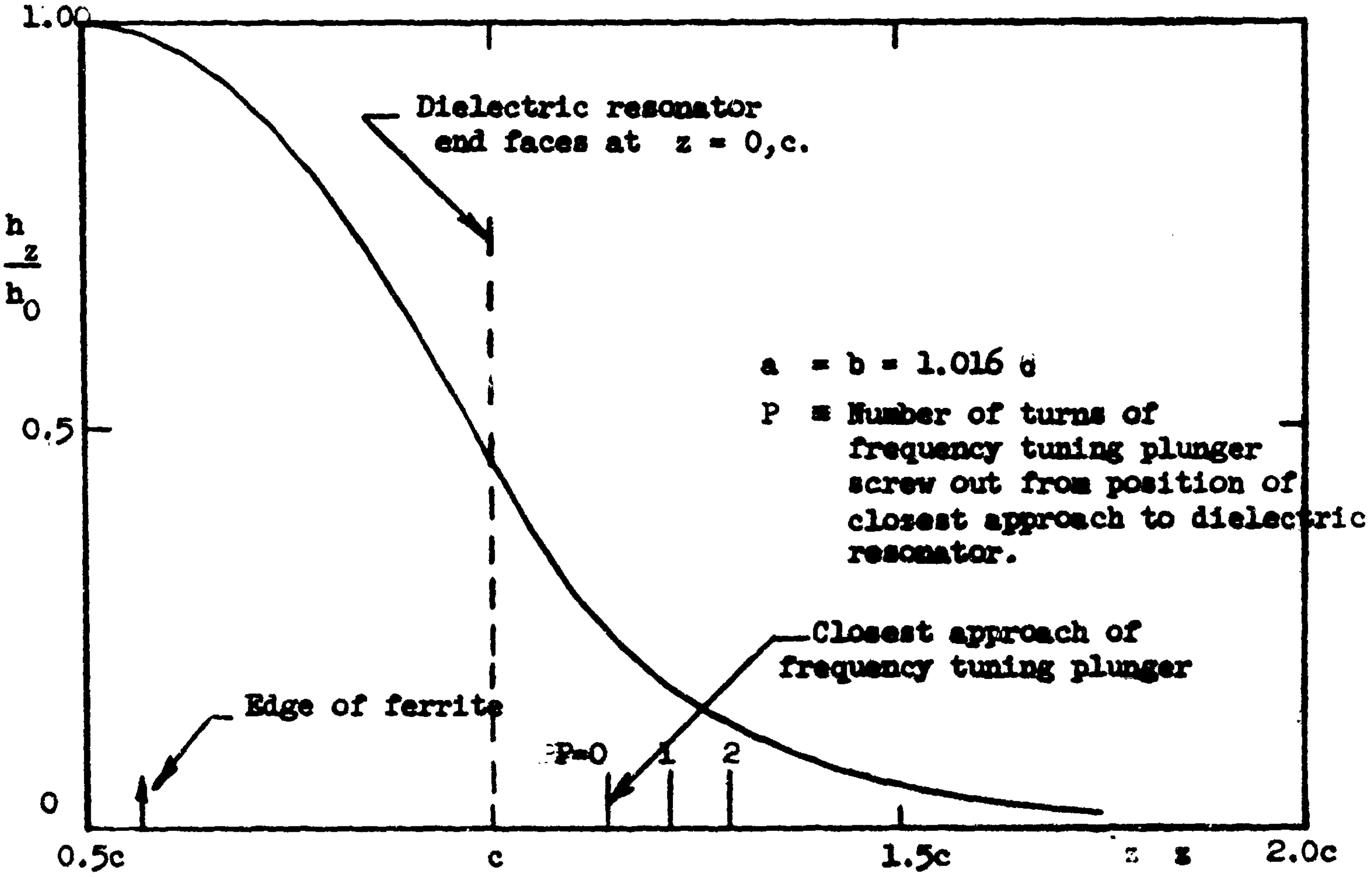

FIG. 5.4--Dielectric resonator magnetic field h_z as a function of z for $x = a/2$, $y = b/2$.

as do the electric fields given by (5.10). The importance of properly centering the ferrite sample in order to achieve maximum field strength and uniformity is obvious. The arrow indicates how far the edge of the ferrite extends when placed at the resonator center. The h_z magnetic field variation over the ferrite sample is about 1%. Thus h_0 may still be taken approximately as the average magnetic field strength over the ferrite sample volume. The transverse magnetic field at the sample edge is less than 1% of the maximum field strength. Hence, as far as field uniformity is concerned, the maximum deviation of the magnetic field lines from the z direction is somewhat less than about 0.5°.

The presence of the frequency tuning plunger causes the field to distort somewhat from the configuration described above. In particular, it causes an increase in the lateral (x-y) components of magnetic field. The diameter of the frequency plunger was almost as large as the resonator dimension a. The position of the plunger was symmetrically located parallel to the z-axis of the resonator. The distance of closest approach for the plunger of 0.06 in. is indicated in Fig. 5.4. The distance corresponding to two successive turns of the plunger screw is also indicated. The resonator was operated with $P \gtrsim 2$ to minimize distortion of the field while still being close enough to have an appreciable effect upon the resonator frequency.

In the exact solution of the fields for the spherical dielectric resonator operating in the H_{110} mode, it has been shown[29] that radiation of power from the resonator takes place. This will also occur in the rectangular resonator. As the plunger is moved closer to the resonator, a greater portion of the total solid angle is shielded against radiation by the plunger. Hence it is expected that the radiation will be reduced as the plunger becomes closer to the resonator. Such an effect was observed experimentally by an increase in the Q_0 of the resonant system. The Q_0 increased by about the same percentage whether the ferrite was present or not.

E. MEASUREMENT OF THE UNLOADED Q_0

In order to accurately evaluate the rf magnetic field strength at the ferrite during the threshold experiments it is necessary to know the unloaded Q_0 of the ferrite-loaded resonator and the variation of Q_0 with H_{dc} . The Q was measured at low power levels--far below that power level at which the instability thresholds occurred. The low power level Q's were adequate, however, since the effective resistance (or imaginary part of the magnetic susceptibility) of the ferrite does not change until loss mechanisms due to growth of elastic or spin wave instabilities are introduced. Besides, it would be much more difficult to measure the precise value of the Q at or near the high threshold power levels because average pulse heating effects would be significant, particularly if the half-power method were employed. If the sweep frequency method were employed, a wide bandwidth high power amplifier would be required.

1. Basic Relations

The relationship between the loaded Q_L , the unloaded Q_0 , and the external Q_{ext} of a resonant system is given by[30]

$$\frac{1}{Q_L} = \frac{1}{Q_0} + \frac{1}{Q_{ext}} \quad . \tag{5.17}$$

The external Q_{ext} is related to Q_0 by

$$Q_{ext} = \frac{Q_0}{\beta} \quad , \tag{5.18}$$

where β is the coupling coefficient. Thus the unloaded Q_0 may be given in terms of Q_L by

$$Q_0 = (1 + \beta)\, Q_L \quad . \tag{5.19}$$

The coupling coefficient β for an overcoupled system is given by

$$\beta = r_0 \tag{5.20a}$$

and for an undercoupled system by

$$\beta = \frac{1}{r_0} \quad , \tag{5.20b}$$

where r_0 is the VSWR on resonance and the VSWR is related to the reflection coefficient Γ by the following:

$$r = \frac{1 + |\Gamma|}{1 - |\Gamma|} \quad . \tag{5.21}$$

The external Q_{ext} given by (5.18) is a quantity dependent upon the coupling between the microwave power source and the resonant system. For a metal cavity this coupling is usually through an iris or a probe. For the dielectric resonator system the resonator is placed inside the waveguide and the coupling is adjusted by means of a movable short.

2. Q-Circle Method

Initially, an attempt was made to measure the unloaded Q_0 by the Q-circle method using instruments designed for a 1 kc square wave modulated signal. However, the time involved in measuring the VSWR and locations of the VSWR minima was sufficiently long, in spite of the low power level (~ 1 mW) of the signal generator, that dielectric heating effects distorted the results. The dielectric heating effects observed were due to the microwave power absorption of the resonator, as well as to the general ambient temperature increase between measurements. These heating effects were compensated for to some degree by taking each set of readings in an alternate sequence about the resonant frequency. Nevertheless, it was decided that other, more precise methods of determing the Q would be used in order to circumvent these heating effects.

E. MEASUREMENT OF THE UNLOADED Q_0

In order to accurately evaluate the rf magnetic field strength at the ferrite during the threshold experiments it is necessary to know the unloaded Q_0 of the ferrite-loaded resonator and the variation of Q_0 with H_{dc} . The Q was measured at low power levels--far below that power level at which the instability thresholds occurred. The low power level Q's were adequate, however, since the effective resistance (or imaginary part of the magnetic susceptibility) of the ferrite does not change until loss mechanisms due to growth of elastic or spin wave instabilities are introduced. Besides, it would be much more difficult to measure the precise value of the Q at or near the high threshold power levels because average pulse heating effects would be significant, particularly if the half-power method were employed. If the sweep frequency method were employed, a wide bandwidth high power amplifier would be required.

1. Basic Relations

The relationship between the loaded Q_L , the unloaded Q_0 , and the external Q_{ext} of a resonant system is given by[30]

$$\frac{1}{Q_L} = \frac{1}{Q_0} + \frac{1}{Q_{ext}} \quad . \tag{5.17}$$

The external Q_{ext} is related to Q_0 by

$$Q_{ext} = \frac{Q_0}{\beta} \quad , \tag{5.18}$$

where β is the coupling coefficient. Thus the unloaded Q_0 may be given in terms of Q_L by

$$Q_0 = (1 + \beta)\, Q_L \quad . \tag{5.19}$$

The coupling coefficient β for an overcoupled system is given by

$$\beta = r_0 \tag{5.20a}$$

and for an undercoupled system by

$$\beta = \frac{1}{r_0} , \tag{5.20b}$$

where r_0 is the VSWR on resonance and the VSWR is related to the reflection coefficient Γ by the following:

$$r = \frac{1 + |\Gamma|}{1 - |\Gamma|} . \tag{5.21}$$

The external Q_{ext} given by (5.18) is a quantity dependent upon the coupling between the microwave power source and the resonant system. For a metal cavity this coupling is usually through an iris or a probe. For the dielectric resonator system the resonator is placed inside the waveguide and the coupling is adjusted by means of a movable short.

2. Q-Circle Method

Initially, an attempt was made to measure the unloaded Q_0 by the Q-circle method using instruments designed for a 1 kc square wave modulated signal. However, the time involved in measuring the VSWR and locations of the VSWR minima was sufficiently long, in spite of the low power level (~ 1 mW) of the signal generator, that dielectric heating effects distorted the results. The dielectric heating effects observed were due to the microwave power absorption of the resonator, as well as to the general ambient temperature increase between measurements. These heating effects were compensated for to some degree by taking each set of readings in an alternate sequence about the resonant frequency. Nevertheless, it was decided that other, more precise methods of determing the Q would be used in order to circumvent these heating effects.

3. Sweep Frequency Method

The sweep frequency method was employed to measure the Q for experiment I. A block diagram of the experimental setup is shown in Fig. 5.5. A mechanical sweep generator was employed to drive the frequency dial of the L-band signal generator. A sweep frequency generator of the wide band, backward-wave oscillator type would have been ideal, but none was available. Since the frequency was swept over a 50 Mc range the heating effects were greatly reduced and ambient temperature drift was no longer a problem. The mechanical sweep generator provided a voltage output proportional to the angular displacement of the frequency dial. The output voltage, which was then linearly proportional to the differential frequency, was fed to the horizontal input of the oscilloscope. The vertical input of the oscilloscope came from the reflectometer, which indicated the reflection coefficient of the dielectric resonator system. A camera was utilized to take photographs of the oscilloscope trace of reflection coefficient vs frequency.

Given that Q_{ext} is constant, the type of coupling (over or undercoupled) can be determined by noting the dependence of Q_0 upon β_0 or r_0 through (5.18) and (5.20).

Another means of determining the type of coupling follows from (5.18) and (5.20), with the knowledge that the ferrite losses increase as the dc magnetic field H_0 is decreased. The type of coupling is determined by observing the change in reflected power on resonance when increased loss is introduced into the system by reducing H_0 . Thus, for an overcoupled system, increasing the loss causes the reflected power to decrease; whereas if the system is undercoupled, the reflected power will increase.

Knowing whether the signal source was over or undercoupled to the resonator system, it was possible to determine the Q of the resonator system from one of these photographs. First, the reflection coefficient Γ_0 on resonance was determined. Then the coupling coefficient β was found from (5.21) and (5.20). Knowing β , the VSWR at the half-power points was determined from a Smith chart, or by the analytical

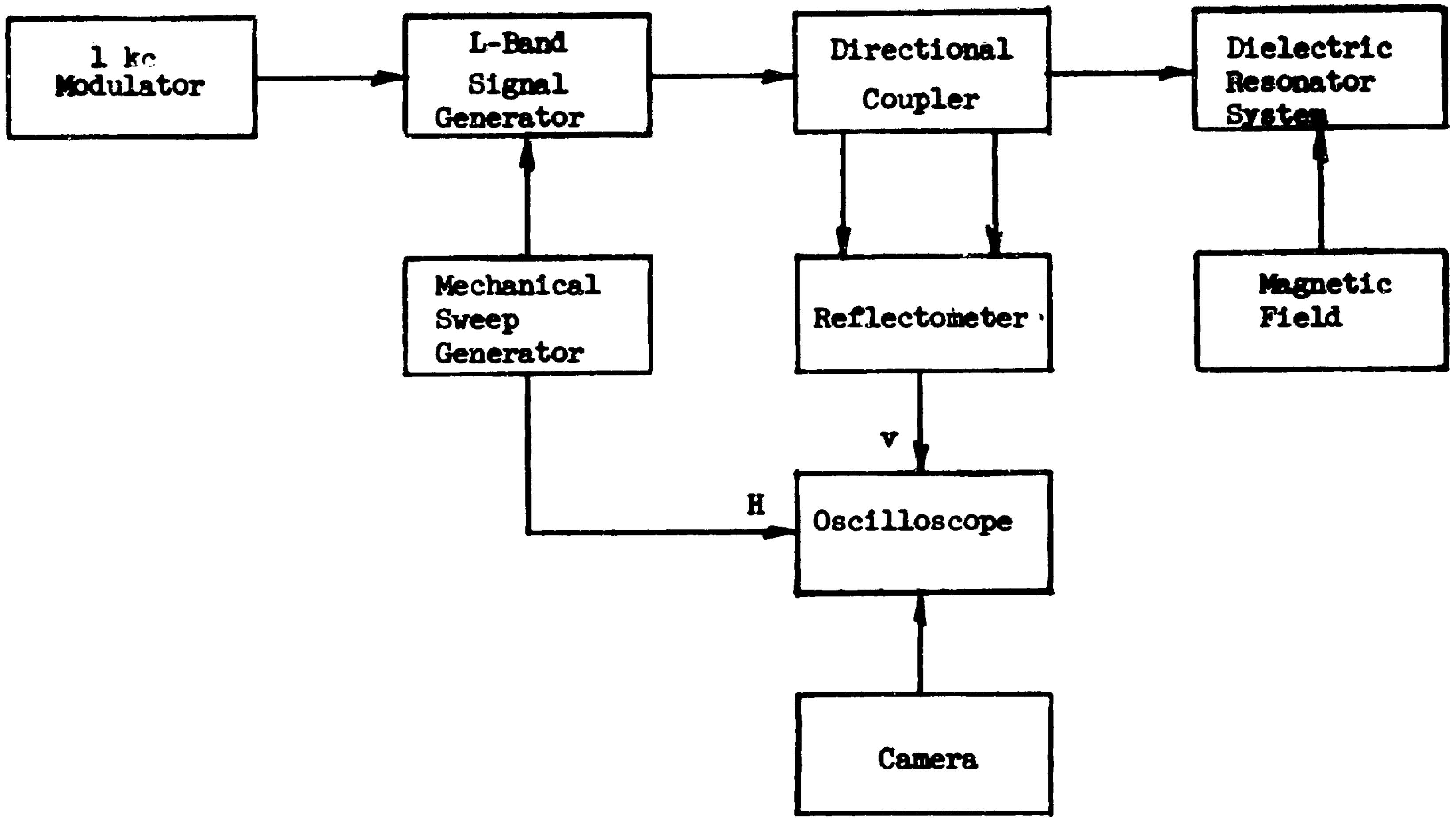

FIG. 5.5--Arrangement used in the measurement of Q_0 of the dielectric resonator system for experiment I.

expression[30]

$$\left(r_{1/2}\right)_L = \frac{\beta(1+\beta)+1+(1+\beta)\sqrt{1+\beta^2}}{\beta} \quad . \tag{5.22}$$

The reflection coefficient corresponding to (5.22) may be obtained, and the resulting frequency difference $\Delta f_{1/2}$ between half-power points may be read from the photograph's plot of reflection coefficient vs frequency. With f_0 as the resonant frequency, the loaded Q_L is defined by

$$Q_L = \frac{f_0}{\Delta f_{1/2}} \quad . \tag{5.23}$$

Finally, the unloaded Q_0 may be obtained from (5.17).

4. Half-Power Method

The half-power method was a method employed to measure the Q for experiment II. This method was used because it had greater accuracy and was much quicker than the sweep frequency method. The experimental arrangement is shown in Fig. 5.6. The pulse length of the signal was less than 2 μsec, and the repetition rate was 20 cps. The incident power level was about 10 dB or so lower than the maximum output of the signal generator (~1mW). Hence, the average power introduced into the resonator system was lower than the average power required for the sweep frequency method by a factor of at least 10^{-5}. Consequently, microwave heating effects were completely negligible. Also, any time delay between taking the data points was completely justified as long as the ambient temperature did not change appreciably during that time.

First, the frequency of the dielectric resonator system was adjusted for resonance and the value of the attenuator noted for an oscilloscope deflection of 0.1 volt. Then the system was tuned off resonance by the tuning plunger, and the attenuator reading taken for the same oscilloscope deflection. The attenuator was next set at the half-power points and

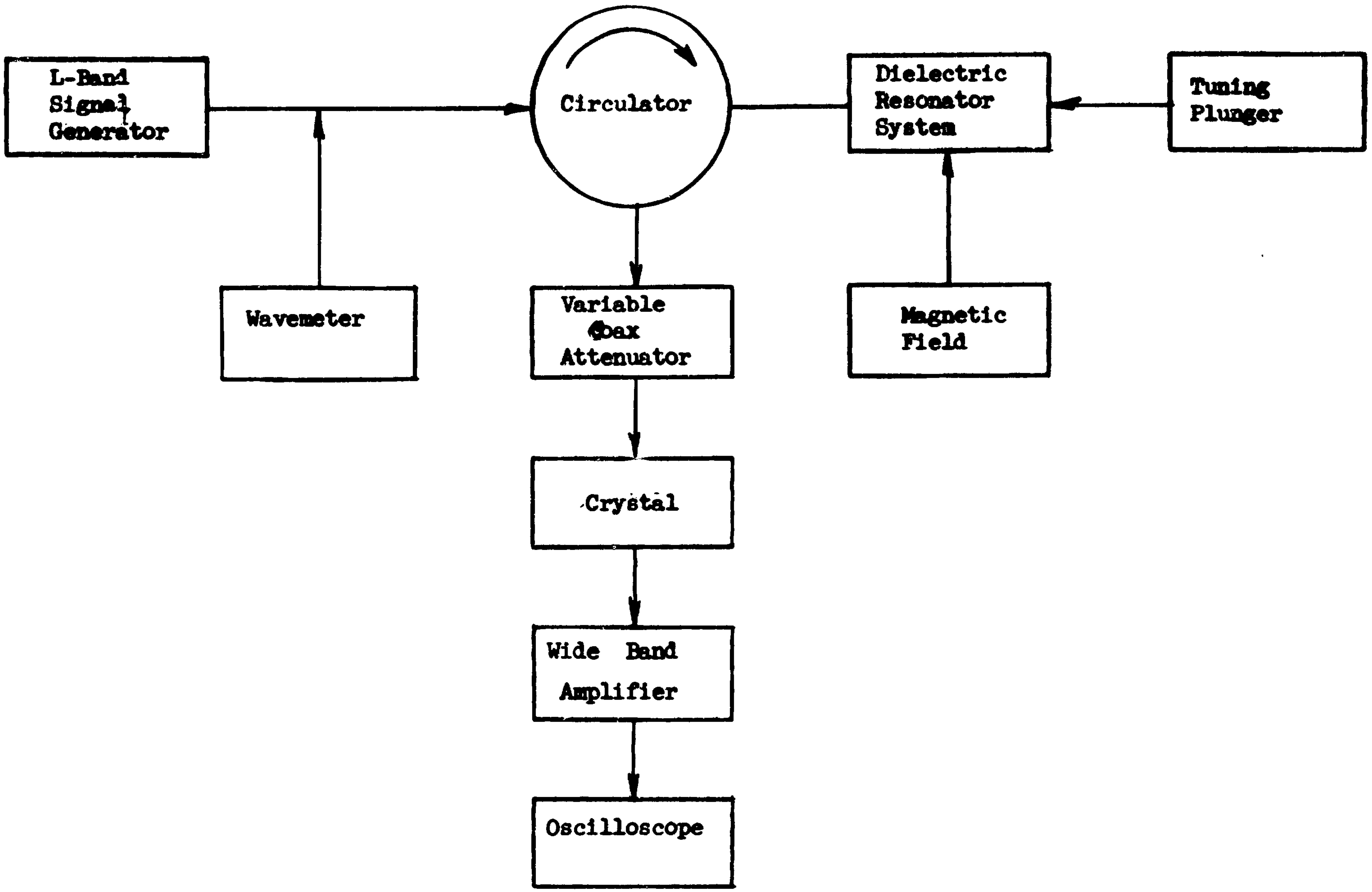

FIG. 5.6--Arrangement used in the measurement of Q_0 of the dielectric resonator system for experiment II.

the frequency measured on each side of resonance. Thus the loaded Q_L could be determined directly from (5.23). Knowing the reflection coefficient on resonance, Q_0 could then be determined from relations (5.19) through (5.21).

5. Results

The results obtained for the unloaded Q_0 as a function of the applied dc magnetic field H_0 for experiments I and II are shown in Fig. 5.7a. Normalized curves showing the approximate dependence of Q_0 upon the frequency tuning plunger position are shown in the accompanying Fig. 5.7b. Actually, these curves also depend slightly upon the magnitude of Q_0 ; i.e., the lower the Q_0 , the nearer the plunger must be to the dielectric resonator for a given relative increase in Q_0 . Nevertheless, the curves shown in Fig. 5.7b are sufficiently accurate over the range of frequency plunger positions for which threshold measurements were taken. The increase in Q_0 as the plunger is screwed inward is attributed to a reduction in the power being radiated from the resonator. The Q_0 increased by about the same percentage whether the ferrite was present or not. The deviation of Q_0 at the nearest plunger position from that at the off-resonant plunger position was not more than 15%. The position of the frequency tuning plunger had no noticeable effect upon the resonator coupling coefficient or the external Q_{ext} .

The decrease of Q_0 at increasingly low dc field values shown in Fig. 5.7a is due to the increasing proximity of the pump frequency to ferromagnetic resonance. At large dc fields the ferrite loss becomes negligible and Q_0 approaches the unloaded Q of the dielectric resonator without the ferrite, since energy storage in the ferrite is negligible compared to that of the resonator. The dashes at the far right of Fig. 5.7a indicate the measured values of Q_0 without the ferrite.

An improvement in the resonator system Q_0 from experiment I to experiment II is apparent from Figs. 5.7a,b. In the two cases the Q_0's were measured with different plunger positions, but this accounts for only about a 10% change in Q_0 . The remaining change is attributed

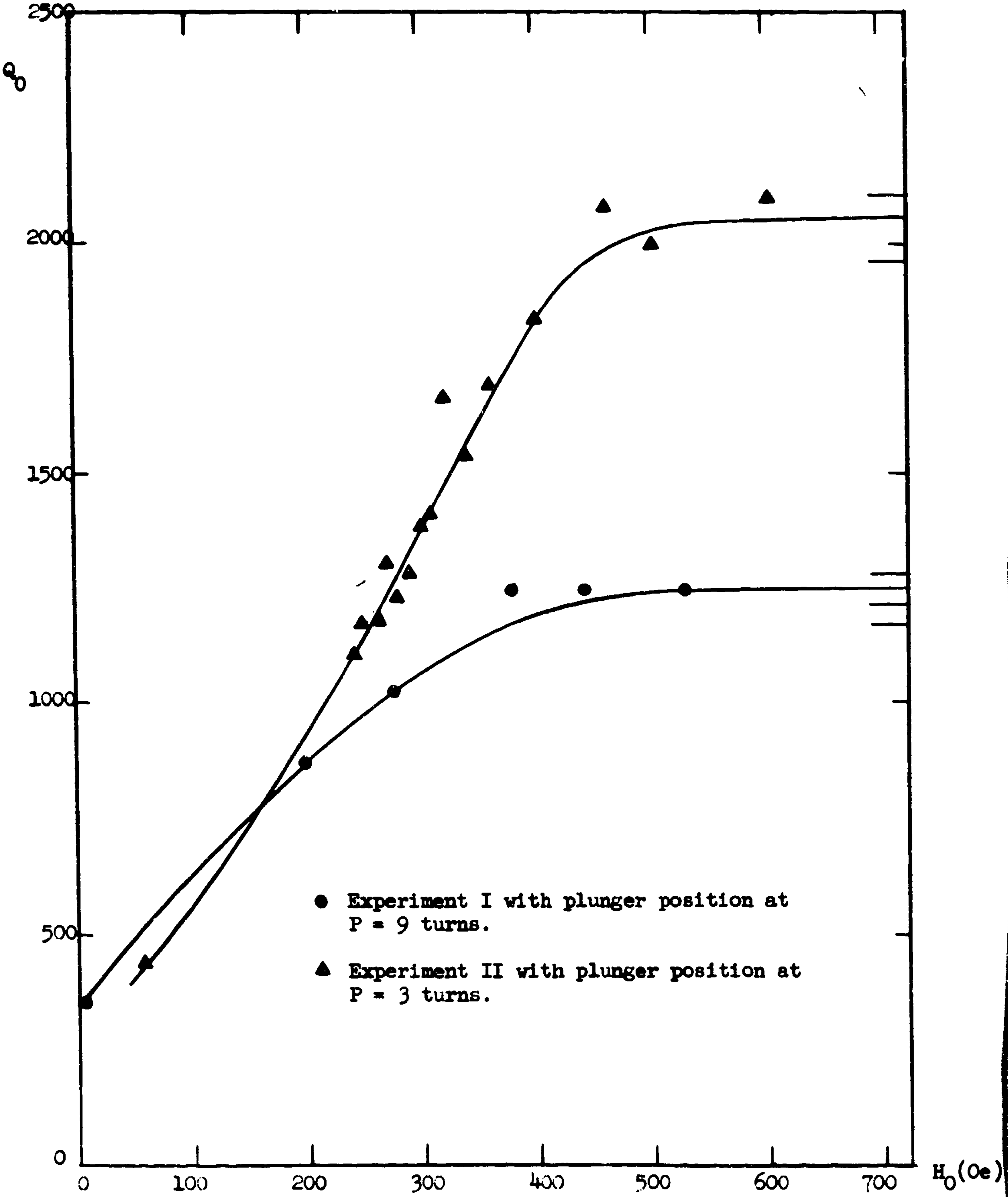

FIG. 5.7a--Unloaded Q_0 vs H_0 for experiments I and II.

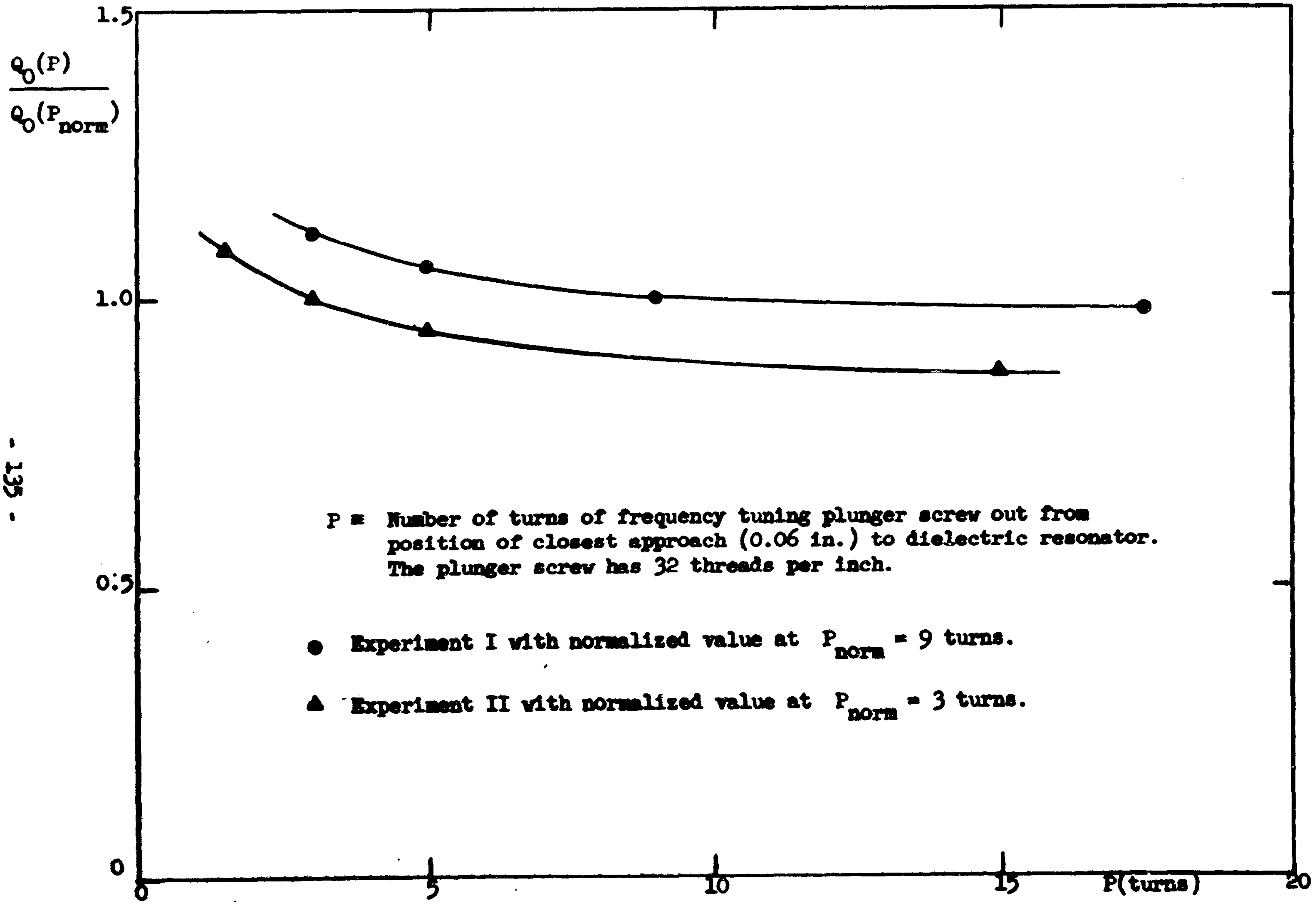

FIG. 5.7b--Normalized Q_0 vs frequency tuning plunger position for experiments I and II .

to a reduction in the amount of Ducco cement at the contact between the resonator and the supporting dielectric rod, where there was strong rf electric field, and to a thorough cleaning of the waveguide system.

No appreciable dependence of the unloaded Q_0 upon the position of the movable short was noted. However, the range of movement of the movable short to obtain proper coupling was small in both experiments.

The variation of Q_0 with temperature in the ambient temperature range was nct appreciable. This is as expected, on the basis of the small temperature dependence of $\tan \delta$ given in Appendix A. In any case, the measurements of Q_0 were taken at nearly the same ambient temperature as were the threshold measurements.

F. SUMMARY

To achieve the large rf magnetic field amplitudes required in order to reach the phonon threshold, a dielectric resonator was employed rather than a conventional cavity. With the strontium titanate dielectric resonator, the large rf field can be obtained with fairly low rf power, breakdown is avoided, and a large ferrite filling factor is obtained. The microwave power source and, in particular, the microwave circuitry associated with the modulation of the klystron beam current are described. Explanations are given for the limitations of the rf power pulse from the source. Calibration techniques for the rf power level and dc magnetic field are also discussed. Various details of the dielectric resonator system are described--including the resonant mode configuration, coupling of rf energy to the resonator, effect of temperature changes upon the resonant frequency, and microwave heating of the dielectric resonator and ferrite.

An expression for the maximum rf magnetic field amplitude (at the position of the ferrite) was derived in terms of the unloaded Q and power absorbed by the resonant system. Reliable measurements of the unloaded Q were obtained by using the sweep frequency method and the half-power method; results are given. The unloaded Q was found to vary significantly with the dc magnetic field owing to the presence of the ferrite.

CHAPTER VI

THRESHOLD MEASUREMENTS

Saturation effects have been observed in two experiments using a disk of single crystal Zn_2Y (0.054 in. diam x 0.0076 in.) cut with th easy plane lying in the plane of the disk. Actual measurements of absorbed power by the system were taken at the onset of saturation as a function of the applied dc magnetic field H_0 . The onset of saturati was determined by observing the reflected pump pulse and noting the powe level at which the growth of instabilities first became evident. There was a critical power level at which the instability threshold was reache and a transient appeared in the reflected pump pulse. Knowing the absorbed power at the threshold and the unloaded Q_0 as a function of the applied dc magnetic field H_0 , the apparent critical magnetic field amplitude (h_{ap}) at the ferrite sample was determined from (5.16).

A. EXPERIMENT I

A photograph of a typical power pulse incident upon the resonator system for experiment I is shown in Fig. 6.1a. The incident power pulse was 120 µsec long and had a time constant of about 309 µsec. The decay f the incident pulse amplitude was due to sag in the klystron beam current which discharged from a large capacitor. This time constant could be reduced by increasing the capacitor voltage; however, this caused the distortion of the pulse to increase. Therefore, a pulse was sought whic had a maximum time constant for a minimum amount of distortion. The dou e image in the photograph of Fig. 6.1a was due to ac pickup.

A typical reflected power pulse below the instability threshold is indicated in Fig. 6.1b. The time constant of this pulse, in general, wa the same as that of the incident pulse. This does not appear to be quit true in comparing Fig. 6.1b with Fig. 6.1a, because the latter was taken

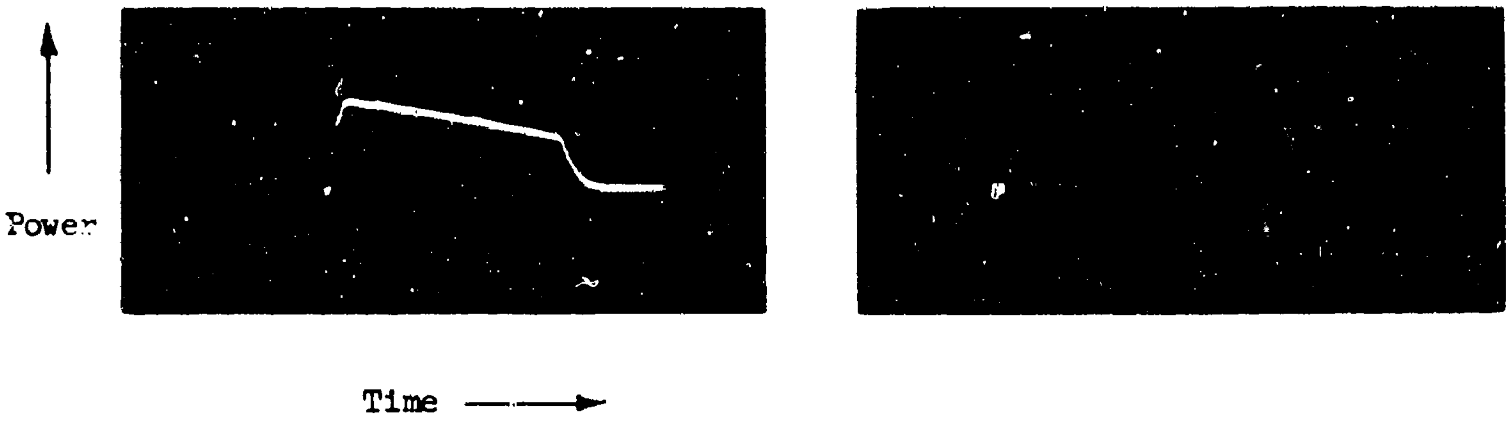

(a) Typical incident power pulse.

(b) Reflected power pulse below threshold.

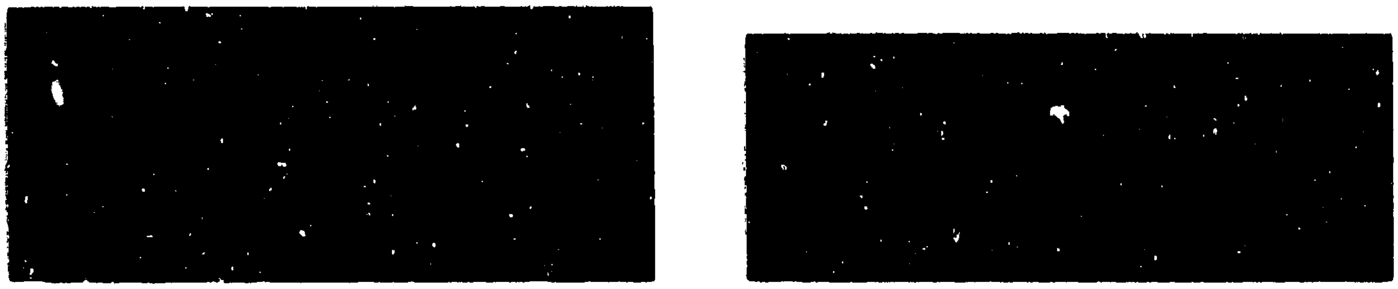

(c) Reflected power pulse just above threshold.

(d) Reflected power pulse above threshold.

(e) Reflected power pulse showing the saturation effect in the low dc field region.

FIG. 6.1--Pulse waveforms for experiment I. Time scale is 20 μsec/division.

at a slightly lower capacitor voltage. The "ear" at the end of the reflected pulse was due to frequency modulation of the microwave signal. The latter arose from the variable load which the klystron presented to the cw signal generator at the leading and trailing edges of the pulse. This effect was somewhat reduced, however, in experiment I because the reflection coefficient was high ($|\Gamma| \approx 0.3$) . The gradual decay of the ear at the trailing edge of the pulse was due mostly to the fairly high RC product of the crystal detector circuit, but was also due in part to the finite time constant of the klystron beam current switching network. Although the time constant could have been reduced by decreasing the resistance in the detector circuit, this was not done because it would have reduced the already low sensitivity of the reflected power measurements [see (4.49) on the sensitivity requirements].

Since the dielectric resonator system was overcoupled, the effect on the reflected pump pulse of an increase in ferrite absorption was to decrease the magnitude of the pulse. A typical example of a reflected pulse exhibiting the initial appearance of increased ferrite absorption is shown in Fig. 6.1c. This waveform is typical of those from which the apparent critical fields (h_{ap}) were determined. As discussed above, the threshold was found from the absorbed power level occurring at the point where absorption was first noticed. It is noted from the figure that the ferrite absorption transient builds up gradually to a peak and then decays back to the unperturbed reflected pulse amplitude. This type of behavior is very similar to that predicted by the phonon absorption theory of Chapter IV.

Figure 6.1d shows a typical reflected pump pulse at an absorbed power level above the threshold level. In this case it is noted that the ferrite absorption is greater and the pulse saturation is even more pronounced than at the threshold level. This behavior also exhibits the typical absorption behavior described in Chapter IV.

In studying the precise nature of the ferrite absorption it will be helpful to normalize the reflected pulse waveforms of Figs. 6.1c,d to an arbitrary level below threshold (Fig. 6.1b). The results of doing this are shown in Fig. 6.2. These waveforms showing ferrite absorption are similar to those predicted in Chapter IV for phonon absorption in the ferrite. In particular, the normalized theoretical waveforms of Fig. 4.8

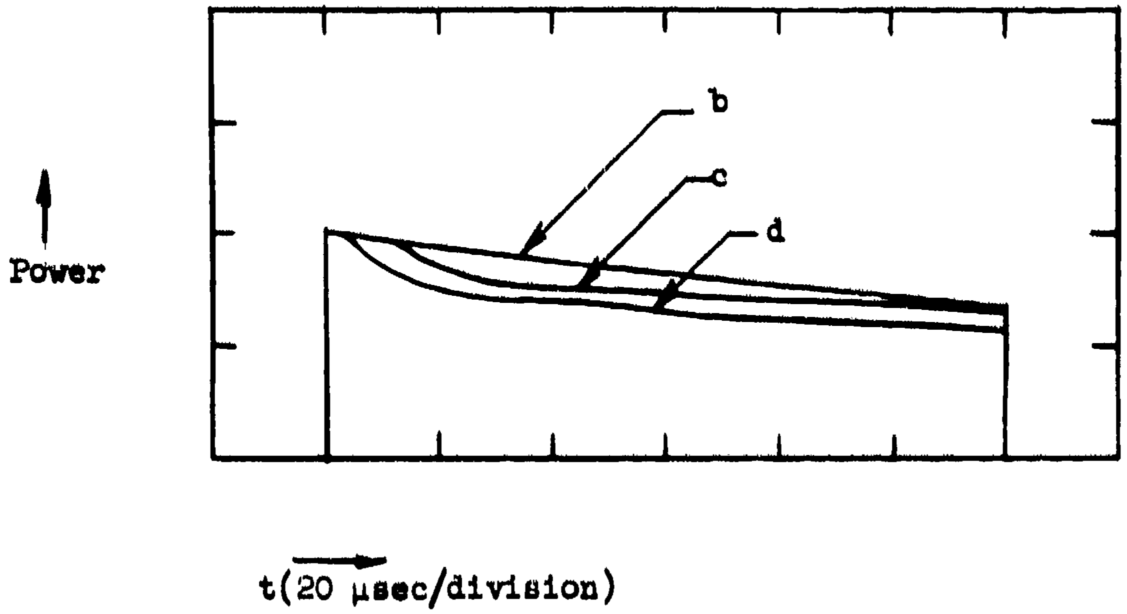

FIG. 6.2--Drawing of reflected power waveforms of Figs. 6.1b,c,d normalized to the level corresponding to 6.1b.

are comparable to the normalized experimental waveforms of Fig. 6.2.(1) Figure. 4.8a is comparable to Fig. 6.2b, the reflected power waveform before the onset of saturation; and Fig. 4.8b is comparable to Fig. 6.2c, the reflected power waveform when the phonon absorption first appears. In each case, the absorption during the pulse builds up to a peak and then decays gradually. It is seen that the waveforms above threshold power levels (Figs. 4.8c and 6.2d) are also similar in nature. Again, the absorption builds up to a peak and decays. In both theory and experiment the absorption peak increases with increasing power levels.

The first exception to the theory occurs in the magnitude of the build-up time t_{ap} . The experimental value observed from Fig. 6.2c is

$$(t_{ap})_{exp} = 32\ \mu\text{sec} \quad , \tag{6.1}$$

which is much shorter than the predicted value of $t_{ap} = 104\ \mu\text{sec}$ for experiment I, based upon a phonon Q_p of 1500. If the linear theory worked out in Chapter IV is correct, then the shorter observed build-up time simply implies that the phonon Q_p is actually much lower than 1500. In fact, it was shown in Chapter IV for $(t_{ap})_{exp} = 32\ \mu\text{sec}$ that a Q_p of 129 was obtained from the linear theory. It might be sufficient to accept this lower value of Q_p as the actual value except for what happens to the reflected pulse waveform at higher pump power levels. From Figs. 6.2c,d the build-up time is seen to decrease with the increasing power level. This is contrary to the behavior predicted by (4.67), where t_{ap} was expected to increase with increasing power levels, and might be explained on the basis of a variation of Q_p with the amplitude of the unstable phonon as was suggested in Chapter IV. In any case, it is clear that the experiment does not provide a reliable measured value of Q_p .

---

(1) Although the curves of Fig. 4.8 were calculated for the values of experiment II, it is clear from the equations of Chapter IV that the shape of the curves describing the phonon absorption would be the same for experiment I. Since Γ is much larger for experiment I than for experiment II, however, the effect of phonon absorption would be proportionally less for experiment I.

The above discussion relates the observed saturation threshold behavior at the higher dc magnetic fields to the phonon saturation theory of Chapter IV. At the lower dc magnetic fields, quite different threshold observations were made. A typical reflected pump pulse in the low dc field region is shown in Fig. 6.1e. Here the threshold is defined by the appearance of the small ripples shown in the figure. This type of threshold is attributed to the presence of spin wave instabilities, which apparently dominate the phonon instabilities.

Measurements of absorbed power were taken as a function of the external magnetic field H_0 at the threshold levels corresponding to Figs. 6.1c and 6.1e. Apparent critical fields were obtained from these measurements and are plotted in Fig. 6.3. The two typical experimental runs shown were taken with increasing H_0. These runs were also typical of runs taken with decreasing H_0. In order to verify the continuous nature of the threshold curve, the experimental points for the second run were taken at the smallest increments of H_0 possible with the magnetic field current supply used in experiment I. This run also gives a good indication of the experimental error to be expected in the reproducibility of such measurements.

The ambient temperature was slightly different for the two runs indicated. This implies a possible greater disparity in the temperature of the ferrite itself for the two runs. In accordance with results from the previous chapter, the temperature of the ferrite depends chiefly upon the length of time it is exposed to a given microwave field. It is evident that the apparent effect of slight temperature deviations on the thresholds from one run to another was not appreciable and is within experimental error. However, for both runs it is expected on the basis of the analysis of Chapter V that at the higher power levels there will be some shift toward lower H_0 values due to the dependence of the demagnetizing field upon temperature. In fact, using the 10°C temperature change estimated for $P_a = 10$ W, a downward shift of 8 Oe would be expected at $H_0 = 365$ Oe.

The relationship between the apparent theoretical threshold h_{ap} for the actual pulse and the threshold h_{cr} for an ideal pulse was

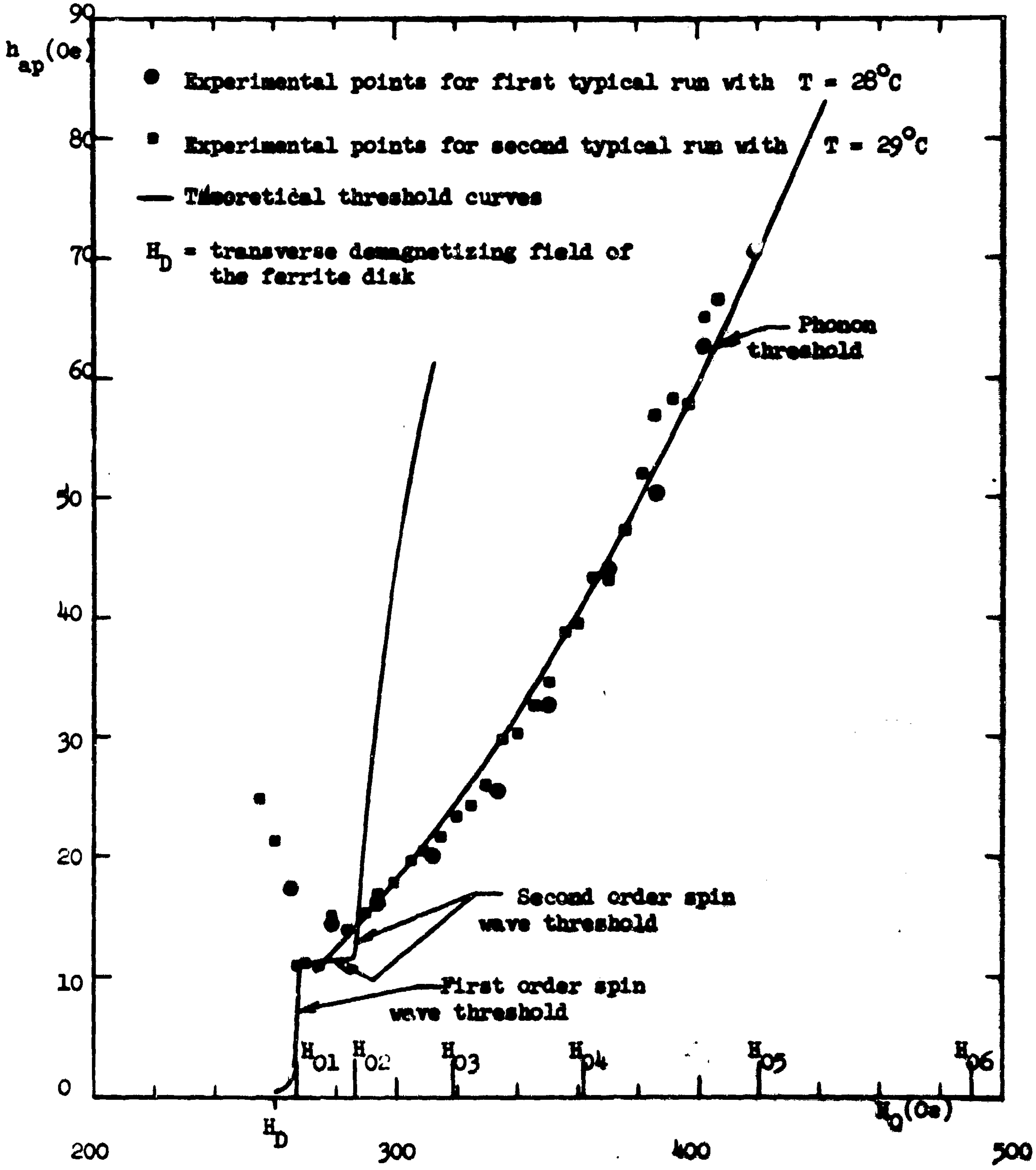

FIG. 6.3--Experimental and theoretical values of h_{ap} vs H_0 (external field) for the Zn_2Y disk in transverse pumping experiment I.

determined in Chapter IV. This ratio h_{ap}/h_{cr} is only approximately constant over the range of field H_0 for which the experimental thresholds of Fig. 6.3 were taken. The only significant change in this ratio takes place through variation in the phonon absorption peak $(P_p)_{ap}$. Recall the relation (4.61) which relates P_p to the reflection coefficient Γ and the change in reflected power ΔP_r . Using this relation, it was found from the experimental results that $(P_p)_{ap}$ changes by a factor of 50:1 , increasing monotonically as H_0 increases. The effect of this change in the observed phonon absorption peak upon the ratio h_{ap}/h_{cr} about a mean value is less than 0.2% for the parameter values associated with (4.66), for the effective $Q_p = 127$ and the observed build-up time. Thus, the ratio h_{ap}/h_{cr} is, indeed, a constant for all practical purposes, and the above assumption is thereby justified.

The dominant theoretical phonon threshold for an ideal pulse, given by (3.52), may be written

$$(A_p)_{cr} = \frac{h_{cr}}{H_0} = \frac{K_p \, x'^{3/2}}{1 + 4.67\, x'} \quad , \qquad (6.2).$$

where

$$K_p = \frac{2C_{\xi\xi\eta\eta}(4\pi M_s)^2}{3\pi\sqrt{3}\, Q_p\, B_3^2}$$

and it is recalled that

$$x' = x + d \quad ,$$

where

$$x = \frac{H}{4\pi M_s} = \frac{H_0}{4\pi M_s} - N_{\parallel}$$

and

$$d = \frac{Dk^2}{4\pi M_s} = \frac{H_{ex\parallel}\, a^2 k^2}{4\pi M_s} \quad .$$

The apparent threshold will then be given by

$$(A_p)_{ap} = \frac{h_{ap}}{H_0} = \frac{h_{ap}}{h_{cr}} (A_p)_{cr} = \frac{\frac{h_{ap}}{h_{cr}} K_p \, x'^{3/2}}{1 + 4.67\, x'} \quad , \qquad (6.3)$$

where the parameters are defined as above. Since the ratio h_{ap}/h_{cr} is very nearly independent of H_0, as explained above, Eq. (6.3) was fitted to Fig. 6.3 by adjusting the parameters $(h_{ap}/h_{cr})K_p$ and d . It was found that the best fit was obtained with

$$\frac{h_{ap}}{h_{cr}} K_p = 9.68 \qquad (6.4a)$$

and

$$d = 0.022 \quad . \qquad (6.4b)$$

Expression (6.3) is plotted with these parameter values in Fig. 6.3, where it is seen that experimental points fit the theoretical curve quite closely.

From the value of d given by (6.4b), it is found that

$$H_{ex\parallel} a^2 k^2 = 58 \text{ Oe} \quad .$$

Knowing the lattice constant a , and the value of k for the unstable elastic wave mode [determined from (3.28b) and (3.57)], the exchange field in the easy plane $H_{ex\parallel}$ becomes

$$H_{ex\parallel} = 12.3 \times 10^7 \text{Oe} \quad . \qquad (6.5)$$

From the above value of $(h_{ap}/h_{cr})\, K_p$ given by (6.4a) and the theoretical value of $h_{ap}/h_{cr} = 1.003$ for experiment I given by (4.66), the value of K_p obtained is 9.65. This value is somewhat larger than the value of $K_p = 7.74$ estimated in Chapter III and given in (3.60). The latter was based upon the estimates of $Q_p = 1500$ and $B_3 = 5 \times 10^6$ erg/cm^3. Taking instead the effective value of $Q_p = 127$ given by (4.66) and the same values of $C_{\xi\xi\eta\eta}$ and $4\pi M_s$ employed originally, a new estimate may be obtained for B_3. From the expression for K_p given in (6.2), the following value for B_3 is obtained:

$$B_3 = 1.54 \times 10^7 \text{ erg/cm}^3 \quad . \tag{6.6}$$

Thus it appears that the magnetoelastic constants for Zn_2Y are larger than they are for YIG ($B \approx 5 \times 10^6$ erg/cm^3).

With the parameters given in (6.4) the theoretical threshold expression (6.3) fits the experimental points of Fig. 6.3 well. There are, however, two minor considerations which should be pointed out. The first one, which has already been described, is the effect of microwave heating on the saturated magnetization and hence upon the applied dc magnetic field required to sustain a given internal field. This effect explains the deviation of the experimental points above the theoretical curve at the higher threshold levels shown in Fig. 6.3. Since the effect of microwave heating at the higher thresholds decreases the demagnetizing field, the theoretical curve shown in Fig. 6.3 more closely approximates a curve of experimental points taken at the same ferrite temperature, rather than one of points taken at the same ambient temperature. The second consideration has to do with deviation of the theoretical threshold from that shown in Fig. 6.3 for the lower H_0 values. In deriving the transverse phonon thresholds the assumption was made that $\omega_p^2 \ll \omega_m^2$. As was mentioned in Chapter III, this condition is fulfilled very well with dc fields above H_{03} where $\omega_p^2 \lesssim 0.1\, \omega_m^2$. However, in the transition range, $H_{02} < H_0 < H_{03}$, the theoretical phonon threshold is somewhat lower than indicated in Fig. 6.3. If both of the above effects are taken into account in the interpretation of the experimental points and theoretical curve of Fig. 6.3, it is expected that slightly different values for the exchange constant d and the multiplicative constant K_p would be obtained. However, the corrections which might be made would be within experimental error of the points of Fig. 6.3.

At dc fields $H_0 \sim H_{02}$ in Fig. 6.3 the reflected power waveforms exhibited a different kind of saturation effect. This is attributed to the growth of spin wave instabilities. The spin wave thresholds for an ideal pulse were plotted as a function of internal dc field in Figure 2.3. These are related to the critical field h_{cr} by the familiar definition

$$(A_p)_{cr} = \frac{h_{cr}}{H_0} \quad . \tag{6.7}$$

For the actual pump pulse the apparent threshold is

$$(A_p)_{ap} = \frac{h_{ap}}{h_{cr}} (A_p)_{cr} \quad . \tag{6.8}$$

It will now be assumed that h_{ap}/h_{cr} is a constant, independent of H_0, and that this constant is approximately unity. This assumption is reasonable in view of the results for the build-up of phonon instabilities (Chapter IV). Then the apparent spin wave thresholds are given approximately by Fig. 2.3, where the spin wave Q has been assumed to be ≈ 193. A comparison of the theoretical curves of Fig. 2.3 with the experimental points of Fig. 6.3 shows that the experimental thresholds are larger. It is tentatively deduced from this that the spin wave Q is lower than 193. By matching the theoretical on-resonance second order threshold curve (2.50) to the level established by the three data points near $H_0 = 270$ Oe, an estimate $Q \approx 23.4$, is obtained for the effective spin wave Q. Using this value of Q, theoretical values of the first and second order spin wave thresholds have been plotted in Fig. 6.3. It is seen that the lowest threshold changes from spin wave to phonon at $H_0 \approx H_{02}$. The second order off-resonance spin wave threshold is seen to increase very steeply above $H_0 = H_{02}$, and is the dominant theoretical threshold only over a negligibly small range of H_0 .

At further reduced magnetic fields, $H_0 < H_{01}$, the experimental thresholds are seen to increase rapidly--in a region where the very low first order threshold is expected to be dominant. The explanation for this probably lies in the fact that in this region the internal dc magnetic field is insufficiently large to saturate the magnetization of the ferrite. Thus the magnetization no longer is uniform throughout the sample volume, and additional magnetic relaxation processes may be operating.

B. EXPERIMENT II

This experiment, similar to experiment I, was undertaken to observe in greater detail the more exact nature of the saturation effects on the reflected pump pulse. The magnet used for this second experiment had a more uniform, better regulated, and larger range of magnetic field than did the one employed in experiment I. The magnetic field was sufficiently uniform for it to be measured directly with the NMR probe. The larger range of the magnetic field H_0 allowed measurement of thresholds corresponding to the maximum power output of the signal generator. This made it possible to pass through H_{05} the maximum field at which the fifth order spin wave instability would be permitted on resonance.

Also, in this experiment the level at which the reflected power could be detected was 20 dB lower than in experiment I, permitting a reduction in the reflection coefficient Γ of the resonant system; and the unloaded Q_0 of the dielectric resonator system was higher than it was for experiment I, with the result that the incident power level P_i was reduced. The effects of lower Γ and P_i on the relative change in reflected power $\Delta P_r/P_r$ due to a given change in ferrite absorption are seen by an examination of (4.49). This shows that ΔP_r is increased; the saturation effects can therefore be observed in greater detail. In this experiment much better photographs of saturation phenomena on the reflected pulse were, in fact, obtained.

A photograph of a typical klystron beam current pulse, as seen at the output of a current pulse transformer, is shown in the top half of

Fig. 6.4a. Some indication of the sag in the current discharging from the high voltage capacitor in the klystron modulator is evident in the first 30 μsec. The increased sag beyond 30 μsec is due to sag inherent in the current transformer as well as in the beam current. The amplified rf power pulse at the output of the klystron detected at the directional coupler is shown in the bottom half of Fig. 6.4a. The pulse was 90 μsec in duration and had a time constant of about 124 μsec. This pulse has a shorter length and a smaller time constant than the incident pulse of experiment I because there was an equipment failure and unavoidable alterations had to be made in the klystron modulator. For each experiment a pulse of maximum time constant was, of course, sought.

A typical reflected power pulse below the instability threshold is indicated in Fig. 6.4b. The ears on the reflected pulse, due to the frequency modulation described previously, are more pronounced than they were for experiment I because the reflection coefficient is much smaller ($|\Gamma| \approx 0.08$). The time constant of the ears is smaller than for experiment I because the resistance in the crystal detector circuit was decreased. It was possible to decrease the resistance for experiment II because the sensitivity (or the relative change in reflected power) was greater, for reasons mentioned above.

In this experiment the dielectric resonator system was again overcoupled. Thus the effect of an increase in ferrite absorption was to decrease the magnitude of the reflected pump pulse. A typical example of a reflected pulse exhibiting the initial appearance of ferrite absorption is shown in Fig. 6.4c. This waveform is typical of those from which the apparent critical fields (h_{ap}) were determined. It is apparent that the ferrite absorption gradually builds up to a peak and then decays as in experiment I. However, in experiment II the initial appearance of the absorption peak is more clearly seen, and the similarity to the waveform predicted by the theory of Chapter IV is even more marked.

Figure 6.4d shows a typical reflected pump pulse at an absorbed power level above threshold. The increase in ferrite absorption is apparent. At a still higher level above threshold, the reflected pump pulse appears as shown in Fig. 6.4e. Here the absorption peak appears

(a) Klystron beam current and rf output power waveforms.

(b) Typical reflected power pulse below threshold.

(c) Reflected power pulse at threshold.

(d) Reflected power pulse above threshold.

(e) Reflected power pulse much above threshold.

FIG. 6.4--Pulse waveforms for experiment II.

slightly truncated--indicating the presence, possibly, of pulse saturation due to the change in Γ , as described in Chapter IV. When the changes in reflected power become as large as those shown in Fig. 6.4e, this effect should be appreciable. If the ferrite absorption increases much more than that indicated in Fig. 6.4e, the reflection coefficient will "go through zero" at the absorption peak and the dielectric resonator system will become undercoupled.

In studying the precise nature of the ferrite absorption it is again helpful to normalize the reflected pulse waveforms of Figs. 6.4b-e to an arbitrary level below saturation. The results of the normalization are shown in Fig. 6.5. These waveforms showing ferrite absorption are similar to those shown in Fig. 4.8 for the theoretical phonon absorption based upon the parameters of experiment II. In particular, it is noted that the predicted waveforms of Figs. 4.8a-c correspond with the observed waveforms of Figs. 6.5b-d. In both theory and experiment the absorption peak increases with increasing power levels above threshold. The shape of the absorption is approximately the same in each case. There appear, however, to be the same deviations from the theory as were observed in experiment I.

The first exception to the theory occurs in the magnitude of the build-up time t_{ap} . The experimental value observed from Fig. 6.5c is

$$(t_{ap})_{exp} = 28\ \mu\text{sec} \quad ,$$

which is shorter than the predicted value of $t_{ap} = 60\ \mu\text{sec}$ for experiment II, based upon a phonon Q_p of 1500 . It is noteworthy, though, that the experimental value of t_{ap} is closer to the predicted value for the parameters of experiment II than for those of experiment I. This, as will be discussed below, is attributed to the lower ferrite absorption level of experiment II. From the linear theory of Chapter IV it may be concluded that the shorter observed build-up time implies that the phonon Q_p is actually much lower than 1500. In fact it was shown in Chapter IV that a Q_p of 294 was obtained for the linear theory for $(t_{ap})_{exp} = 28\ \mu\text{sec}$. As explained previously, this value of Q_p may probably be regarded as an effective value which can be considered as decreasing with increasing

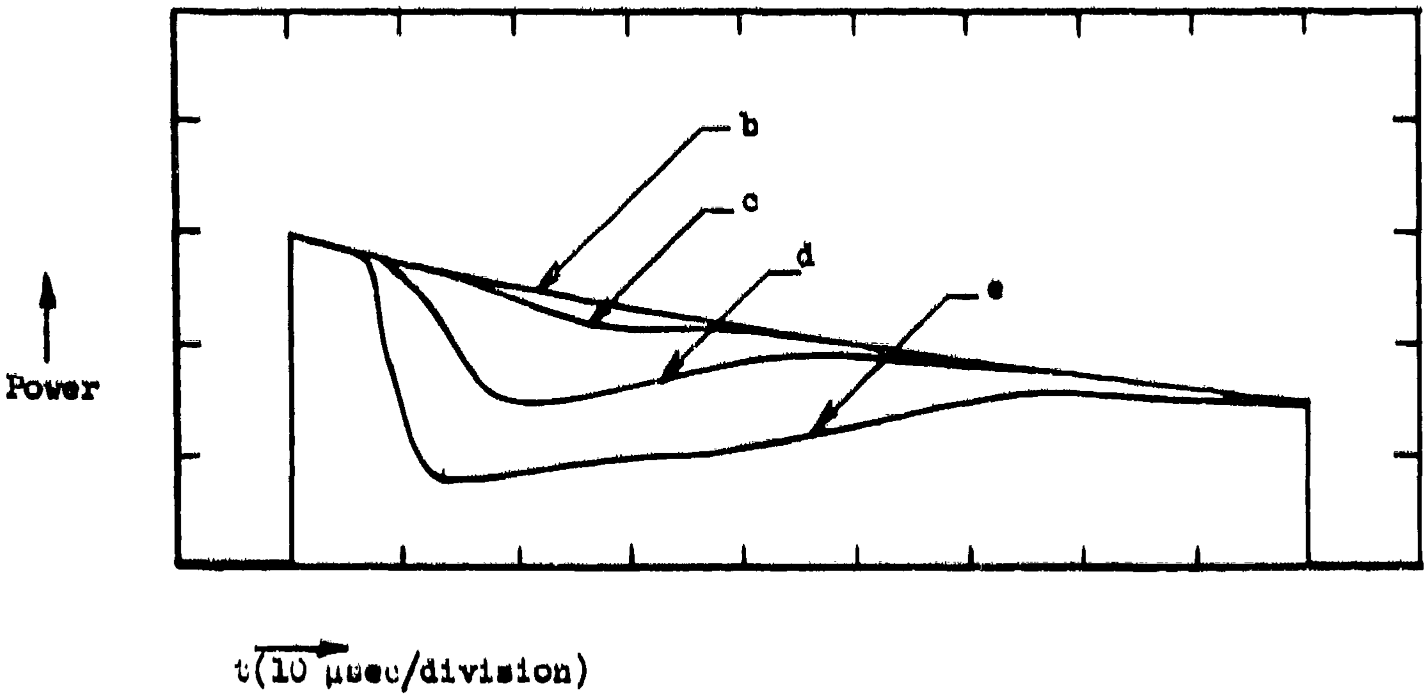

FIG. 6.5--Drawing of reflected power waveforms of Figs. 6.1b,c,d normalized to the level corresponding to 6.1b.

phonon amplitude. Thus the phonon damping is considered nonlinear. By this interpretation of the results, it is possible to explain the decrease in the observed build-up time t_{ap} with increasing absorption levels, which can be clearly seen in Fig. 6.5.

The above discussion correlates the observed instability thresholds at the higher dc magnetic fields with the theory of Chapter IV. At the lower dc magnetic fields, quite different threshold observations were made. In this experiment several different kinds of saturation effects were observed for $H_0 \gtrsim H_{02}$. A typical example of the reflected power waveform taken in this region is shown in Fig. 6.6a. The dc field of $H_0 = 300\ O_e$ for these waveforms is within 14 Oe of H_{02}. Each successively higher waveform in the photograph occurs for a higher incident power level, and hence a higher field strength at the ferrite. The lowest trace in the photograph shows a slight evidence of ripples at the lowest power level. At a slightly higher power level the ripples show their somewhat random nature and their amplitudes increase. The third waveform shows superimposed upon the random ripples the appearance of the absorption peak associated with the phonon theory. At the highest power waveform indicated in the photograph, the ripples are clearly dominated by the phonon-like behavior. At dc fields higher than 300 Oe the amplitude of the small random ripples became less and less, until at about $H_0 = 360$ Oe they vanished completely. At fields less than 300 Oe the amplitude of the ripples became larger, but they were still dominated by the phonon absorption dip described above until the point $H_0 = H_{02}$ was reached. For $H_0 < H_{02}$ random ripples, similar to those described above, appeared quite suddenly at a critical power level. This is believed to define the second order spin wave threshold. For $H_0 > H_{02}$ the appearance of the absorption dip is believed to define the phonon threshold, even when random ripples are superimposed. The reason for the superposition of the two patterns, suggesting concurrent spin wave and phonon instabilities, is not known.

For $H_0 < H_{01}$ another kind of saturation effect was observed. This is shown in Fig. 6.6b, for which $H_0 = 263$ Oe . There was a threshold, marked by the sudden appearance of relaxation oscillations in the form

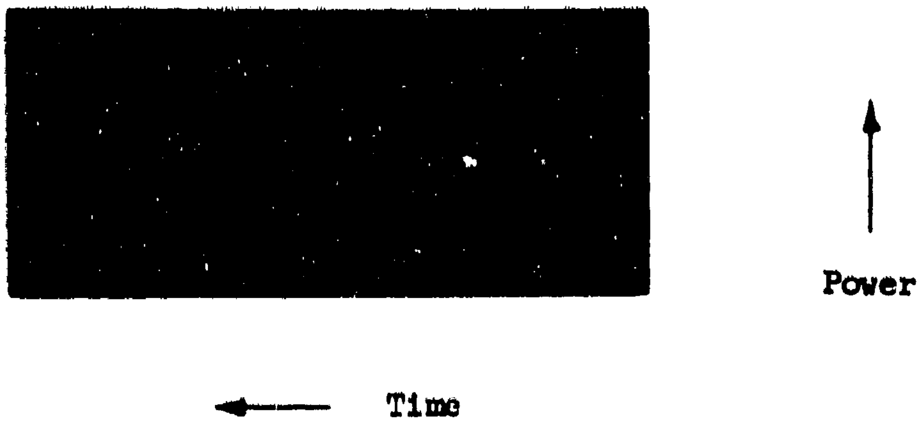

(a) Saturation effects for H_0 slightly greater than H_{02}.

(b) Saturation effects for H_0 less than H_{01}.

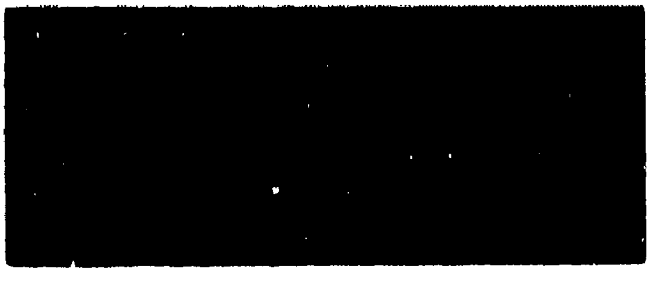

(c) Saturation effects for H_0 slightly less than H_{01}.

FIG. 6.6--Reflected power pulse waveforms showing various saturation effects observed in experiment II. Time scale is 10 μsec/division.

of an attenuated sinusoid. One reason for the attenuation was, of course, that the incident power decreased during the pulse and eventually reached a level below the threshold. This waveform was reproducible and had a relaxation frequency of about 250 kc.(1) This effect was observed only at dc field values between H_D and H_{01}, and is attributed to the first order resonant spin wave instability. For the slightly higher dc field $H_0 = 265$ Oe a similar behavior was observed, as is shown in the top waveform of Fig. 6.6c. In this case, however, as the power level was increased the waveform shown in the bottom of Fig. 6.6c was observed. Here the attenuated sinusoid broke up into somewhat random oscillations as the power was increased further. This effect is not understood.

Measurements of absorbed power were taken as a function of the applied magnetic field H_0 at the threshold level for each type of ferrite absorption. Apparent critical fields were obtained from these measurements and are plotted in Fig. 6.7. Proceeding as before with expressions (6.2) and (6.3), a "best fit" of the theoretical phonon threshold curve to the experimental points of Fig. 6.7 is obtained with

$$\frac{h_{ap}}{h_{cr}} K_p = 10.35 \qquad (6.9a)$$

$$d = 0.022 \quad . \qquad (6.9b)$$

Expression (6.3) is plotted with these parameter values in Fig. 6.7, where it is seen that the experimental points fit the theoretical curve closely. The value of d in (6.9b) is the same as was obtained from the threshold curve for experiment I. Thus the calculated exchange field is the same as before, equation (6.5).

From the value of $(h_{ap}/h_{cr})K_p$ given by (6.9a) and the theoretical value of $h_{ap}/h_{cr} = 0.961$ for experiment II, given by (4.79), the value

---

(1) Such relaxation oscillations have frequently been observed in parallel pump experiments. They are not completely understood.

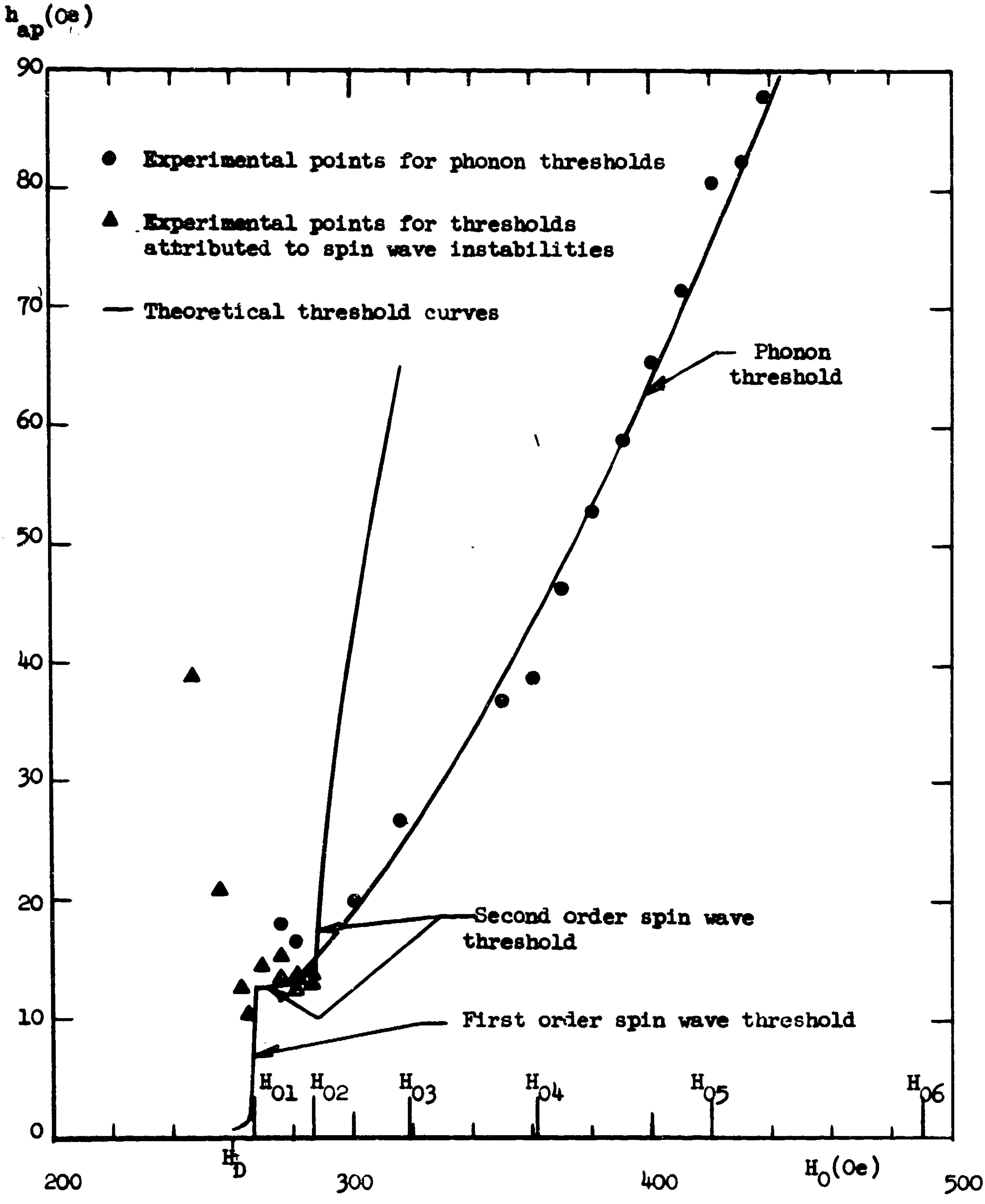

FIG. 6.7--Experimental and theoretical values of h_{ap} vs H_0 for the Zn_2Y disk in transverse pumping experiment II.

of K_p obtained is

$$K_p = 10.77 \quad ,$$

which is comparable to the value of K_p obtained for the first experiment. Again, taking the above value of K_p , the effective value of $Q_p = 294$ given by (4.67) and the same values of $C_{\xi\xi\eta\eta}$ and $4\pi M_s$ used originally, the following estimate for B_3 is obtained:

$$B_3 = 0.959 \times 10^7 \text{ erg/cm}^3 \quad . \qquad (6.10)$$

This result is comparable to the result (6.6) for experiment I.

As in experiment I, the thresholds attributed to the second order spin wave instability may be fitted to the theory by assuming a spin wave Q given by $Q \approx 18.0$, and the theoretical first and second order thresholds are plotted in Fig. 6.7, assuming this value of Q . The results are comparable with those of experiment I.

C. SUMMARY AND CONCLUSIONS

Two experiments were performed using a disk of single crystal Zn_2Y cut with the easy plane lying in the plane of the disk. In each experiment the apparent critical magnetic field was found to be a function of the applied dc magnetic field. The instability threshold (or critical field) was determined by the absorption peak in the reflected pump pulse. Photographs of the incident and reflected power pulse waveforms are shown and irregularities in the waveforms due to the nature of the power source are explained. Irregularities on the reflected pulse waveforms due to the growth of ferrite instabilities are discussed in detail.

In the dc magnetic field region where phonon instabilities were expected to be dominant, the shape of the ferrite absorption on the reflected pump pulse was nearly the same as that predicted by the phonon absorption theory of Chapter IV. The observation of instability thresholds was found to be approximately as predicted by the theoretical spin wave and elastic wave threshold calculations of Chapters II and III. At applied dc magnetic fields above the point where the seond order spin wave threshold becomes off-resonant, the experimental threshold fields were found to exhibit the same functional dependence upon dc field as the theoretical phonon threshold curve. From this curve an estimate was obtained for the exchange field $H_{ex\parallel}$ of Zn_2Y in the easy plane. This functional dependence strongly indicates that the magnetoelastic effect is the dominant mechanism and that the observed thresholds were due to growth of unstable elastic waves propagating and polarized in the easy plane. At applied dc magnetic fields below the point where the second order spin wave threshold becomes off-resonant, the experimental threshold fields were found to exhibit qualitatively the same dependence upon dc field as the theoretical first and second order spin wave threshold curves, with some exceptions.

Explanations for these exceptions are suggested but more work must be done in order to understand the precise nature of these instabilities, and it should probably be done with ideal pulses. In the phonon threshold case, however, the use of actual pulses permitted the determination of both the magnetoelastic constant B_3 and the phonon Q_p ; but there is some question as to the reliability of these values.

APPENDIX A

PHYSICAL CONSTANTS FOR Zn_2Y , YIG , AND $SrTiO_3$

This appendix presents a table of those constants which were useful during this study, with special interest in the single crystal properties of each material. The single crystal values of the saturated magnetization were assumed to be the same as the polycrystalline values given, since the crystal anisotropy was overcome at 11 kOe.

The values of saturated magnetization and anisotropy at 29°C were used extensively throughout this study and are given below for reference:

General Constants

$4\pi M_s = 2624$ Oe

$H_A = 8460$ Oe

$p = H_A/4\pi M_s = 3.22$

$\omega_p/2\pi = 1.32$ kMc

$q = \omega_p/2\omega_M = 0.0898$

Property[*]	Zn_2Y	YIG	Strontium Titanate
Formula	$Zn_2Ba_2Fe_{12}O_{22}$	$Y_3Fe_5O_{12}$	$SrTiO_3$
Molecular Weight	1428	738	183
Density (gm/cm^3)	5.46	5.17	5.13[37]
Curie temperature (°K)	403	560	
Crystal type	Hexagonal	Cubic	Cubic
Lattice constant(s) of unit cell (Å)	a=5.88 c=14.5	a=12.37	a=3.90[38]
Initial permeability at 29°C			
Polycrystal	28		
Single crystal	700 est.		
Saturation magnetization $4\pi M_s$ (Oe) at 20°C		1700	
Polycrystal at 11 KOe	2700		
Powder at 11 KOe	2628[31]		
Temp. derating (Oe/°C) near r.t.	-8.4	-3.7	
Anisotropy field H_A (Oe) at 20°C	9000	45[35,9]	
Temp. derating (Oe/°C) near r.t.	-60 est.[32,33]	-0.7 est.[35,9]	
Dielectric constant at 27°C and 1.31 kMc	10 est.		277[†]
Temp. derating ($1/°C^{-1}$) near r.t.			-1.095[28]
Loss tangent at 1.3 kMc			$\leq 2.54 \times 10^{-4}$ [39,40]
Temp. derating ($1/°C^{-1}$) near r.t.			$\leq 3.65 \times 10^{-7}$ [40]
Specific heat c($cal\ gm^{-1}\ °C^{-1}$)	0.17 est.[34]		0.2 est.[41]
Elastic constants (erg/cm^3)		$c_{11}=26.9 \times 10^{11}$ [36] $c_{12}=1077 \times 10^{11}$ $c_{44}=7.64 \times 10^{11}$	

---

[*] The source for these data is reference 9 unless otherwise indicated.

[†] See Chapter V.

APPENDIX B

GLOSSARY OF PRINCIPAL SYMBOLS

$\underset{\sim}{A}$	Generalized vector which may represent $\underset{\sim}{\alpha}$, $\underset{\sim}{k}$, etc.
A_i	Component of generalized vector along coordinate direction i
A_i'	Component of generalized vector in rotated coordinate system
A_p	Pumping angle = h/H_0
$(A_p)_{ap}$	Apparent threshold angle = h_{ap}/H_0
$(A_p)_{cr}^{(n)}$	n^{th} order spin wave threshold
$(A_p)_{ij}$	Phonon threshold as a function of rotation angle ψ_0 ; i,j refer to the direction of polarization and propagation, respectively
$(A_p)_{ij_{cr}}$	Phonon threshold (minimized with respect to ψ_0)
$\mathcal{B}_k, \mathcal{B}_k'$	Time-independent spin wave amplitudes
B_1, B_2, B_3, B_4	Magnetoelastic constants for uniaxial crystal
$C_{\xi\xi\eta\eta}$, etc.	Elastic constants for uniaxial crystal
d	Normalized exchange field = $Dk^2/4\pi M_s$; ferrite disk diameter
E	Free energy of crystal
E_a	Anisotropy energy
E_K	Magnetpcrystalline energy
E_e	Elastic energy
E_m	Magnetostrictive energy
E_p	Phonon energy--the portion of E_e in the unstable mode
$\mathcal{E}_p$	Time average stored phonon energy in sample

G	Frequency modulation parameter
$\underset{\sim}{H}$	Total magnetic field = $\underset{\sim}{H}(\underset{\sim}{r},t)$
H_A	Anisotropy field along "hard" or c-axis
$\underset{\sim}{H}_a$	Anisotropy field
H_D	DC demagnetizing field in the plane of the ferrite disk
$\underset{\sim}{H}_d$	Demagnetizing field for uniform precession
$\underset{\sim}{H}_{dip}$	Dipolar magnetic field or demagnetizing field for spin wave
$\underset{\sim}{H}_{ex}$	Exchange field
$H_{ex\parallel,\perp}$	Exchange field constant in easy plane, normal to easy plane
$\underset{\sim}{H}_0$	Applied (external) dc magnetic field
H_{0n}	The applied dc field above which the n^{th} order spin wave instability is no longer allowed on resonance
h	Amplitude of applied (external) rf pump magnetic field
h_{ap}	Apparent critical field
h_{cr}	Critical field or threshold field
h_m	Value of h at beginning of pulse
h_{mp}	Value of h_m when the apparent threshold is reached
h_0	Maximum rf magnetic field amplitude for dielectric resonator
$\underset{\sim}{h}_p$	Applied (external) rf pump magnetic field
h_y	Nonzero component of $\underset{\sim}{h}_p$
i,j,k	Subscripts, each of which takes on the coordinate values 1,2,3 or x,y,z
K_{mp}, K_{pm}	Magnetic and phonon coupling constants for spin wave and elastic wave equations, respectively
$\underset{\sim}{k}$	Propagation vector
k_0	Elastic wave propagation constant on resonance

$\underset{\sim}{M}$	Magnetization vector
M_s	Saturated magnetization
N	Effective number of growing phonon modes
$N_{\parallel}$	Demagnetizing factor in the plane of the ferrite disk $= N_x = N_y$
n	Order of spin wave instability $= 2\omega/\omega$
P	Number of turns of frequency tuning plunger screw out from position of closest approach to dielectric resonator
P_a, p_a	Peak, average power absorbed by resonant system
ΔP_F	Change in ferrite absorption due to growth of instabilities
P_i	Incident pulse power level
P_{im}	Value of P_i at beginning of pulse
P_p	Phonon power absorption
$(P_p)_{ap}$	Phonon absorption at apparent threshold
P_r	Reflected pulse power level
ΔP_r	Change in reflected power level due to ΔP_F
P_{rm}	Value of P_r at beginning of pulse
p	Normalized anisotropy constant $= H_A/4\pi M_s$
Q	Spin wave Q
Q_{ext}	External Q of resonant system
Q_L	Loaded Q of resonant system
Q_O	Unloaded Q of resonant system; ferromagnetic resonance Q
Q_p	Phonon or elastic wave Q
q	Frequency normalization parameter $= \omega_p/2\omega_M$
$\underset{\sim}{R}$	Elastic displacement vector
$\underset{\sim}{R}_k$	Elastic wave amplitude

$\underset{\sim}{r}$	Spatial coordinate vector
$\underset{\sim}{r}_{\underset{\sim}{k}}, \underset{\sim}{r}_{\underset{\sim}{k}}'$	Time-independent elastic wave amplitudes
r_0	Standing wave ratio at resonance
$s, s_{\underset{\sim}{k}}$	Exponential phonon growth parameter
t_{ap}	Build-up time of phonon instabilities to the apparent threshold level
U, u	Peak, average stored energy in resonant system
x	Internal magnetic field parameter $= H/4\pi M_s$
x'	Effective internal magnetic field parameter $= (H + Dk^2)/4\pi M_s$
x, y, z	Crystallographic coordinates for uniaxial Zn_2Y ; coordinates used to describe dielectric resonator fields
x', y', z	Coordinates in rotated system at an angle ψ_0 with respect to fixed system
$\underset{\sim}{\alpha}$	Unit magnetization vector $= \underset{\sim}{\alpha}_0 + \underset{\sim}{\alpha}_s$
$\underset{\sim}{\alpha}_{\underset{\sim}{k}}$	Spin wave amplitude
$\underset{\sim}{\alpha}_0$	Uniform precession amplitude
$\underset{\sim}{\alpha}_s$	Spin wave component of the unit magnetization vector
Γ	Reflection coefficient of resonant system
γ	Gyromagnetic ratio $= ge/2mc$
ϵ_{ij}	Strain tensor component
η	Effective relaxation frequency in the presence of magnetoelastic coupling
$\eta_{\underset{\sim}{k}}$	Spin wave relaxation frequency $= \omega/2Q = \gamma\Delta H_k/2$
η_m	Spin wave relaxation frequency $= \omega_m/2Q$
η_p	Phonon or elastic wave relaxation frequency
θ	Spherical coordinate used to specify orientation of $\underset{\sim}{k}$
ρ_0	Density of ferrite sample

τ	Decay time constant of incident power pulse
ϕ	Spherical coordinate used to specify orientation of $\underline{k}$
ψ_0	Angle between rotated and fixed coordinate systems
$(\psi_0)_{opt}$	Optimum value of ψ_0 for pumping of most unstable phonon mode
ω	Frequency of unstable spin wave or elastic wave mode
ω_{H_A}	Anisotropy field frequency parameter $= \gamma H_A$
ω_{H_0}	Applied dc field frequency parameter $= \gamma H_0$
ω_M	Saturated magnetization frequency parameter $= \gamma 4\pi M_s$
ω_0	Ferromagnetic resonance frequency
ω_P	Pump frequency (i.e., frequency of applied rf magnetic field)
ω_k	Spin wave resonant frequency
ω_m	Spin wave resonant frequency containing modulation component
ω_p	Elastic wave resonant frequency
ω_p'	Elastic wave resonant frequency in the presence of magneto-elastic coupling and pumping by the uniform precession
ω_{p0}	Elastic wave resonant frequency in the presence of magneto-elastic coupling and zero pump
ω/Q	Phenomenological damping parameter for spin waves

REFERENCES

1. R. W. Damon, Rev. Mod. Phys. 25, 239 (1952).
2. N. Bloembergen and S. Wang, Phys. Rev. 93, 72 (1954).
3. H. Suhl, Proc. IRE 44, 1270 (1956).
4. R. I. Joseph, E. Schlömann and R. M. White, J. Appl. Phys. 34, 2686 (1963).
5. R. M. White and M. Sparks, Phys. Rev. 130, 632 (1963).
6. F. R. Morgenthaler, Proc. IRE 50, 2139 (1962).
7. B. A. Auld, R. E. Tokheim, and D. K. Winslow, J. Appl. Phys. 34, 2281 (1963).
8. B. A. Auld, J. Appl. Phys. 31, 1642 (1960).
9. J. Smit and H. P. J. Wijn, *Ferrites* (John Wiley and Sons, New York, 1959).
10. E. Schlömann, R. I. Joseph and I. Bady, J. Appl. Phys. 34, 672 (1963).
11. J. H. Saunders and J. J. Green, J. Appl. Phys. 32; 161S (1961).
12. E. Schlömann, Phys. Rev. 121, 1312 (1961).
13. E. G. Spencer, R. C. LeCraw, and C. S. Porter, J. Appl. Phys. 29 429 (1958).
14. R. C. LeCraw and E. G. Spencer, J. Phys. Soc. Japan, Suppl. 17(B1), 401 (1962).
15. J. J. Green, and E. Schlömann, J. Appl. Phys. 32, 168S (1961).
16. S. Dixon, Jr., A. Tauber, and R. O. Savage, Jr., "Parallel Pumping in Narrow Linewidth Planar Mn-ZnY," Decennial Conference on Magnetism and Magnetic Materials, Minneapolis, Minnesota, November, 1964.
17. E. Schlömann, J. J. Green, and U. Milano, J. Appl. Phys. 31, 386S (1960).
18. G. A. Alers, J. R. Neighbours, and H. Sato, J. Phys Chem. Solids 9, 21 (1958).
19. G. Simon, Z. Naturforsch. 13a, 74 (1958).
20. L. D. Landau and E. M. Lifshitz, *Theory of Elasticity* (Pergamon Press, Ltd., London, 1959).

21. H. Mueller, Phys. Rev. 58, 805 (1940).
22. J. F. Nye, *Physical Properties of Crystals* (Clarendon Press, Oxford, 1960).
23. C. Kittel, Phys. Rev. 110, 836 (1958).
24. R. C. LeCraw, Private Communication.
25. M. Sparks, *Ferromagnetic-Relaxation Theory* (McGraw-Hill Book Co., New York, 1964) Chap. 7.
26. C. Kittel, *Introduction to Solid State Physics* (John Wiley and Sons, New York, 1959).
27. P. M. Morse and H. Feshbach, *Methods of Theoretical Physics* (McGraw-Hill Book Co., Inc., New York, 1953) p. 437.
28. A. Okaya and L. F. Barash, IRE 50, 2081 (1962).
29. H-Y. Yee, Engineer's Thesis, Department of Electrical Engineering, Stanford University; Microwave Laboratory Report No. 1065, (July 1963).
30. E. L. Ginzton, Microwave Measurements (McGraw-Hill Book Co., Inc., New York, 1957).
31. R. C. Sherwood, Private Communication, Bell Telephone Laboratories,Inc.
32. Shing-gong Liu, Doctoral Dissertation, Department of Electrical Engineering, Stanford University, Microwave Laboratory Report No. 1092 (October 1963).
33. Shing-gong Liu, Private Communication.
34. R. F. Soohoo, *Theory and Application of Ferrites* (Prentice-Hall, Inc., New York, 1960) p. 22.
35. J. F. Dillon, Phys. Rev. 105, 759 (1957).
36. A. E. Clark and R. E. Strakna, J. Appl. Phys. 32, 1172 (1961).
37. Research Laboratory, National Lead Company, Titanium Division, South Amboy, N. J.
38. R. W. G. Wyckoff, *Crystal Structure* (Interscience Publishers, Inc., New York, 1948), Chap. VII.
39. A. Linz, Phys. Rev. 91, 753 (1953).
40. G. Rupprecht and R. O. Bell, Phys. Rev. 125, 1915 (1962).
41. *Handbook of Chemistry and Physics*, 43rd ed., (Chemical Rubber Publ. Co., 1961).

(Information arranged according to DD form 1473)

DOCUMENT CONTROL DATA - R AND D

1. ORIGINATING ACTIVITY

Microwave Laboratory
W. W. Hansen Laboratories of Physics
Stanford University, Stanford, California

2. REPORT SECURITY CLASSIFICATION

Unclassified

3. REPORT TITLE

Saturation Phenomena in Zn_2Y Ferrite at Frequencies Below Resonance

4. DESCRIPTIVE NOTES

Scientific Report Number 4

5. AUTHOR(S)

R. E. Tokheim

6. REPORT DATE

February 1965

7a. TOTAL NO. OF PAGES	7b. NO. OF REFS.	
176	41	
8a. CONTRACT OR GRANT NO.	8b. PROJECT NO.	8c. TASK NO.
AF 19(628)-342	4600	460003
9a. ORIGINATOR'S REPORT NUMBER(S)	9b. OTHER REPORT NO.(S)	
M. L. 1290	AFCRL-65-138	

10. AVAILABILITY/LIMITATION NOTICES

U. S. Government agencies may obtain copies of this report directly from DDC. All other persons can purchase copies from

Clearinghouse for Federal Scientific
and Technical Information (CFSTI)
Sills Building
5285 Port Royal Road
Springfield, Virginia 22151

11. SUPPLEMENTARY NOTES

None

12. SPONSORING MILITARY ACTIVITY

Air Force Cambridge Research Laboratories
Office of Aerospace Research
United States Air Force
L. G. Hanscom Field
Bedford, Massachusetts

13. ABSTRACT

An experimental and theoretical investigation was made of transverse pumping saturation effects in Zn_2Y ferrite at frequencies far below ferromagnetic resonance. Chief interest was in saturation effects at frequencies below the bottom of the spin wave manifold, where the lowest order phonon instabilities were expected to compete favorably with the higher order spin wave instabilities.

Measurements of saturation effects in single crystal Zn_2Y, with the easy plane lying in the plane of the disk, were made at 1.32 kMc. The dc and rf magnetic fields were applied orthogonally in the plane of the disk. The large rf magnetic fields required were obtained by employing a strontium titanate dielectric resonator. In these experiments the order of the first resonant spin wave instability permitted was varied from the first to the fifth by adjusting the position of the spin wave manifold relative to the pump frequency. The nature of the saturation was investigated by observing the waveform of the reflected pump pulse.

Theoretical on-resonance spin wave thresholds up to fourth order and off-resonance spin wave thresholds up to second order were derived. The first order theoretical spin wave threshold was the lowest threshold in the range of low dc magnetic fields. At higher dc fields the second order theoretical on- and off-resonance spin wave thresholds dominated the higher order thresholds. Taking the magnetoelastic effect as the dominant mechanism, first order phonon thresholds were derived for transverse and longitudinal elastic waves propagating in the easy plane and along the c-axis. The lowest theoretical phonon threshold was for transverse elastic waves propagating and polarized in the easy plane, and at frequencies below the bottom of the spin wave manifold, this threshold dominated the theoretical second order off resonance spin wave threshold. Theory was developed for the growth of phonon instabilities from thermal level in order to relate pulse saturation effects to the phonon absorption.

Transverse pumping thresholds observed experimentally were comparable with the above theoretical predictions and strongly indicate that first order phonon instabilities dominate the higher order spin wave instabilities at frequencies below the bottom of the spin wave manifold. These results together with the phonon growth theory made it possible to obtain rough estimates for the phonon Q, one magnetoelastic constant, and the exchange field of Zn_2Y in the easy plane. The observed pulse saturation effects and the results of two experiments for two different phonon absorption levels indicated the presence of nonlinear elastic wave damping.

14. KEY WORDS

Ferrites
Saturation effect
Spin wave thresholds
Phonon thresholds
Elastic wave thresholds
Zn_2Y
Elastic wave instability growth
Transverse pumping
Magnetoelastic constants
Exchange field
Elastic wave Q
Dielectric resonator